Spring 1-1-2018

An Analysis of Scientific Data Quality for the Fast Plasma Investigation of the MMS Mission

Alexander C. Barrie
University of Colorado at Boulder, abarrie@gmail.com

An Analysis of Scientific Data Quality for the Fast Plasma Investigation of the MMS Mission

by

A. C. Barrie

B.S., Virginia Polytechnic University, 2004

M.S., Virginia Polytechnic University, 2006

A thesis submitted to the

Faculty of the Graduate School of the

University of Colorado in partial fulfillment

of the requirements for the degree of

Doctor of Philosophy

Department of Aerospace Engineering

2018

This thesis entitled:
An Analysis of Scientific Data Quality for the Fast Plasma Investigation of the MMS Mission
written by A. C. Barrie
has been approved for the Department of Aerospace Engineering

Prof. Zoltan Sternovsky

Prof. Xinlin Li

Prof. Robert Marshall

Prof. Scot Elkington

Dr. Craig Pollock

Date

The final copy of this thesis has been examined by the signatories, and we find that both the content and the form meet acceptable presentation standards of scholarly work in the above mentioned discipline.

Barrie, A. C. (Ph.D., Aerospace Engineering)

An Analysis of Scientific Data Quality for the Fast Plasma Investigation of the MMS Mission

Thesis directed by Prof. Zoltan Sternovsky

This work describes technical innovations to improve the data quality and volume for the Fast Plasma Investigation (FPI) on board the Magnetospheric Multiscale mission (MMS). A parametric study of wavelet compression has shown that plasma count data can be compressed to high compression ratios with a minimal effect on the integrated plasma moments. Different regions of the magnetosphere are analyzed for both electron and ion count data. The FPI trigger data, intended as a data ranking metric, has been adapted and corrected to a point where scientifically accurate pseudo moments can be generated and released to the research community, drastically increasing the availability of high time resolution data. This is possible due to a scaling system that tunes the dynamic range of the system per region, and the method of using a neural network to correct for exterior contamination effects, such as spacecraft potential. Finally, a map of detection angle bias has been generated that can be used to correct raw count for errors in look direction of incoming particles. This map was generated by statistically sampling particle flight paths through a charged spacecraft environment, validating against flight data. All three of these efforts lead toward the overarching goal of improving data quality and volume for the FPI suite, and future missions to come.

Dedication

Dedicated to my little dude, Will. I can hear you running around laughing as I write this...

Acknowledgements

I would like to thank my dissertation committee: Zoltan Sternovsky, Xinlin Li, Robert Marshall, Scot Elkington, and Craig Pollock. Scot has been my magnetospheric physics sounding board through this process and has kept me on the right track. Zoltan was willing to take a chance on someone who wanted to do the entire PhD remotely. Rob Studer rescued me from the desert and brought me to Goddard, and Craig Pollock, Lillian Reichenthal and Mark Adrian brought me into the heliophysics branch and onto the FPI team. I received immeasurable help, and encouragement from Levon Avanov, Ulrik Gliese, John Dorelli, Chad Salo, Charles Dickson, Dan Gershman, Dave Rand, and everyone else on the team over the years. Daniel da Silva was my neural network and python expert. Barbara Giles was hugely supportive in my research and allowing me time away from work to complete this degree. Last but not least from FPI, Conrad Schiff, continuously offered sage business advice, accompanied me to the cafeteria, and listened to my various witty remarks.

I would like to thank the extended community at LASP as well. The initial encouragement from Chris Pankratz and Dan Baker finally pushed me over the edge and back into graduate school. The whole MMS group out there was fantastic - Patrick, Gina, Emily, Sasha, and everyone else. The same goes for the folks at ESA who worked with me on the MMS sheath model.

I would especially like to thank my friends and family who supported me along the way: Bill, Sarah, Chris, and in particular, my beautiful wife, Asli, who held my hand all the way through.

Much of the original engineering design work included here was supported by NASA/GSFC. My tuition, as well as all travel to Boulder, was funded by Aurora Engineering (thanks Steve).

Contents

Chapter

1 Dissertation Statement and Contributions **1**

1.1 Data Compression 1

1.2 Pseudo Moments 2

1.3 Particle Trajectories 2

2 Introduction **4**

2.1 Instrument Description 9

2.2 Operational Modes and Data Products 12

2.3 Research Overview 14

3 Predicting Errors Associated with Wavelet Data Compression **19**

3.1 Introduction 19

3.2 Error Modes and Effects on Data 22

3.2.1 Macroscopic View of Magnetosphere 22

3.2.2 Errors in Simulated Moment Data 26

3.2.3 Exploration of Error Modes Using Simulated Data 29

3.3 Error Modes 29

3.3.1 Observable Error 30

3.3.2 Subtle Error 33

3.3.3 Performance with Increased Compression 36

3.4 Conclusion 48

4 Development and Validation of Science Quality Pseudo Moments 54

4.1 Introduction 54

4.2 Ground Based Moment Calculations 56

4.2.1 Data Manipulation 56

4.2.2 Calculate the Plasma Moments 58

4.3 Pseudo Moment Calculations 59

4.3.1 On Board Trigger Term Calculations 60

4.3.2 FPGA Implementation 61

4.3.3 Scale Factor Tuning 62

4.3.4 Reconstitution of Data on Ground 65

4.4 Flight Validation 73

4.4.1 Dynamic Range Scaling 73

4.5 Conclusion 82

5 Sheath Effects on Particle Trajectories 86

5.1 Introduction 86

5.2 Algorithms 88

5.2.1 Potential Map 88

5.2.2 Particle Traces 89

5.3 Results 93

5.4 Flight Validation 97

5.5 Application 101

5.6 Conclusion 102

6 Concluding Remarks 104

Bibliography **107**

Appendix

A FPI Energy Targets **113**

Tables

Table

2.1 Four operational energy ranges stored in EEPROM (Electronically Erasable Programmable Read-Only Memory), each used in different regions of the magnetosphere. 11

3.1 Compression allocation (on board storage, per skymap) for all data types 22

3.2 Parameters used for simulation of single spin in magentosphere/sheath to examine effect of compression on plasma moments. 27

4.1 List of currently used scale factors for MMS mission. 66

5.1 Plasma parameters used for SPIS charging simulation 88

5.2 Plasma parameter ranges for electron data from the flight data selected in Figure 5.9 100

A.1 Energy targets for the DIS spectrometers in each of the four EEPROM slots, as of July 1, 2018. 114

A.2 Energy targets for the DES spectrometers in each of the four EEPROM slots, as of July 1, 2018. 115

Figures

Figure

2.1 Plasma inflow forces two opposing magnetic fields together until they reconnect, releasing energetic particles. 5

2.2 Illustration of the Earth's magnetosphere. Solar wind, entering from the left, skews the shape of Earth's magnetic field as it decelerates, causing distinct regions.[42] . . 6

2.3 Magnetic reconnection can occur when the solar wind pushes the Interplanetary Magnetic Field (IMF) into Earth's field on the day side, or when Earth's field is compressed into itself in the tail region.[42] 7

2.4 Orbital phases of the MMS mission. 9

2.5 Illustration of DES top hat functionality. 16

2.6 Views of the DES (a), DIS (b), and IDPU (c). These photos do not include final blanketing, harnessing, heaters, etc.[42] 17

2.7 Field of view of DES/DIS (left) and instrument positions as shown on MMS instrument deck (right).[42] 17

2.8 Pixel look directions resulting from rectilinear mapping of spherical coordinate system. 18

3.1 Histogram of all flight FPI flight data showing compressed image size as a function of local environment (temperature and density.) 23

3.2 Flight results of DES compression performance over full day side pass (Phase 1A) as a function of image entropy. 24

3.3 Flight results of DIS compression performance over full day side pass (Phase 1A) as a function of image entropy. 25
3.4 Histogram of initial DES burst data from Phase 1B using increased image size limit. 26
3.5 Simulation of a single spin of DES moments (density, velocity vector, temperature tensor) in the magnetosheath. 28
3.6 Simulation of a single spin of DIS moments (density, velocity vector, temperature tensor) in the magnetosheath. 29
3.7 Simulation of a single spin of DES moments (density, velocity vector, temperature tensor) in the magnetosphere. 30
3.8 Simulation of a single spin of DIS moments (density, velocity vector, temperature tensor) in the magnetosphere. 31
3.9 Flight data showing illustrating a difference in spin tone between summed bursts (blue) and fast survey (black) introduced by compression error (23:29 - 23:30). . . . 32
3.10 Smearing of large gradients. Original sky map (left), post compression/decompression sky map (center), and difference map (right). 33
3.11 Observed electron counts for MMS4 for a given range at two energy slices: 54 eV (top) and 300 eV (bottom). 34
3.12 Difference map showing a checkerboard pattern (left) introduced by the compression algorithm. A zoom in of the area enclosed in green is shown (top right). 35
3.13 Difference map showing artifacts introduced in low count regions, present in integer mode (left) and not present in floating point mode (right). 37
3.14 Effect of background noise redistribution. Original sky map (left), post compression/decompression sky map (center), and difference map (right). 38
3.15 Plasma moments calculated for a partial magnetopause crossing from December 29, 2016. 41
3.16 Compression performance on typical magnetopause crossing from December 29, 2016 for electrons (top) and ions (bottom). 42

3.17 Plasma moments calculated for a typical solar wind interval from December 7, 2016. 44
3.18 Compression performance on typical solar wind data from December 7, 2016 for electrons (top) and ions (bottom). 45
3.19 Plasma moments calculated for a magnetosheath interval from November 8, 2017 . . 46
3.20 Compression performance on magnetosheath data from November 8, 2017 for electrons (top) and ions (bottom). 47
3.21 Plasma moments calculated for an interval from July 6, 2017. 48
3.22 Compression performance on tail data from July 6, 2017 for electrons (top) and ions (bottom). 49
3.23 Plasma moments calculated for an interval from December 30, 2016. 50
3.24 Compression performance on inner magnetosphere data from December 30, 2016 for electrons (top) and ions (bottom). 51
3.25 Plasma moments calculated for an interval from August 7, 2017. 52
3.26 Compression performance on lobe / PSBL data from August 7, 2017 for electrons (top) and ions (bottom). 53

4.1 Identifying the error modes associated with the FPGA term accumulations: quantization, and saturation of the two summation loops. 64
4.2 Scale factors can be chosen to optimize a certain plasma regime and tuned to either the red or blue regions. 66
4.3 Relationship of raw, uncorrected trigger terms to Level 2 (L2) plasma moments. . . 67
4.4 Final correction fits of the pseudo moments as a function of likelihood. 71
4.5 Histograms illustrating accuracy of trigger term to pseudo moment corrections. . . . 72
4.6 Trigger term corrections as a function of spacecraft potential. 72
4.7 Histograms of 2017/2018 day side pass with scale factors tuned for magnetopause crossings. 75
4.8 Histograms of 2017/2018 day side pass with scale factors tuned for solar wind. . . . 76

4.9 Histograms of the June 20 through July 20, 2017 pass through the central tail current sheet. 77
4.10 ET spectrogram for ions (top) and electrons (2nd from top) show a transition region into higher density plasma. 78
4.11 ET spectrogram for ions (top) and electrons (2nd from top) show a data segment near the central current sheet in the magnetotail. 79
4.12 December 30, 2015 (MMS1); Electron pseudo moments (blue) compared to level 2 burst resolution data (orange) and fast survey (green). 81
4.13 December 30, 2015 (MMS1); Ion pseudo moments (blue) compared to level 2 burst resolution data (orange) and fast survey (green). 82
4.14 December 30, 2015 (MMS1); capture of Alfvén wave structure in electron pseudo moments zoomed around the 22:26 time index. 83
4.15 December 30, 2015 (MMS1); capture of Alfvén wave structure in ion pseudo moments zoomed around the 22:26 time index. 84

5.1 Ambient potential as calculated by SPIS model 90
5.2 Histograms of particle distributions for electrons (top) and ions (bottom) 92
5.3 Detection bias map for electrons (top) and ions (bottom) for the lowest FPI energy range (10 - 13 eV) 94
5.4 Detection efficiency map corresponding to an FPI energy/angle sky map for electrons (left) and ions (right). 95
5.5 Absolute error in trajectory angle as a function of energy, separated per bay. 96
5.6 Estimation of error and uncertainty for a trajectory measurement versus energy . . . 96
5.7 Distributions of detected particles per bay, collapsed over all energies 97
5.8 Comparison of simulated data (top) to flight data (bottom) for particle detection bias 99
5.9 Flight electron (DES) bias maps from six selected regions from August, 2016 100
5.10 Flight electron (DES) bias maps for all four observatories in similar environments . . 101

Chapter 1

Dissertation Statement and Contributions

This dissertation contributes to the area of remote sensing of space plasmas. Specifically, it focuses on increasing data volume and data quality for count data measured by plasma spectrometers, using data from the Fast Plasma Investigation on board the Magnetospheric Multiscale mission. The work presented in this dissertation has led to four journal article submissions, described here.

1.1 Data Compression

AC Barrie, S Elkington, Z Sternovsky, D Smith, B Giles, and C Schiff. Wavelet compression performance of mms/fpi plasma count data. **Journal of Geophysical Research: Earth and Space Science**, 2018. Under Review

AC Barrie, SE Smith, JC Dorelli, DJ Gershman, P Yeh, C Schiff, and LA Avanov. Performance of a space-based wavelet compressor for plasma count data on the mms fast plasma investigation. **Journal of Geophysical Research: Space Physics**, 122(1):765–779, 2017

These two papers demonstrate a marked improvement in data compression over previous missions. While many data compression algorithms exist, only the most basic algorithms have been flown for compressing plasma count data due to a fear of compression induced error. These two manuscripts outline the performance metrics of wavelet based compression for plasma count data looking specifically at what levels of compression can be achieved balanced against acceptable error levels. They show that compression of data can be increased from the heritage limits of 2:1 to

beyond 10:1 with acceptable error. This represents a significant increase in available data volume for future missions, and also helps scientists to fully understand which signatures in data may be compression induced error.

1.2 Pseudo Moments

AC Barrie, D da Silva, S Elkington, Z Sternovsky, AC Rager, DJ Gershman, WR Paterson, JC Dorelli, and B Giles. Physically accurate large dynamic range pseudo-moments for the mms fast plasma investigation. **Earth and Space Science**, 2018

Previous missions have computed onboard plasma moments, but have had large uncertainties due to the required dynamic range of the data, and from unavoidable errors introduced by the spacecraft and environment. This manuscript presents a method used by FPI to tune the dynamic range of the system so as to retain high resolution and low uncertainty over the entire environmental dynamic range. The data are then corrected for external effects using a neural network, which has also never been done before for onboard moments. Together, these two advances allow the onboard moment summations of FPI to rival the fully corrected, high resolution data in terms of accuracy. This is a major advancement in the sense that, while the standard high resolution data is only available for a small fraction ($\sim$ 5%) of the science collection time, these pseudo moments are available for the entire science collection region - a 20 fold increase in the quantity of science data available for study.

1.3 Particle Trajectories

AC Barrie, Z Sternovsky, and S Elkington. Correcting particle measurements for potential sheath effects. In Preparation

While it is standard practice to correct particle energies based on the spacecraft potential, the effect of spacecraft potential on individual particle trajectories has only been attempted for ex-

tremely simplified, unrealistic test cases. This manuscript presents a new method of reporting error and uncertainty in particle trajectories based on a simulation of the plasma sheath and integrated particle paths that accurately models the flight performance of the in-situ MMS spacecraft. This method is only now possible due to advancements in spacecraft charging models and computational power for statistical analysis of the trajectories. In addition to informing the quality of the data, this work also presents a stepping stone towards correcting raw count data. This approach can correct counts that are in a near isotropic environment, however a more accurate simulation model would be needed for the correction to be reliable.

Chapter 2

Introduction

Magnetic reconnection is a fundamental physical process that is not well understood. Plasma can stretch a magnetic field, storing energy in the field. If two opposing magnetic fields are pushed together, they can 'snap' and reconfigure releasing the stored energy in the form of energetic particles. Figure 2.1 shows this process. As the plasma inflow compresses the two opposing field lines together (top/bottom), they reconnect into a new configuration (left/right), releasing energetic particles. At the center of the reconnection region the ions, and eventually electrons, become demagnetized as the magnetic field strength lessens into a magnetic null. In these regions, referred to as ion and electron *diffusion regions*, the plasma is no longer gyrotropic, or bound around the magnetic field line.

While it is desirable to understand physical processes, such as this, simply to advance basic knowledge of the universe, there are practical applications to understanding reconnection as well.

- Magnetic reconnection is believed to be a driving force in solar flares and coronal mass ejections (CMEs.) These phenomena can emit high energy radiation and particles, upwards of 10s of MeV for electrons and MeV to GeV for ions[34]. This can be an important driver for space weather. Understanding the process by which flares and CMEs evolve could potentially help scientists predict their occurrence and give satellites time to prepare before being bombarded with high energy particles and radiation.

- Magnetic reconnection also occurs in small scale locations. For example, reconnection

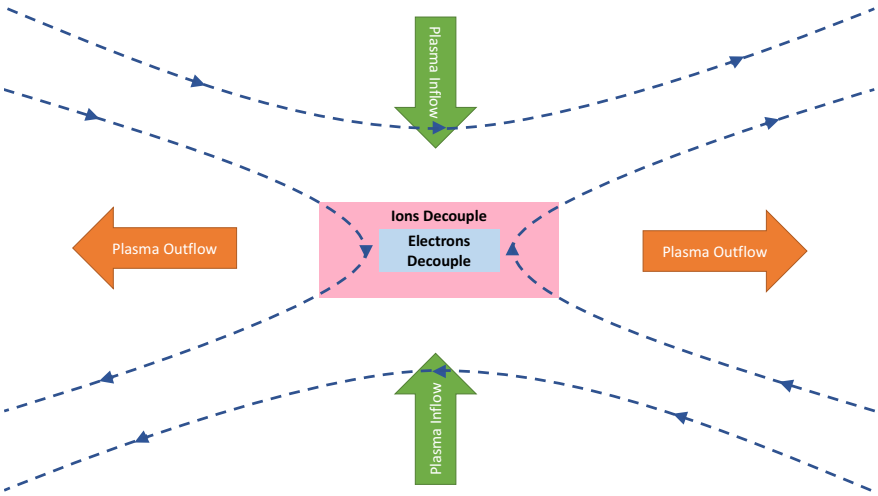

Figure 2.1: Plasma inflow forces two opposing magnetic fields together until they reconnect, releasing energetic particles. At the center of the phenomenon, the magnetic field reduces to the point where ions, and eventually electrons, become demagnetized.

is suspected to be a cause of why magnetically contained fusion, such as in tokamaks, is unstable and cannot be maintained. Being able to mitigate reconnection could significantly advance fusion research.

The general idea of reconnection is well known[53, 58], and has been observed in a limited fashion[50, 8]. As with many physical processes, however, the devil is in the details and many aspects of the reconnection process are still debated. NASA has posed[41] these questions as

- What determines when reconnection starts and how fast it proceeds?
- What is the structure of the diffusion region?
- How do the plasmas and magnetic fields disconnect and reconnect in the diffusion regions?
- What role do the electrons play in facilitating reconnection?
- What is the role of turbulence in the reconnection process?
- How does reconnection lead to the acceleration of particles to high energies?

NASA is aiming to answer these questions by observing reconnection in-situ in the Sun/Earth magnetosphere boundaries. While magnetic reconnection can occur in many places, the time and length scales involved make it difficult to investigate terrestrially. As such, Earth's magnetosphere is an attractive place to study this phenomenon. Figure 2.2 shows the primary regions of Earth's magnetosphere.

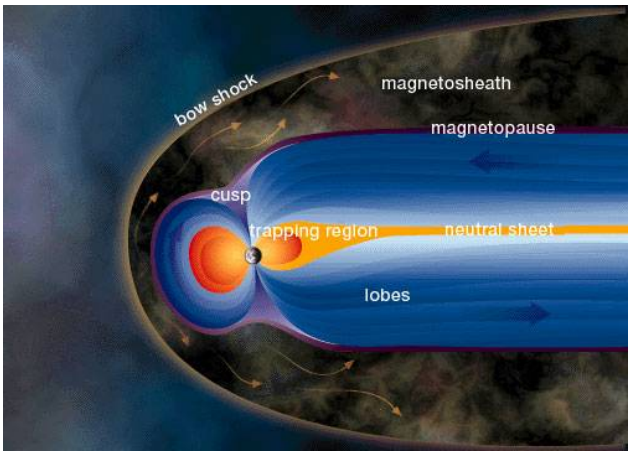

Figure 2.2: Illustration of the Earth's magnetosphere. Solar wind, entering from the left, skews the shape of Earth's magnetic field as it decelerates, causing distinct regions.[42]

Energetic particles ($\sim 1 - 10$ keV) known as the solar wind, emanate from the Sun in all directions. This primarily consists of collimated ions, and thermal electrons. These particles impact Earth's magnetic field in the near vicinity of the Earth. The supersonic and super Alfvénic solar wind particles are slowed in a shock boundary, known as the bow shock. The magnetopause represents the outer boundary between Earth's inner magnetosphere and the solar wind. The region in between the bow shock and magnetopause is referred to as the magnetosheath, where the solar wind is present, but no longer supersonic. In the region behind the Earth, that does not see direct solar wind, a long magnetotail extends outward containing a centralized neutral current sheet inside of a wider lobe region. The day side and tail side regions meet in an area called the cusp. The trapping region, or radiation belts and ring current, represent trapped particles in Earth's interior magnetic field.

With regard to magnetic reconnection, the solar wind is the plasma that compresses the

magnetic fields together in two primary locations. On the day side, the Interplanetary Magnetic Field (IMF) is compressed into Earth's magnetic field creating reconnection events around the magnetopause. In the magnetotail, Earth's magnetic field is compressed into itself, creating a potential for a reconnection region. These two regions are highlighted in Figure 2.3

The size of the diffusion region, even in an area as large as the magnetosphere, is small (a few km for electrons) relative to the resolution of typical measurement scales, and the region can be moving in excess of 100 km/s relative to the spacecraft. This means that measurements must be taken extremely quickly. The CLUSTER mission[21] saw some evidence of magnetic reconnection, but was not able to resolve any of the fine details[12, 50, 8]. The Magnetospheric Multiscale mission (MMS) is a mission designed to operate quickly enough to capture electron scale measurements in the diffusion region. Specifically, a measurement time of 30 or 150 ms measurements for electrons and ion respectively, is required in order to capture several data points in the diffusion region. This represents a factor of over 100 times faster than previous missions[21, 40]. MMS is therefore the first mission capable of observing sub-gyroperiod physics[9, 52, 10, 54].

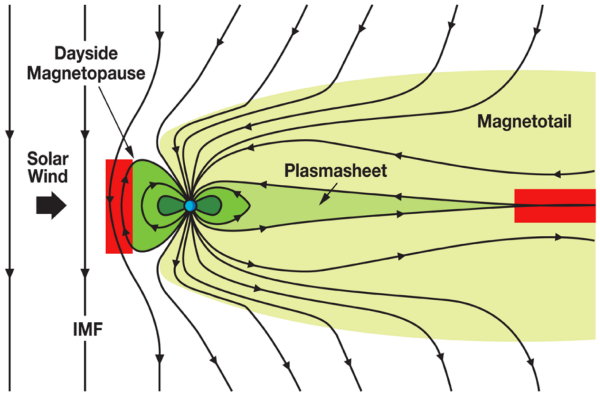

Figure 2.3: Magnetic reconnection can occur when the solar wind pushes the Interplanetary Magnetic Field (IMF) into Earth's field on the day side, or when Earth's field is compressed into itself in the tail region.[42]

MMS was launched on March 13, 2015. The purpose of the mission is to find physical evidence of magnetic reconnection[9]. To accomplish this, MMS has a large suite of instruments on each of

the four identical satellites that measure the local electric field, magnetic field, electron and ion distributions, and plasma composition.

The Laboratory for Atmospheric and Space Physics (LASP) is an affiliate of CU Boulder and houses the Science Data Center (SDC) for the MMS mission. FPI is managed out of the NASA Goddard Space Flight Center (GSFC). MMS has completed a prime science mission, consisting of several phases, looking for evidence of magnetic reconnection at the day side magnetopause and in the magnetotail.

(1) Phase 1A: A day side pass with apogee of 12 Re, targeting the magnetopause

(2) Phase 1X: A 12 Re tail pass with limited science gathering

(3) Phase 1B: A second day side pass, similar to 1A

(4) Phase 2A: Apogee raise to 25 Re with limited science gathering

(5) Phase 2B: 25 Re tail pass

These phases are illustrated in Figure 2.4. MMS has recently been funded to continue science operations in an extended mission, maintaining formation quality and continuing science collection. The extended mission, for the immediate future, will maintain the Phase 2B orbit configuration and constellation formation.

The primary science goal of the MMS mission is to:

> *Reveal the small-scale three-dimensional structure and dynamics of the elusively thin and fast-moving electron diffusion region.[42]*

In practice, this means that MMS must be able to observe the electric and magnetic fields, as well as electron and ion particle distributions with spatial and timing resolutions fast enough to resolve several data points within the electron diffusion region. This must be performed simultaneously on four satellites in order to obtain three dimensional spatial gradients .

Much of this work focuses on the Fast Plasma Investigation (FPI), which consists of four Dual Electron Spectrometers (DES), four Dual Ion Spectrometers (DIS) and one Instrument Data

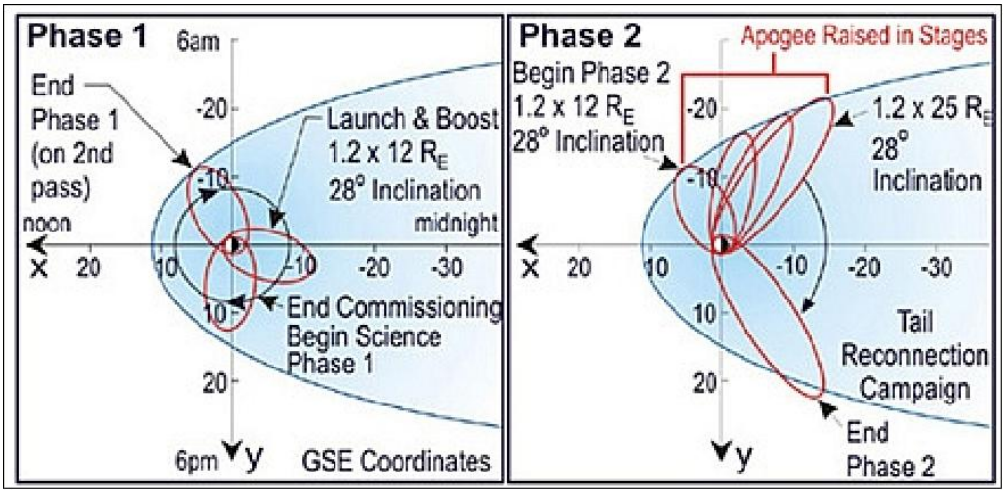

Figure 2.4: Orbital phases of the MMS mission. Phase 1 consisted of two day side passes at 12 Re (MMS operated during the 12 Re tail pass, but many instruments were not collecting science data). Phase 2 consisted of an apogee raise to 25 Re and a science collection region through the tail.[42]

Processing Unit (IDPU) per spacecraft. These spectrometers measure electrons and ions over a full 2π steradians every 30 ms for electrons and 150 ms for ions. The energy range varies with plasma environment, but the operational range of the DES is 6 eV to 30 keV and the DIS is 2 eV to 30 keV.

2.1 Instrument Description

FPI[52] consists of four DES, four DIS, and one IDPU (Fig. 2.6.) The spectrometers are dual half top-hat analyzers which will measure the 3D plasma environment and the IDPU will process the data. As illustrated in Figure 2.5, a top-hat analyzer utilizes nested hemispheres (or tori), with different applied voltages to achieve a curved channel with a constant interior electric field[11]. This electric field acts as an energy bandpass filter, which in the case of FPI, has an energy resolution (dE/E) of about 18-20% for DES and 12-15% for DIS. The applied voltage is swept in magnitude to adjust the target measurement energy. The axisymmetric nature of a top-hat allows for simultaneous measurements in all look directions, rotated around the axis of symmetry. FPI uses two back to back half top-hats, as shown in Figure 2.6. In addition, two electrostatic steering

electrodes are present, allowing each spectrometer to deflect the look direction up to a maximum of $\sim$ 20 degrees. FPI does not use a full top-hat, but rather a truncated half top-hat design. Two of these are placed back to back, with a shared power supply, to make a dual half top-hat. When four of these units are placed evenly around the spacecraft, a full sky image can be taken quickly by combining several simultaneous measurements. Figure 2.7 shows the instrument positioning and fields of view on the spacecraft.

The detection system consists of a chevron stack of two micro-channel plates (MCP), with a segmented anode underneath, followed by amplifying and filtering electronics before the digitized count data are recorded. An MCP is a thin, semi-conductive, plate that has a large number of narrow channels through it at a given bias angle. These channels are coated in a material with a large secondary emission coefficient. This means that when a particle enters a channel and hits the wall, more than one secondary electron are often generated. The two plates have opposite bias angles, forming a chevron shape. This is to put an effective turn in the channel, increasing the probability that particles will impact the surface. A voltage differential is applied across the MCP stack, such that any secondary electrons generated are then accelerated downward. These in turn impact the wall generating more secondaries, resulting in a cascade effect that acts as a gain multiplier. For the MCP stack used in FPI, a gain of $\sim$ 1e6 is achieved for a single particle.

Azimuthally (direction of spacecraft spin, roughly around GSE_Z), FPI has 32 data bins, each of 11.25 degrees to cover a full 360 degrees. Each head of each spectrometer can electrostatically deflect to four different states. In elevation, a segmented anode simultaneously measures 16 look directions. The entire *skymap* is therefore composed of $32 \times 16 = 512$ look directions, with each direction measuring 11.25×11.25 degrees. As shown in Figure 2.8, a rectilinear mapping of the spherical measurement space results in oversampling near the poles. It is also not immediately clear in the data, which measurement points came from which spectrometer. This can be critically important because the units do not all have exactly the same performance characteristics[52]. Efficiency changes between spectrometers as well as variations in energy and angle bandpass are corrected on the ground[24, 54].

Table 2.1: Four operational energy ranges stored in EEPROM (Electronically Erasable Programmable Read-Only Memory), each used in different regions of the magnetosphere. The safety table is used when suspected high voltage anomalies are detected in DIS.

Memory Slot	Region Used	DES Min (eV)	DES Max (eV)	DIS Min (eV)	DIS Max (eV)
EEPROM1	Magnetotail	6	30,000	2	30,000
EEPROM2	EM Sheath	6	23,000	2	19,000
EEPROM3	DIS Safety	6	30,000	2	11,000
EEPROM4	Solar Wind	4	940	197	9,222

A 32 step energy table is used, with the energy steps being roughly logarithmic in spacing. The azimuthal bandpass is $\sim 5-8\%$ and the energy bandpass of the detectors is $\sim 18-20\%$ for DES and $\sim 12-15\%$ for DIS, meaning that small gaps exist between both azimuthal angle and energy bins (no gap exists in the polar direction because of the segmented anode design.) The energy range can be altered via loading one of four different voltage (energy) stepping tables into memory. The current operational concept utilizes the options shown in Table 2.1. Exact values for the energy step tables are given in Appendix A. The energy range of the spectrometers is tuned to target the regions in question. Switching tables requires rebooting the IDPU, which takes a few seconds, and reramping the high voltage MicroChannel Plates (MCPs), which takes about 20 minutes. The DIS Safety table is not used under normal circumstances, but can be used if there is suspicion of a high voltage discharge in one of the DIS units (due to suspected workmanship issues in assembly of DIS.) The safety table would be used during the investigation of the discharge until a permanent action (such as limiting the spectrometer in question) can be taken.

Note that while the minimum energies measured are 2 and 6 eV for ions and electrons, the lowest energy calibrated on the ground for both electrons and ions was 10 eV. Measuring this low energy tail is difficult for two primary reasons:

(1) The high voltage power supplies (HVPS) have a quantization limit, and offset error, that make it difficult to achieve precise voltage settings at low energies. These errors alter the exact energy and look angle being measured. Not only are these errors non-uniform from unit to unit, but they also vary with time, due to aging, and over temperature.

(2) The spacecraft will charge to several volts creating a plasma sheath around the spacecraft. This, in turn, will deflect incoming particles, altering their trajectories (both energy and direction). While the energy error is directly related to the spacecraft potential, the directional error is hard to predict. Chapter 5 explores this effect.

Because of these concerns, while distributions are reported down to the minimum energies, moment integrals are only performed above 10 eV. Details of the plasma moment integration process can be found in [54, 25].

A total of 32 azimuth, 16 elevation, and 32 energy = 65,536 measurements are taken for a complete energy/angle scan. This is performed in 128 separate measurements - 32 energies at each of four deflection states, per spectrometer. Elevation measurements are taken simultaneously. Given the time requirements of 30 ms for electrons and 150 ms for ions, plus margin for high voltage (HV) settling, an integration time of $195\mu s$ for electrons and 1 ms for ions are used. The geometric factor[14] of both DES and DIS is $\sim 5e-4cm^2eV/eVsr$ per pixel. In this particular context, the pure geometric factor[14] could not be measured; rather this number is a convolution of geometric factor and detection system efficiency. This means that $\sim 1/2000$ particles entering the aperture of the instrument will ultimately be detected. These data lead to an average count rate of < 100 per integration period (look angle / energy combination) in most plasmas, peaking at a maximum of ~ 400 counts before the MCPs are fully saturated[37].

2.2 Operational Modes and Data Products

FPI has five primary operating modes:

(1) **Safe** mode disables all commanding and high voltage operation of the instruments. This mode is used when anomalies are detected, or during maneuvers.

(2) **Engineering** mode is an interactive mode that allows individual commands to be sent to the instruments. This is used for executing calibration sequences and as a standby mode during periods of inactivity.

(3) **Fast Survey** is the primary science mode and accumulates data at the fastest rate of one complete energy/angle sweep per 30 ms / 150 ms for electrons and ions respectively.

(4) **Slow Survey** is a secondary science mode that uses a single spectrometer integrating counts over three spins of the spacecraft, for a single energy/angle sweep every 60 s. Slow Survey (SS) is used in regions of lesser scientific interest as a means to lessen wear on critical components.

(5) **Calibration** mode is a legacy mode that performs a calibration sequence that is no longer used.

The instrumentation on board MMS is commanded via a multi-tiered operational sequence for routine operations:

(1) **Automated Time Sequence (ATS)** is the top level spacecraft command sequence

(2) **Relative Time Sequence (RTS)** are called from the ATS or another RTS. These represent *activities*, such as a calibration sequence for FPI. They are short and generally represent wrappers for larger sequences.

(3) **Macros** are called from RTSs and are longer lists of serial instrument commands.

While FPI generates many different packet types[52, 9], there are a small number of scientific or operational interest:

(1) **Housekeeping**, or HK data is generated every 5 seconds and samples relevant health, safety, and status metrics from the instruments such as currents and temperatures. A highly developed ground monitoring system scans this data for potential problems.

(2) **Integrate** packets are the result of a single command for the spectrometer to collect counts at a given energy and look direction. These are used primarily for calibration sequences.

(3) **Burst** data packets are the high time resolution (30/150 ms) science data. These are generated while the IDPU is in Fast Survey mode.

(4) **Fast Survey** data are a 4.5 s accumulation of burst packets. These are generated when the IDPU is in Fast Survey mode.

(5) **Slow Survey** data are 60 s spin integrated science data generated in Slow Survey mode.

(6) **Trigger** data are a series of on board integrations of counts designed, initially, as a metric for ranking science data for priority downlink. These data are generated when the IDPU is in Fast Survey mode. They represent integrals of on board count measurements that are roughly proportional to physical plasma moments (density, pressure, etc). Chapter 4 explores ways to extract added science information from these data products.

All science data (burst, fast survey, slow survey) are compressed on board to varying degrees. The errors and effects associated with the data compression are explored in Chapter 3. All fast survey and slow survey data are downlinked to the ground. The burst data has a much larger data volume, and as such only $\sim 5\%$ of the burst data are downlinked. There is an automated trigger system[47] in place to rank the data for scientific value, however this ranking is often adjusted by a human *Scientist In The Loop* (SITL).

Once data is received on the ground, it is processed to generate distribution functions, plasma moments, etc. These processed data are available to the public through the MMS Science Data Center (SDC) located at the CU Boulder, Laboratory for Atmospheric and Space Physics (LASP)[33].

2.3 Research Overview

As MMS progresses through its lifetime, and more data are collected, an increased emphasis is being placed on data quality. This work is focused on an analysis of scientific data quality on board MMS and ways to improve it. This is divided into three primary investigations:

(1) **Effects of Data Compression on Science Data Quality** - FPI uses a discrete wavelet transform with a bit plane encoder (DWT/BPE) to compress data to high compression ratios. The performance of the FPI wavelet based compression engine is examined in a

broader context, looking specifically at the limits of wavelet compression for regions of high scientific interest. Flight data is compressed to increasingly small sizes, with associated errors analyzed for their effect on the science data quality leading to an in depth presentation of error modes associated with varied levels of data compression. Specific plasma environments are investigated to form a broad picture of the applicability of wavelet compression for count data. Recommendations are made for future missions that will collect counts in all regions of Earth's magnetosphere with increasingly high compression requirements.

(2) **Development Pseudo Plasma Moments** - Design and analysis of flight performance of a pseudo moment system for FPI that can track plasma parameters at the highest time resolution for a fraction of the data bandwidth of the full skymap images. This system is based on using the data from the trigger data ranking system, with a robust set of corrections on the ground. The dynamic range of the integration algorithm can be adjusted via a set of input parameters, allowing the user to focus on specific plasma environments as the spacecraft passes through them. Comparisons between the burst, fast survey, and pseudo moment data validate the algorithms and approaches taken.

(3) **Effects of a Plasma Sheath on Incoming Particle Trajectories** - Analysis of the error introduced on particle velocities by traveling through the electrostatic sheath around MMS. A statistical trajectory analysis is performed to generate a map of detection efficiency bias per look direction and energy. A bias map is generated, which highlights areas of uncertainty and error in the collected counts matrix. Qualitative agreement with flight data in some areas, suggests that this type of approach could be used to correct count data in some circumstances.

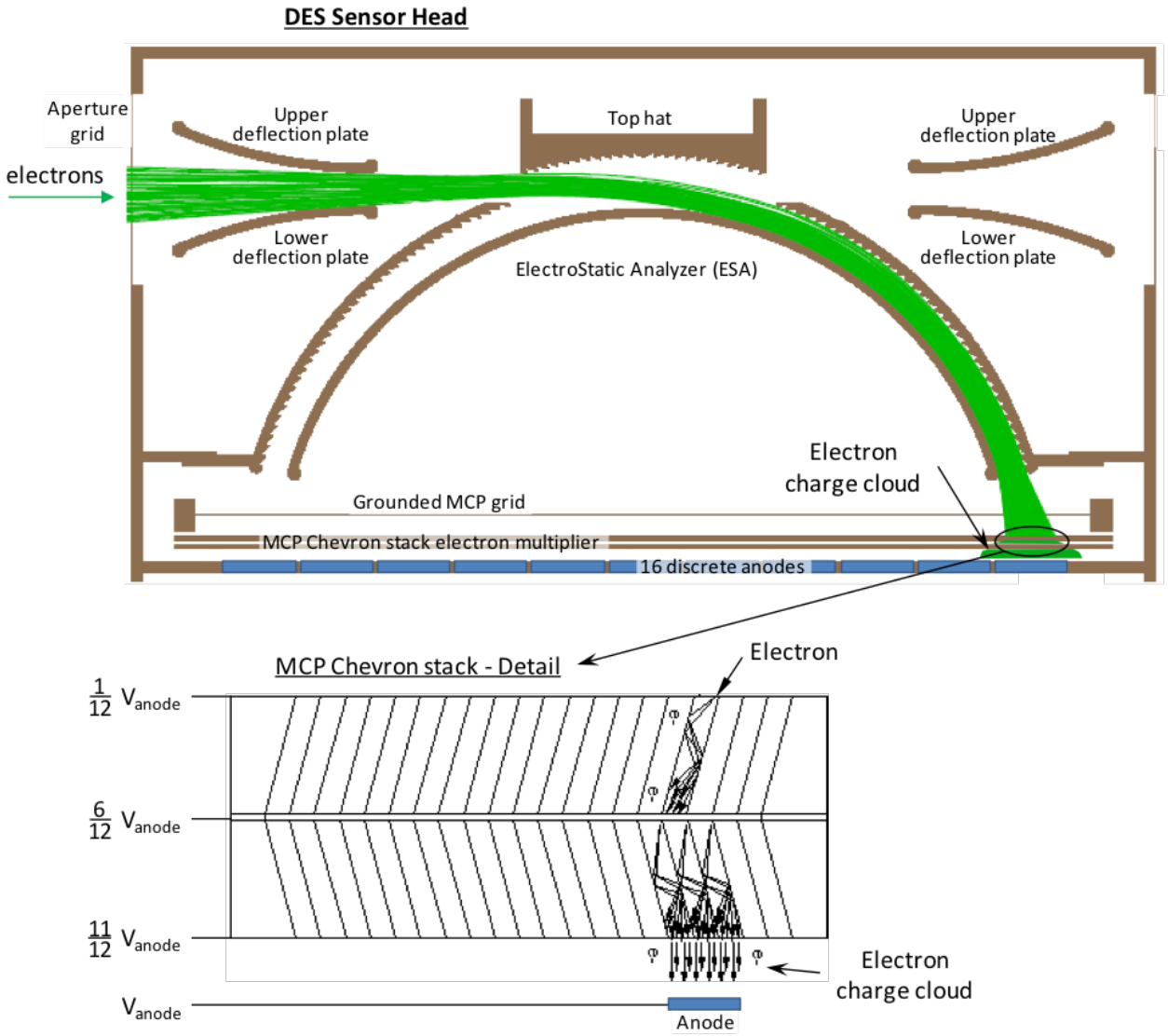

Figure 2.5: Illustration of DES top hat functionality. Particles (green) enter the aperture and are steered by the applied electric field to the MCP, where an electron cascade is created, resulting in a measurable signal on the anode pads[52].

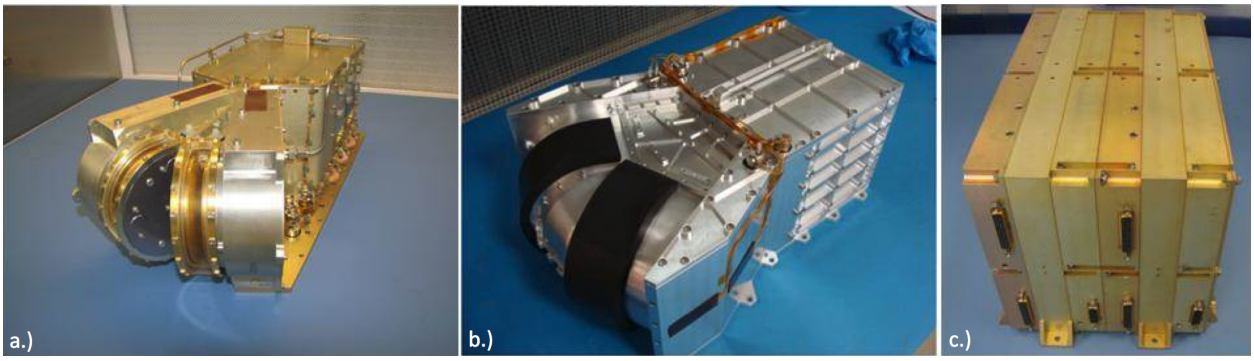

Figure 2.6: Views of the DES (a), DIS (b), and IDPU (c). These photos do not include final blanketing, harnessing, heaters, etc.[42]

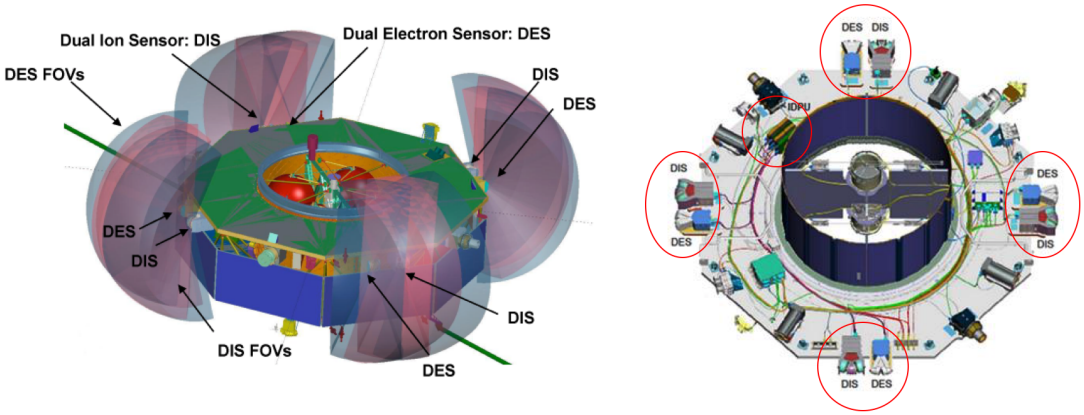

Figure 2.7: Field of view of DES/DIS (left) and instrument positions as shown on MMS instrument deck (right).[42]

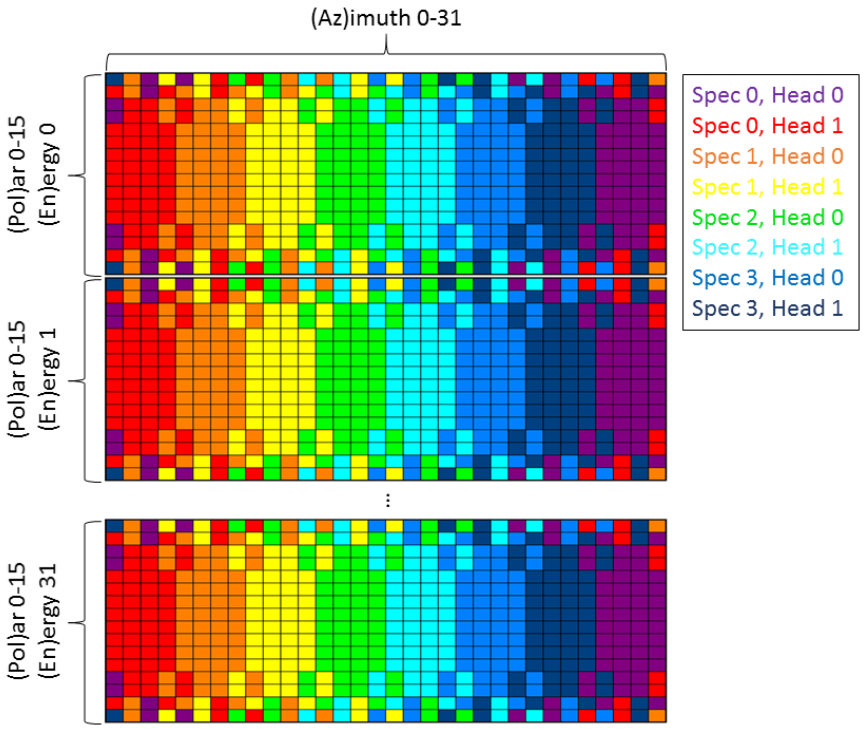

Figure 2.8: Pixel look directions resulting from rectilinear mapping of spherical coordinate system. Colors represent the pixels contributed by a given dual spectrometer. Note that, at the poles (top and bottom of panel), clear separation of spectrometers is no longer possible.[42]

Chapter 3

Predicting Errors Associated with Wavelet Data Compression

Portions of this chapter are taken from:

AC Barrie, S Elkington, Z Sternovsky, D Smith, B Giles, and C Schiff. Wavelet compression performance of mms/fpi plasma count data. **Journal of Geophysical Research: Earth and Space Science**, 2018. Under Review

and

AC Barrie, SE Smith, JC Dorelli, DJ Gershman, P Yeh, C Schiff, and LA Avanov. Performance of a space-based wavelet compressor for plasma count data on the mms fast plasma investigation. **Journal of Geophysical Research: Space Physics**, 122(1):765–779, 2017

3.1 Introduction

Plasma instrumentation has been measuring the magnetosphere for decades, and modern electrostatic optics have undergone only modest changes since their inception[11]. One area of rapid advancement, however, is the data capture rate and overall volume of data acquired. FPI captures data over 100 times faster than the previous CLUSTER[21] mission. These faster time resolution measurements enable scientists to observe phenomena that are spatially narrow or short in time duration, such as the electron diffusion region of a reconnecting magnetic field[10]. This increased data rate, however, leads to proportionally increasing data volumes that must addressed. There are three methods by which to deal with increased data volume:

(1) Increase bandwidth for data downlink

(2) Downlink a smaller fraction of collected data

(3) Compress data to a smaller size

MMS has followed all of these paths. As MMS has now completed three years of mission life, sufficient data is available to analyze the performance of the compression system and make recommendations for the next generation of instrumentation.

Each FPI skymap is compressed by the IDPU using a Discrete Wavelet Transform and Bit Plane Encoder (DWT/BPE)[65], designed to the CCSDS (Consultative Committee for Space Data Systems) 122.0 DWT/BPE standard[15]. CCSDS is a group responsible for defining standards to be implemented with regard to space data and information systems. The DWT organizes the image into a series of wavelets, with each successive wavelet resolving higher frequency, finer details in the image. The BPE truncates the series to a specified length and encodes the result. The wavelet compression algorithm is not new, and has been used in imaging missions in the past[17] as has a similar algorithm, JPEG2000[1], and others[60, 66]. The BPE algorithm, however, is specifically tailored for space applications due to its lower computation complexity and memory requirement.

Previous plasma instruments[40, 21] have historically relied on low compression ratios which were acceptable due to their lower data volumes. FPI is operating ~ 100 times faster than previous plasma instruments, however, and requires a higher rate of compression. FPI is therefore a proof of concept DWT/BPE based wavelet compression on plasma count data. In this way, truncating an image, or compressing it in a lossy manner, will lose the highest frequency data first and preserve large features.

Onboard FPI burst skymaps, which are fed into the compression algorithm as an image, measure 32 columns (azimuth) and 512 rows (32 energy and 16 elevation bins). The energy bins are logarithmically spaced from 2eV - 30keV for ions and from 6eV - 30keV for electrons. The compression algorithm supports either an integer based calculation or floating point calculation mode. This governs the data type used for internal mathematical operations. Compression error is marginally higher for integer mode than floating mode due to the loss of precision in mathematical

calculations in integer mode, but the integer mode compresses into a smaller size if the compression is lossless[65, 6]. The general approach taken is therefore to use integer mode compression when the majority of the data is expected to compress losslessly and floating point mode when the wavelet series is expected to be truncated (lossy data). The vast majority of FPI burst maps are compressed losslessly, thus supporting integer based compression for FPI burst data.

While FPI uses integer mode compression for burst skymaps due to the modest compression requirements, this work explores the viability of using floating point compression to drive the compression to smaller image sizes. This approach abandons the idea of fully lossless compression and assumes that some level of error is tolerable. Looking at a sampling of the entire operating range of MMS, plus an in-depth look at representative samples of the magnetosphere, this work guides future missions towards the expected performance that they can derive out of wavelet based compression. Finally, recommendations are given for when and where plasma count skymaps can be compressed heavily, and where they should be allowed to fill a larger volume. These recommendations will serve to inform future plasma instrumentation that will be relying on increasingly large data volumes compressed to smaller sizes.

The target compression ratio is the minimum compression ratio required to fit within the telemetry allocation. The DES and DIS produce data of 10 and 16 bits/pixel respectively. It is desirable that the same compression performance is obtained for both DES and DIS, thus the same compression ratio was chosen for both species for Phase 1A (See Section 2 for a discussion of the MMS phases). Due to reasons discussed herein, the ion data compressed more favorably than the electron data and the DES compression was relaxed for Phase 1B and beyond. The telemetry and the desirable compression ratio for DES and DIS in different modes are provided in Table 3.1.

Table 3.1: Compression allocation (on board storage, per skymap) for all data types. The DES burst compression limit was changed between Phases 1A and 1B to allow for more lossless DES burst data.

	Sky Map Volume (bytes)		Allocation (bytes)		Compression Ratio	
Data Type	DES	DIS	DES	DIS	DES	DIS
Burst	20480	32768	6087 (4433 in 1A)	7093	3.36 (4.62 in 1A)	4.61
Fast Survey	32768	32768	1964	1966	16.68	16.67
Slow Survey	16384	16384	3772	3772	4.34	4.34

3.2 Error Modes and Effects on Data

3.2.1 Macroscopic View of Magnetosphere

MMS has completed three years of mission life. This means that it has had three dayside passes, with two at an apogee of 12 R_E and one with an apogee of 25 R_E. Similarly, there have been three tail passes, one at 12 R_E and one at 25 R_E (the first tail pass was used for commissioning). Throughout this time, science data has been collected and downlinked as available. While not all data could be downlinked due to telemetry limitations, a significant portion of the highest resolution burst data has been acquired in nearly every operational region of the magnetosphere. The sum of all of this data was collected and binned for compressed image size vs temperature and density. These parameters were chosen as they are common metrics used to evaluate or identify plasma regions. The results are shown in Figure 3.1. The color denotes the size, in bytes, of the full series of wavelet terms needed to fully describe the image. This translates to the size of the compressed data file in the system. When the entire series is preserved, the data compression is lossless. When some terms are truncated, the data volume is reduced, but information is also lost, resulting in a lossy compression. Red areas denote times when the series was truncated by FPI and the resulting compressed image was lossy. The absolute numerical value of the compressed image size is highly dependent on instrument parameters and would not translate directly to future missions, however the trend is instrument agnostic. There is a clear trend of increasing density and, to a lesser extent, temperature leading to a larger image size. High densities ($> 100/cm^2$) still compress highly efficiently when at low temperatures. Similarly, even high temperatures can

compress well at lower densities. This shows instrument teams that DWT/BPE can achieve high compression ratios, while maintaining lossless data, at lower density, lower temperature plasmas. Lossless data can always be achieved, if given enough data volume. The required size in data volume for lossless data increases as the temperature and density increase. This is of particular importance for missions, such as MMS, that operate in different regimes in different phases of the missions.

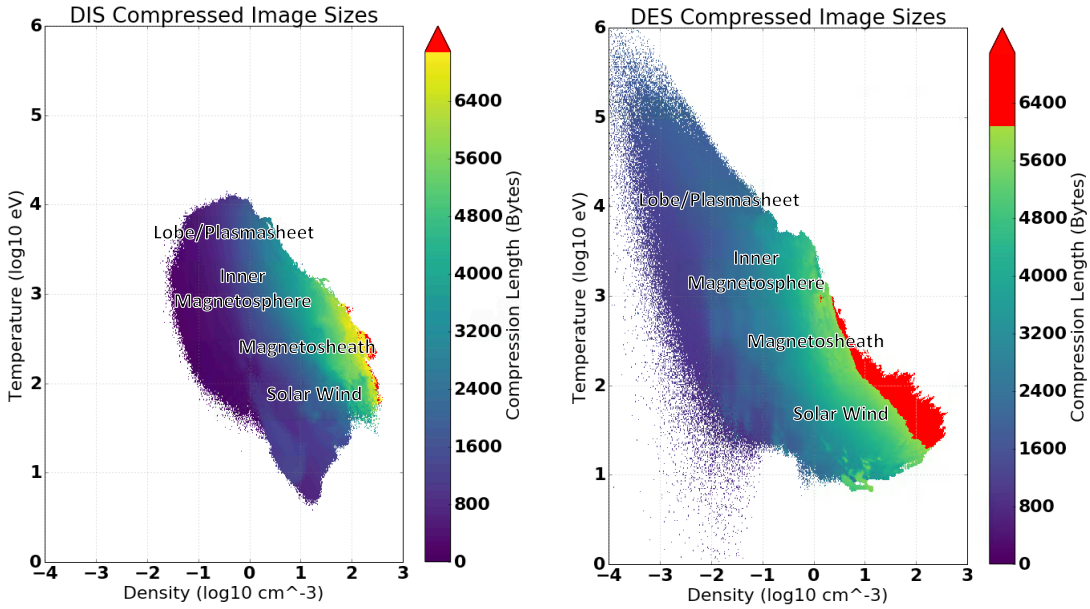

Figure 3.1: Histogram of all flight FPI flight data showing compressed image size as a function of local environment (temperature and density.) The compressed length (non-red coloring) denotes the compressed image size for the full series of wavelets and represents lossless compression. Red areas indicate lossy compression where original size cannot be determined due to a truncated wavelet series. DES (electron data, right) has a smaller truncation limit than DIS (ion data, left), hence more of the colormap is red. Notional areas of the magnetosphere are listed for reference. Note that the image sizes are for an FPI specific sky map image and hardware.

This is not to say, however, that large count values (higher density), or spatial spread (temperature) cause compression error, but rather that an increase in structure (entropy in the map) leads to poorer compression performance. This distinction is shown in Figures 3.2 and 3.3, which examines the entropy of every count skymap image in Phase 1A. These figures show a much clearer trend and via the relationship between compression performance and overall entropy in the map,

where entropy is defined as

$$E = -\sum_i P_i Log_2 P_i \tag{3.1}$$

and P_i is a probability matrix that the difference in counts of two neighboring pixels is equal to i, calculated from the histogram of the intensity of the image[26]. Good agreement is shown between the DES and DIS in terms of the relationship between entropy and compressed size, with DES generally having higher entropy and therefore increasingly compressed sky map image (file) sizes. Color represents the logarithmically spaced energy bin, as described in Appendix A. This relation helps to explain why the hotter temperature plasmas compress more poorly in that plasmas with a larger thermal speed will have greater variability between adjacent pixels, and therefore, why DES shows greater compressed sizes than DIS.

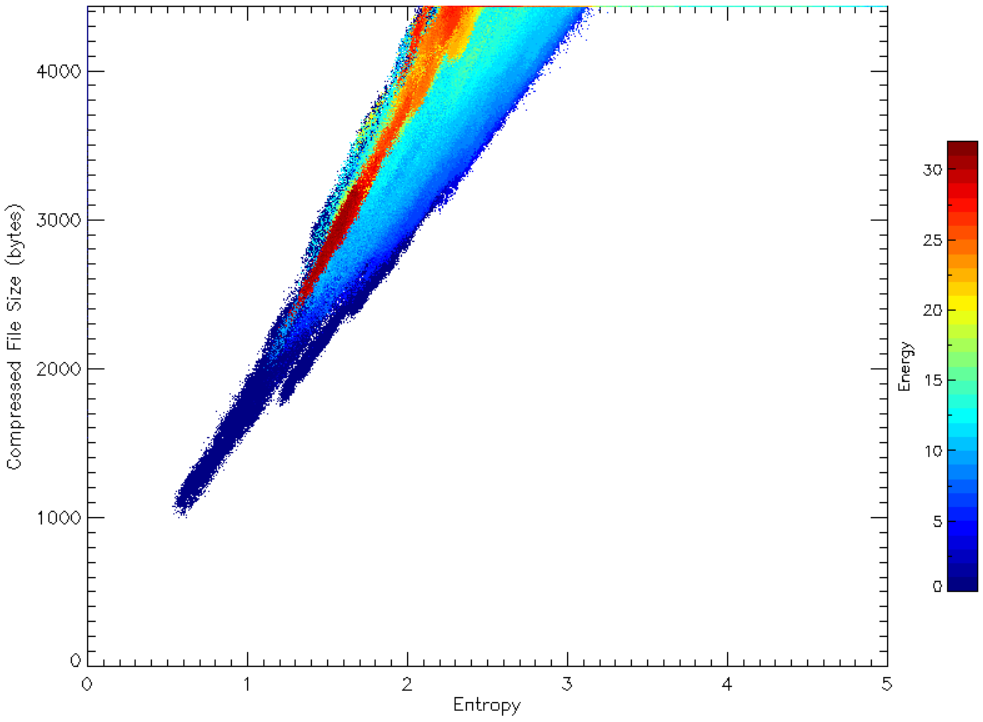

Figure 3.2: Flight results of DES compression performance over full day side pass (Phase 1A) as a function of image entropy. The compressed file size refers to the size of the compressed sky map image in bytes. Energy refers to the peak energy bin as described in Appendix A. Values in the uppermost row of the image represent truncated wavelet series and therefore lossy sky map images.

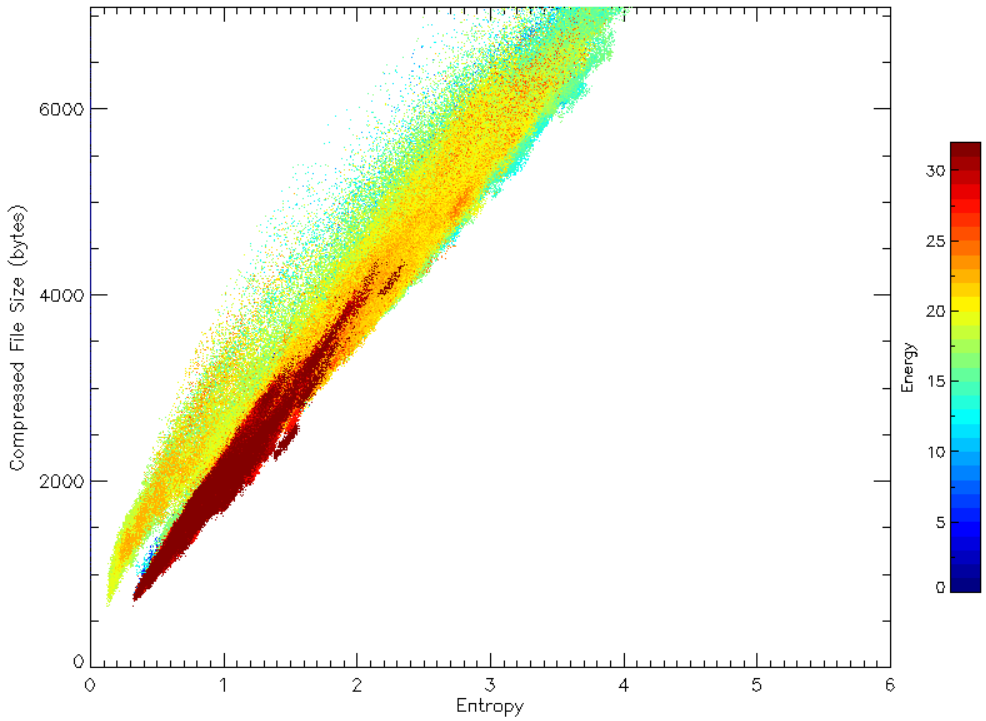

Figure 3.3: Flight results of DIS compression performance over full day side pass (Phase 1A) as a function of image entropy. The compressed file size refers to the size of the compressed sky map image in bytes. Energy refers to the peak energy bin as described in Appendix A. Values in the uppermost row of the image represent truncated wavelet series and therefore lossy sky map images.

Based on these findings, the compressed size limit of DES burst skymaps was increased prior to the start of Phase 1B to 6084 bytes. The updated limit was successful in allowing 99.5% of DES burst maps to come down losslessly, a similar rate to DIS. Figure 3.4 illustrates this distribution of sizes for DES burst data. The histogram shows the range of compressed skymap sizes for two months after the increase. The highest bin still shows that $\sim 0.5\%$ of the data was lossy (the high end tail of the distribution is collapsed into a single bin at the green line), however this is a huge improvement over the annotated black line (the initial limit), which would have resulted in over half of the data returned lossy.

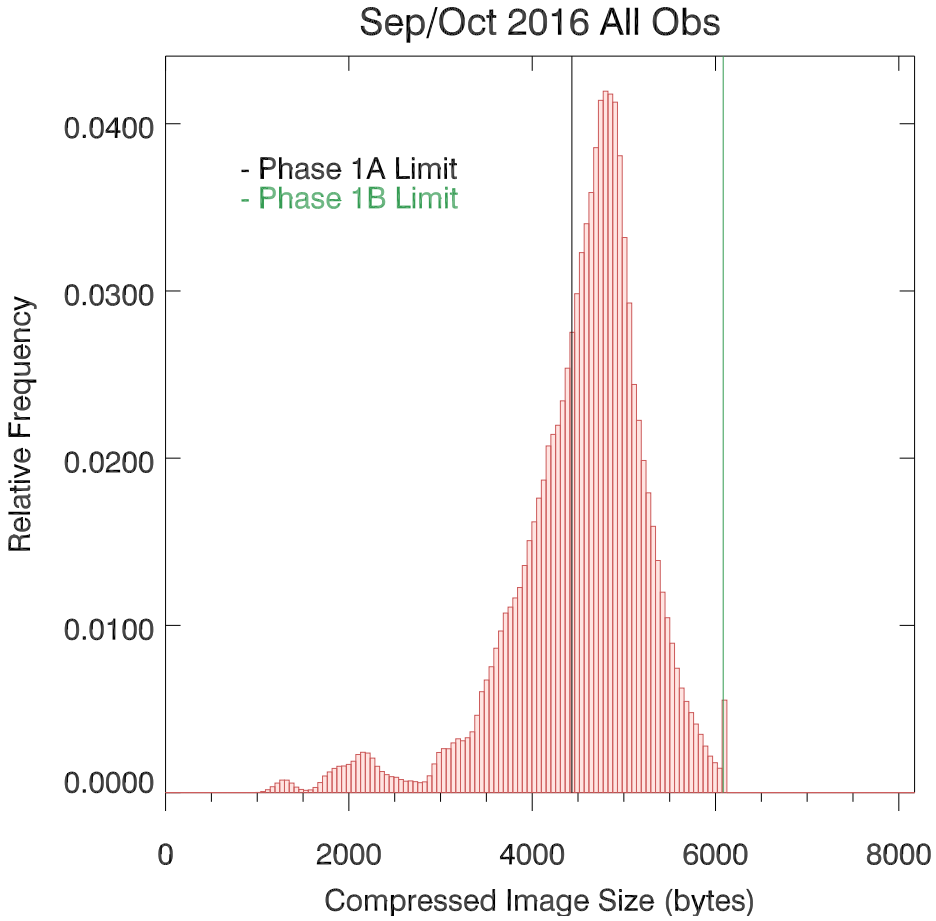

Figure 3.4: Histogram of initial DES burst data from Phase 1B using increased image size limit. 99.5% of burst maps thus far have been lossless. The last bin in the histogram (at the size limit denoted by the green line) represents lossy data. All data to the left of this is lossless.

3.2.2 Errors in Simulated Moment Data

The compression error typically has a small effect on plasma moments. Figures 3.5 and 3.6 show the bulk plasma parameters for a simulated spin of magnetosheath plasma for DES and DIS respectively compressed using the Phase 1A limits (see 3.1). Figures 3.7 and 3.8 show a simulated spin of magneotspheric plasma. The simulation input parameters are shown in Table 3.2. Random Poisson noise was applied to the maps, resulting in the variation in the moments over the course of the spin. For both of the DIS cases, there is no measurable difference in the moments between the pre and post compression sky maps. This is consistent with the notion that most DIS data

Table 3.2: Parameters used for simulation of single spin in magentosphere/sheath to examine effect of compression on plasma moments.

Case	Density (per cc)	Temperature (eV)
DES Magnetosheath	35	100
DIS Magnetosheath	35	900
DES Magnetosphere	1	50
DIS Magnetosphere	1	1000

compresses losslessly. Of more interest are the DES moments, which are composed of lossy sky maps. For typical magnetosphere and magnetosheath data, however, it is clear that there is a negligible, though nonzero, difference in the final plasma moments.

This is not to say, however, that compression error can never affect moments. Burst compression artifacts create features in burst maps at a fixed location in observatory frame skymaps. When de-spinning skymaps to convert to GSE, these fixed artifacts generate a feature in spacecraft azimuth that rotates at the spin period. These artifacts contribute to all moments generated through numerical integration of skymaps. In the dense magnetosheath ($n >> 1cm^{-3}$), such enhancements have very little impact on bulk plasma moments such as density, velocity, and temperature. In sparse magnetospheric plasma ($n < 1cm^{-3}$), countrates are so low that they do not generate strong compression artifacts, such that there is little impact of compression to plasma moments. In intermediate density magnetosphere ($n \approx 1cm^{-3}$) plasmas, phase space density associated with compression artifacts can occasionally be comparable to that of the ambient plasma. The effect of this is most pronounced in electron spin plane (V_x,V_y) bulk velocities, where there is an additional spin tone observed in the data. Imperfect correction tables[52] also produce a spin tone. One can distinguish between the two by comparing fast survey and burst FPI data, as the only difference between the two is their compression schemes. If the spin tone has similar amplitude and phase, then its origin is correction factor based. If the spin tone amplitude and phase shift between the burst and fast survey data, then the origin is compression based. This effect is illustrated in Figure 3.9, where the plasma density goes from 0.5 to $3cm^{-3}$ in the magnetosphere. Burst moments are averaged to fast survey time periods and compared. In the low density regions, where there are

no strong compression artifacts, the burst data precisely averages to the fast survey data. In the region of enhanced density (23:29 - 23:30), the burst and fast survey data diverge, with the burst data showing an increased spin tone amplitude in V_x and V_y. This increase is due to compression artifacts such as shown in Section 3.3.

While the effects of compression error on plasma moments can, on most occasions, be considered negligible, one of the main focuses of MMS, and FPI in particular, is to examine localized, subgyroperiod behavior of the particles. In this case, individual sky maps are often examined and errors in individual count rates become important. This class of error modes is discussed in detail in Section 3.3.

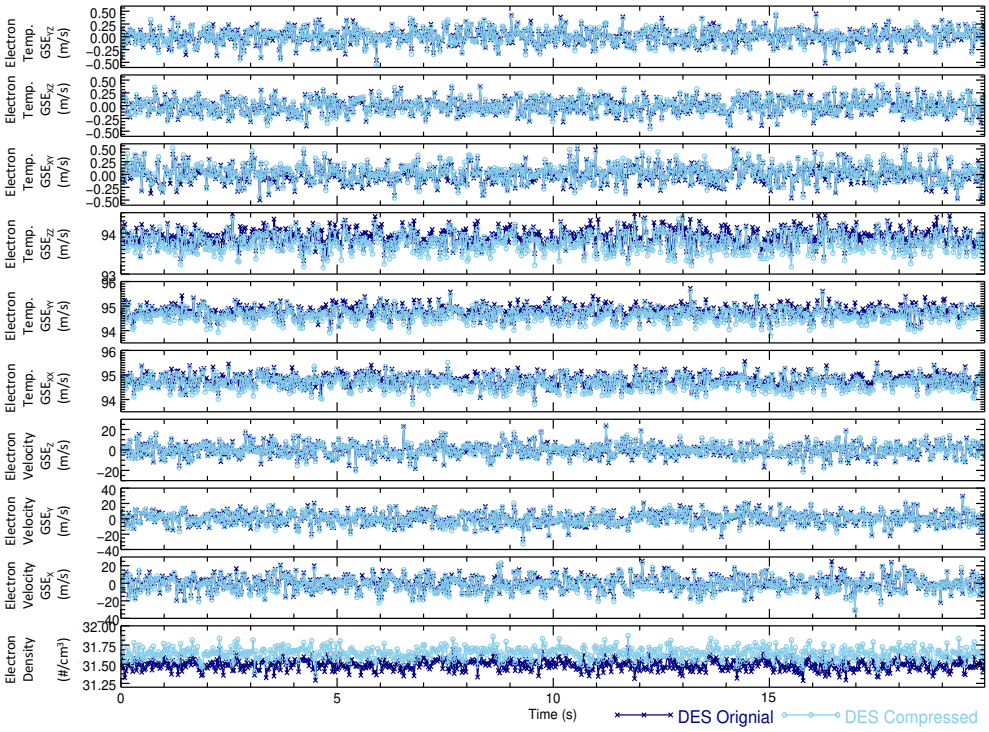

Figure 3.5: Simulation of a single spin of DES moments (density, velocity vector, temperature tensor) in the magnetosheath. Moments from original sky maps are compared to moments from maps that have been compressed and decompressed.

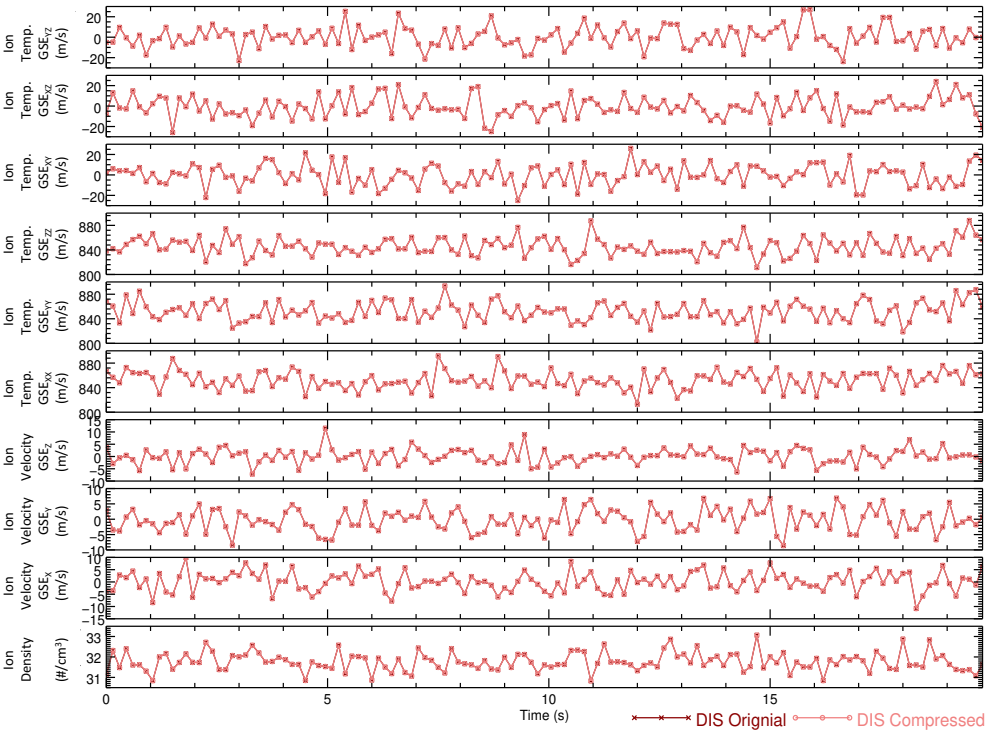

Figure 3.6: Simulation of a single spin of DIS moments (density, velocity vector, temperature tensor) in the magnetosheath. Moments from original sky maps are compared to moments from maps that have been compressed and decompressed. Note that the two lines are coincident, making the original line obscured.

3.2.3 Exploration of Error Modes Using Simulated Data

3.3 Error Modes

A discussion of error modes observed during testing is provided here, where an error mode is defined as the change in reported counts in a specific and recognizable way. The error is classified into two categories: **observable**, which are easily noticed in a single map and **subtle**, which only become readily apparent when looking statistically over many maps. Because flight data is only returned in the compressed form, the original map cannot be known (unless the map is marked lossless). For this reason, simulated sky maps were used for the investigation of error modes (with the exception of where burst data are compared to fast survey data and flight data can be used). The simulated maps were derived from a hot Maxwellian background plasma with density varying

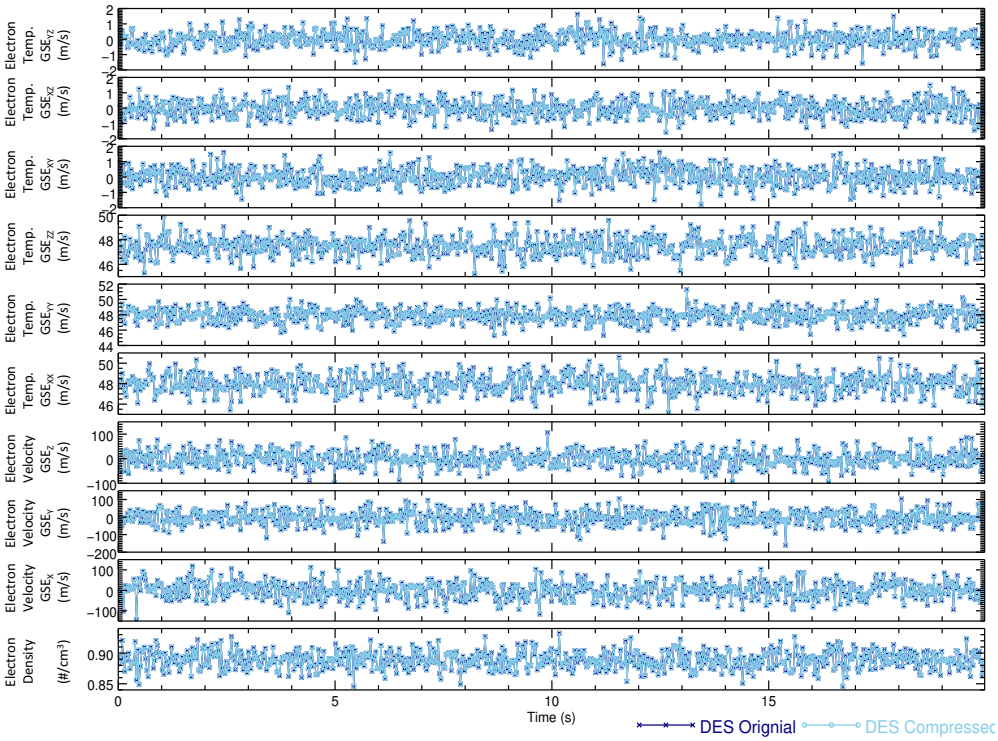

Figure 3.7: Simulation of a single spin of DES moments (density, velocity vector, temperature tensor) in the magnetosphere. Moments from original sky maps are compared to moments from maps that have been compressed and decompressed.

from 0.1 - 25/cc, and temperature from 5 - 5000 eV.

3.3.1 Observable Error

Observable errors are large differences between pre- and post-compression count rates present in a single map. These types of errors are the most serious in terms of scientific impact, however they only occur when compression performance is stressed in terms of count rates and distributions within the map.

Smearing The compression algorithm does not handle large gradients (e.g. delta/step functions) well. Figure 3.10 shows this effect using a high count rate sky map with significant angular structure. The original simulated sky map shows several regions of over 900 counts, which quickly drop to $\sim$ 400 counts over the course of 2 angular bins. The map illustrated here has a peak count rate of over 4 MHz, which is unrealistic for FPI due to saturation of the Micro Channel

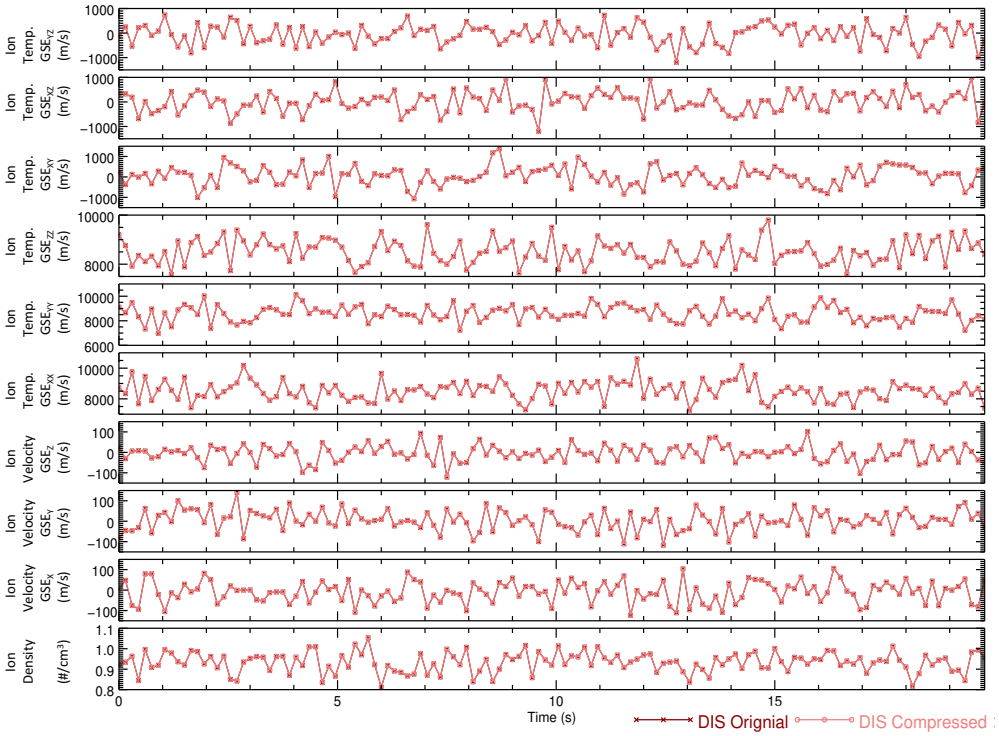

Figure 3.8: Simulation of a single spin of DIS moments (density, velocity vector, temperature tensor) in the magnetosphere. Moments from original sky maps are compared to moments from maps that have been compressed and decompressed. Note that the two lines are coincident, making the original line obscured.

Plate detectors (MCPs) around 2 MHz. The smearing was not seen with count rates closer to 2 MHz and similar angular structure. This error mode is therefore not a concern for operation of FPI or in analysis of FPI data. This was demonstrated, however, during ground testing using artificial test pulses into the FPI sky map acquisition system and should serve to inform future missions.

Noise Floor During the prime region of interest, FPI produces two data products: burst maps are collected every 30 ms/150 ms for electrons and ions respectively and fast survey maps sum up the (uncompressed) burst maps over the course of 4.5 s. All fast survey data is downlinked to the ground and is used to help prioritize which burst data to downlink, as well as for science investigation. The fast survey maps are compressed to a rate of 16.67:1 whereas the burst maps are compressed to 4.62:1. Due to the higher counts from summing and the increased compression ratio, the fast survey maps have substantially higher compression error than the burst maps. In

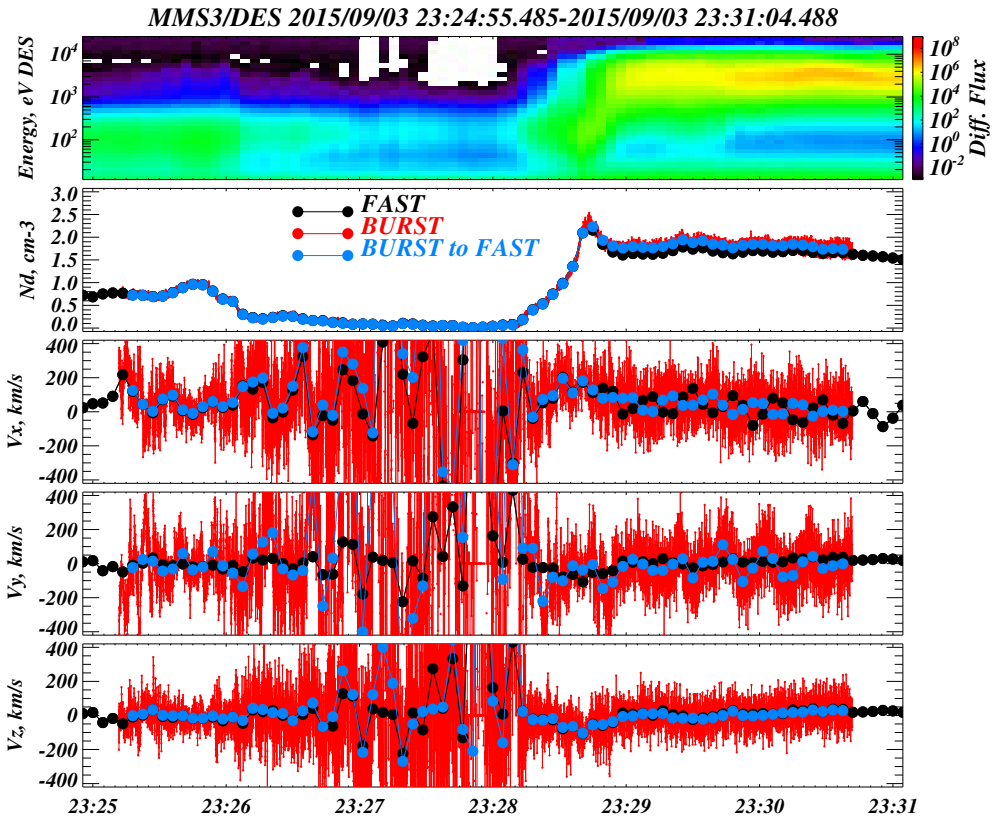

Figure 3.9: Flight data showing illustrating a difference in spin tone between summed bursts (blue) and fast survey (black) introduced by compression error (23:29 - 23:30). Uncertainty in earlier time interval is due to low counting statistics.

this case of high compression, an error mode is evidenced where the noise floor (lowest measurable count rate) of the sky map is elevated. This is illustrated in Figure 3.11. The total counts of two energy bins in a sample DES fast survey sky map (black) are compared to a manual sum of the bursts used to compose the FS map (red.) If no error were present, the single fast survey map would exactly match the integrated bursts and these two lines should lie on top of each other. This is the case in the higher count energy bin (top panel). For the lower count rate energy bin (lower panel), however, the agreement breaks down below 800 Hz. The fast survey image shows a noise floor that is not present in the summed burst maps. While this type of error can change the interpretation of data in a general sense, the fast survey product is compressed so significantly

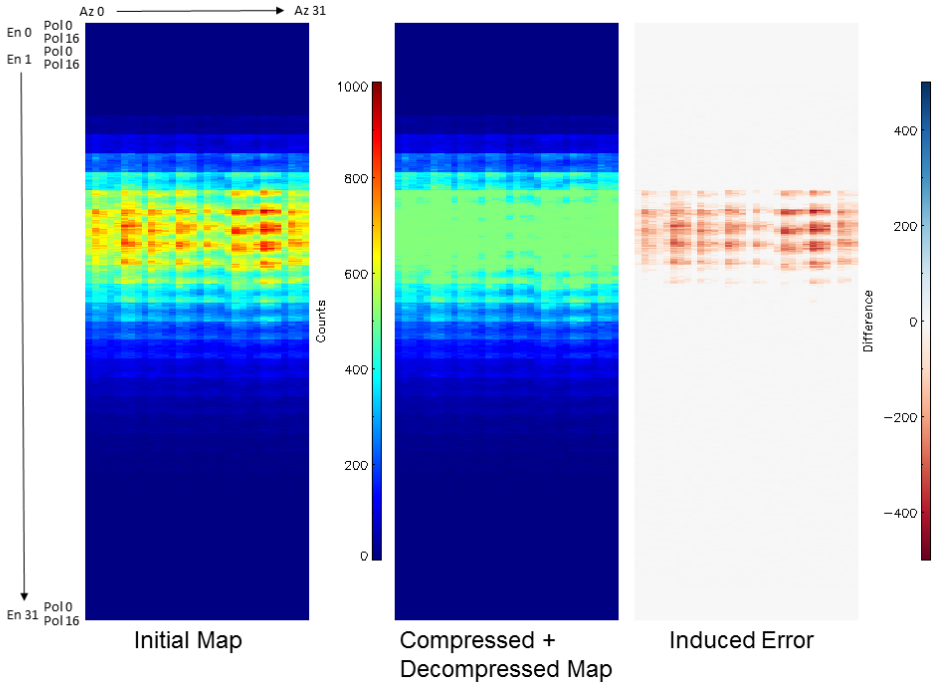

Figure 3.10: Smearing of large gradients. Original sky map (left), post compression/decompression sky map (center), and difference map (right). The sharp, steep gradients in the original map have been reduced, effectively blurring the sky map.

because it is intended to be a guide for which burst data will be of interest. The noise floor does not inhibit the fast survey maps in that function. Furthermore, the one count level in a DES burst map is 5 kHz. The noise floor in the FS map is therefore less than 20% of the one count level at the burst resolution.

3.3.2 Subtle Error

Subtle errors are not always obvious in a single map, but become evident when looking at a statistical sample of maps - a tendency of small, seemingly random errors to appear in a similar way over many maps. For example, a tendency in one area of the map to have a positive (increased count rate) vs a random error pattern. The results in this section represent difference maps summed over many samples in an effort to bring out statistical anomalies.

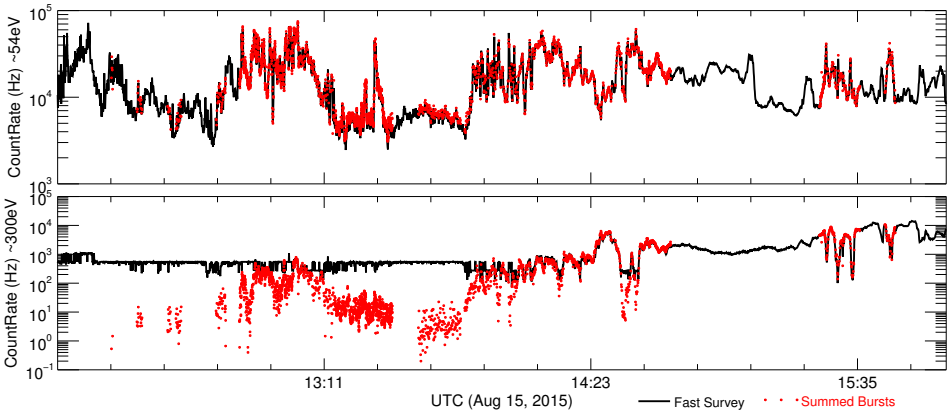

Figure 3.11: Observed electron counts for MMS4 for a given range at two energy slices: 54 eV (top) and 300 eV (bottom). Counts recorded in the Fast Survey product (black) are compared to the summed Burst data (red). The fast survey data is compressed more than the burst data and suffers from increased error, and does not match the (correct) burst data in all cases. Note: burst data is not available for all time periods.

Checkerboarding Higher frequency data in the wavelet domain will be truncated first if the compression is lossy. Because the highest wavelet transform frequency corresponds to alternating single column/row information[15], the loss of this frequency can result in a vertical striping, or to a lesser degree, checkerboarding effect in the final decompressed map. An example of this is shown in Figure 3.12. 1000 individual sky maps were compressed and decompressed. Each compressed/decompressed map was subtracted from the corresponding original map to generate an error map for a given sky map. The checkerboard effect is inherent in the compression algorithm (in both integer and float modes) and cannot be easily removed, however it is a small effect. A statistical anomaly of +/- 30 counts in error is shown here, which corresponds to 1000 summed error maps, each with ~ 150 counts in the relevant pixels. In any individual map, the error is $<< 1$, meaning that most pixels have an error of 0, and occasionally, an error of 1 (or -1) is present. This leads to a statistical error well below the level of Poisson statistical noise, which can typically be ignored in individual measurements. One must take note of this effect when summing burst maps to uncover subtleties in the plasma that lie below the one count level, however. It should be noted that although error tends to be biased with the checkerboard pattern, the overall integrated mean

count rate in an image remains unchanged.

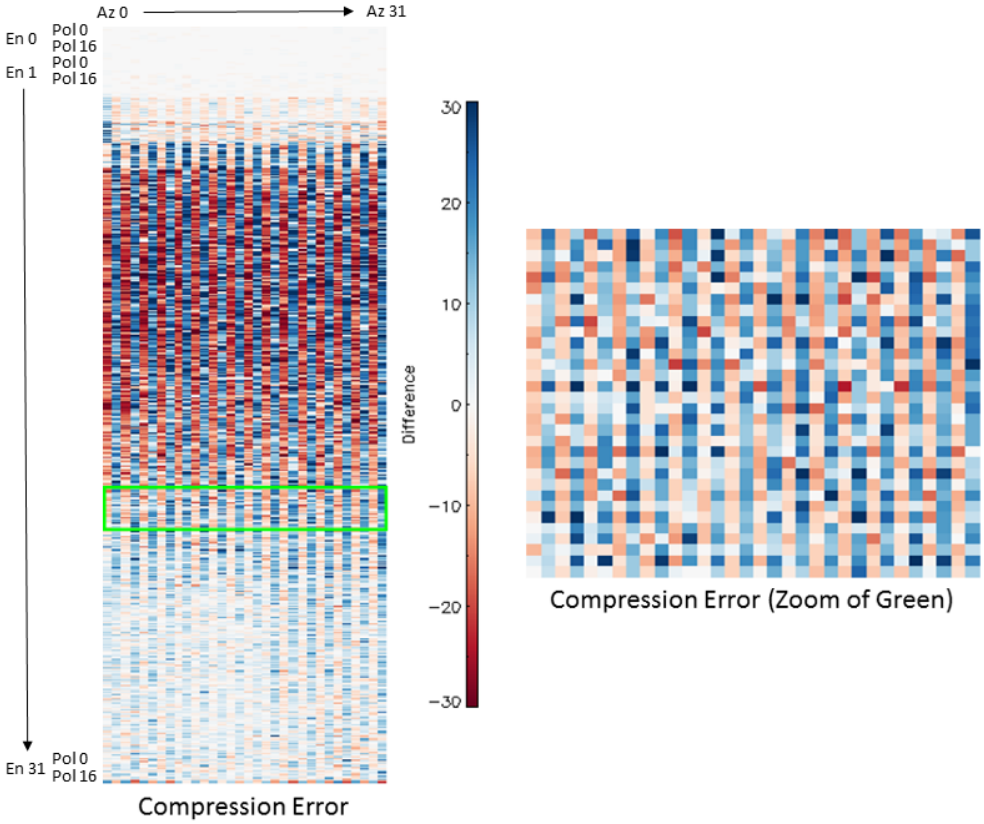

Figure 3.12: Difference map showing a checkerboard pattern (left) introduced by the compression algorithm. A zoom in of the area enclosed in green is shown (top right).

Artifacts Count errors can be biased in one direction (increased or decreased counts) in groups such that artifacts can appear in images after compression. A summed difference map shown in Figure 3.13 illustrates this effect. These statistical artifacts can appear for two reasons:

(1) In low count regions (mostly 0s), errors will tend to be positive because a count can never be negative. This effect can be compounded by the fact that a single count error is more noticeable in low count regions.

(2) The bit plane encoder compresses the wavelet transformed image (in this case, the 32x512 frame) from one corner of the wavelet image, crossing horizontally, then proceeds down the frame. For this reason, one side, or a corner of an image may tend to have slightly higher

error if the size limit is reached mid-image. While this behavior does exist in both Float and Integer modes, using Float mode can sometimes mitigate this effect as shown in Figure 3.13. The same simulated hot Maxwellian sky map is compressed to a ratio of 4.67:1 in both modes with the integer mode showing a dark artifact on the left. The entire bottom section of both maps tends to be blue, which is an example of the above point involving low count regions. The integer mode, however, has an additional dark blue region on the left side of the map that is indicative of the frame processing described here. The floating point map not only removes the dark blue artifact, but also reduces the checkerboarding to some degree. For this reason it is recommended to use floating point mode when high count rates are expected.

Artifacts present in low count rate regions are the most problematic error mode for the interpretation of FPI data. These artifacts are typically a 0 being changed to a value of 1, which when accumulated, can lead to errors in calculations in low count rate regions.

Poisson Redistribution The most common, and also most benign, form of compression error is redistribution of background noise, as shown in Figure 3.14; a simulated Maxwellian distribution compressed to a ratio of 4.67:1 and decompressed. This noise redistribution is characterized by a random distribution of added or lost counts that is not biased toward any particular feature or region of the sky map. The last bit plane contains the finest details in an image (i.e. noise). Bit planes that are truncated will therefore affect the background noise first, before important features are lost. This noise redistribution is essentially random with zero mean and the integrated mean is preserved. This allows small features that lie within the noise floor to be recognized by summing maps in a normal fashion, albeit with some loss of precision.

3.3.3 Performance with Increased Compression

The survey shown in Figure 3.1 is for the nominal FPI configuration, where the truncation limit was set sufficiently high that most data was returned losslessly, retaining the entire wavelet

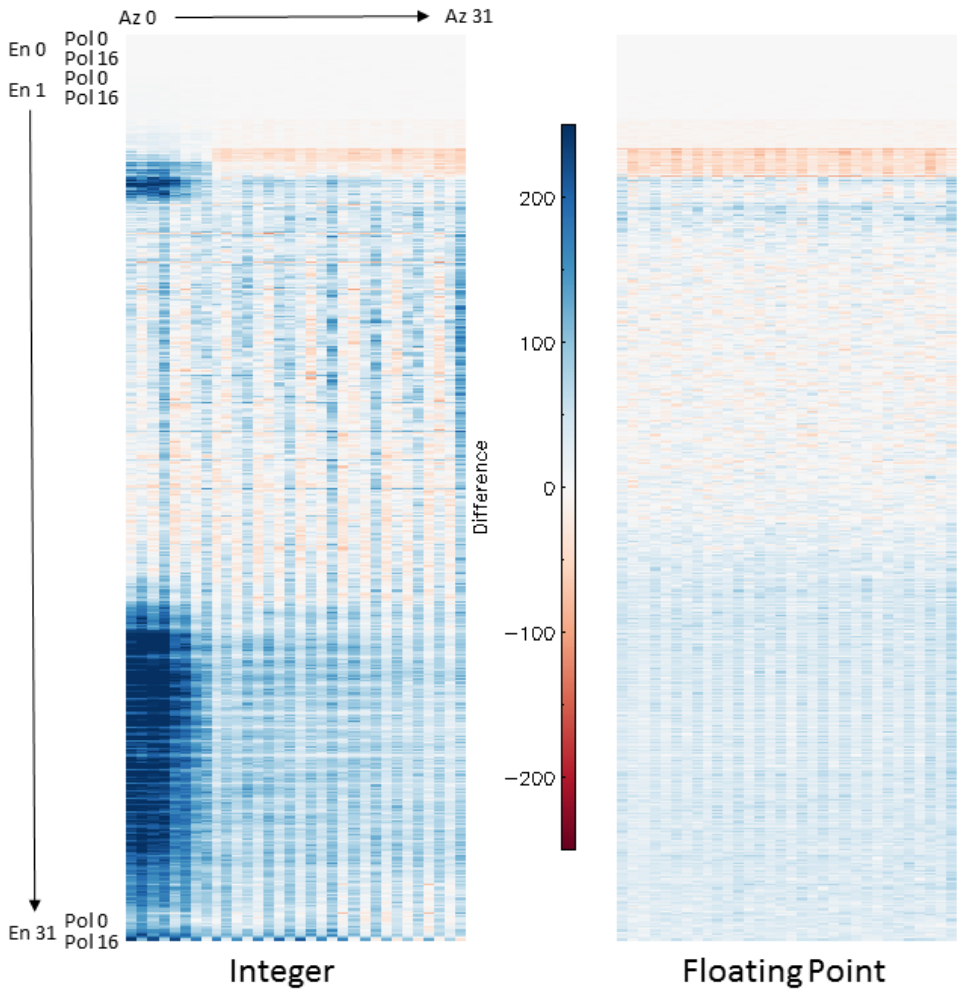

Figure 3.13: Difference map showing artifacts introduced in low count regions, present in integer mode (left) and not present in floating point mode (right).

series, and Section 3.2.2 examines the effect of the nominal compression rates on plasma moments. It may be required in future missions, however, to push the compression down to lower data volumes into the regime where truncation of the series occurs and data becomes lossy. The highest frequency data is at the end of the wavelet series, meaning that the bit plane encoder will truncate highest frequency data (noise) first. Truncating successively more terms leads to lower frequency information being lost, up to a point where the signal is no longer meaningful. In between a negligible redistribution of noise and total loss of signal shape, there are several error modes that may or may not be tolerable depending on the mission.

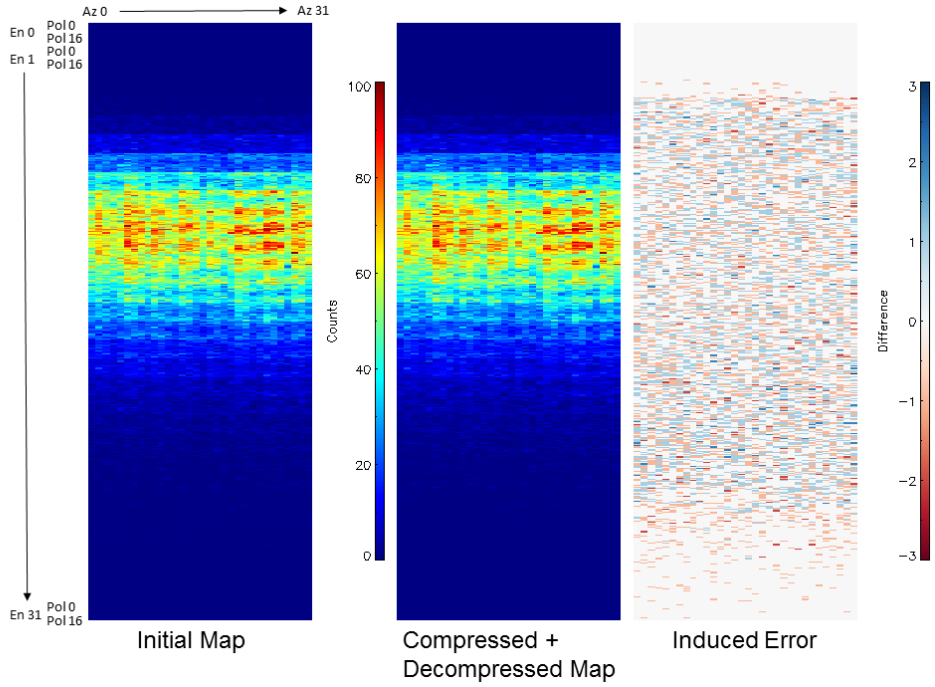

Figure 3.14: Effect of background noise redistribution. Original sky map (left), post compression/decompression sky map (center), and difference map (right).

In order to quantify the effect of this truncation, we define an error term, ε is defined as:

$$\varepsilon = \sqrt{\frac{\sum_{i=1}^{32}\sum_{j=1}^{16}\sum_{k=21}^{32}\left|c'_{ijk} - c_{ijk}\right| c_{ijk}}{\sum_{i=1}^{32}\sum_{j=1}^{16}\sum_{k=21}^{32} c_{ijk}^2}} \tag{3.2}$$

where c are the raw counts, c' are the counts after compression/decompression, and i, j, and k represent the indices of the energy, elevation angle, and azimuth angle, respectively. This error metric is designed to emphasize errors in areas of high counts as those tend to be the areas of most interest. Errors in areas of low counts are therefore depressed. In contrast, a raw RMS type of error would result in all error being treated equally regardless of scientific impact. For example, a raw RMS error would treat a Poisson noise distribution equally to a major change in shape of a key feature in an image assuming similar total change in counts. Our metric attempts to weight the error to the prominent features of the skymap image by focusing more on higher count areas.

As explored in Section 3.3, the error modes that appear with increasing error are:

(1) **Redistribution of Noise** can alter signals present below the noise floor, but is generally benign as it is at the level of Poisson statistical noise

(2) **Checkerboarding** can preferentially affect alternating pixels, resulting in an error with a checkerboard type of appearance. This can be noticeable, but again at a low level and largely benign.

(3) **Artifacts** are large contiguous areas of an image that are all altered in a similar way, such as changing a block of 0s to a block of 1s. These are typically single count errors, however, and are only important if one is interested in extremely low signal areas of the image. This is the level at which the integrated mean of the image may no longer be preserved.

(4) **Elevated Noise Floor** adds a uniform background level to the entire image, raising the count floor. This does not affect major features because it is a small count level, but it does significantly raise the total integrated mean and loses all knowledge in low count areas.

(5) **Smearing** is the most severe effect and occurs when the lowest frequency wavelets begin to be affected. In these instances, major features of the image are blurred together.

As a qualitative measure of the error defined in Equation 3.2, a value of $\varepsilon \sim 0.3$ is where *artifacts* start to appear in the data. This is the point at which the integrated mean of the image may no longer be accurately preserved, i.e. plasma moments may be affected, however the overall shape and structure of the image are reliable. Below this limit, error tends to be simple noise redistribution consistent with Poisson statistical noise. A value of $\varepsilon \sim 0.6$ is where *smearing* starts to occur. Smearing represents the loss of large gradients in the image as features get blurred over multiple pixels. This is the point where the wavelet series has been truncated to such a degree that even large structural parts of the image are no longer recoverable.

These levels are illustrated with Figures 3.15 and 3.16, showing a partial magnetopause crossing from December 29, 2016. The raw, lossless data was gathered by FPI as raw count arrays. As in Figure 3.1, this raw data was not a constant size, but varied in size per the length of the

wavelet series. The data was then compressed to successively smaller sizes, from 6000 bytes down to 200 bytes, as shown in Figure 3.16. The increased compression was performed using the floating point operational mode, as this is recommended for high levels of compression[65, 6]. At each compression level, the error, ε was calculated per Equation 3.2 for all data. Two contours of constant error are shown in white, representing error traces of $\varepsilon = 0.3$ and $\varepsilon = 0.6$. Note that this does not imply a constant rate of compression - the actual image size resulting in a given error varies based on the environment, particularly during the crossing of the magnetopause from 04:02:29 to 04:03:04.

The data correlating to the contours of constant error, in addition to the lossless data, were then processed to produce plasma moments shown in Figure 3.15. Moments from the three different levels of compression shown in Figure 3.16 are illustrated in Figure 3.15 as: lossless, C_L, a lower error level of $\varepsilon = 0.3$, $C_{0.3}$, and a higher error level of $\varepsilon = 0.6$, $C_{0.6}$. What is seen in these energy time (ET) spectrograms is that the low compression error ($C_{0.3}$) cases show some losses of counts in the high energy low density regions where the compressed image size is smallest (04:02:29 to 04:03:04, Fig. 3.16) and that the higher compression error ($C_{0.6}$) cases show lowered counts in almost all low density regions (higher energy range) and the beginnings of elevated counts in some areas, particularly in the ions (see darker orange coloring during magnetopause crossing and earlier.) This is caused by the peak of the distribution smearing into neighboring bins, elevating counts over a broader area. Note that the error metric defined in Equation 3.2 places an emphasis on error in high count regions, which is why the low error case shows some loss of counts in the ET spectrogram while still maintaining constant error. This targeting of high count rate regions, however, allows for a closer representation of error in the integrated moments. Note that for the velocity, temperature, and density integrals, the $C_{0.3}$ low error case generally tracks the integrated moment, although with some elevated jitter. This illustrates that a value of $\varepsilon = 0.3$ is just at the limit of where integrated plasma moments are preserved accurately. In contrast, the high error case is often systematically offset from the lossless line, particularly in the case of the ions. It should also be noted that, while the defined error is constant along these lines, there is a clear difference in

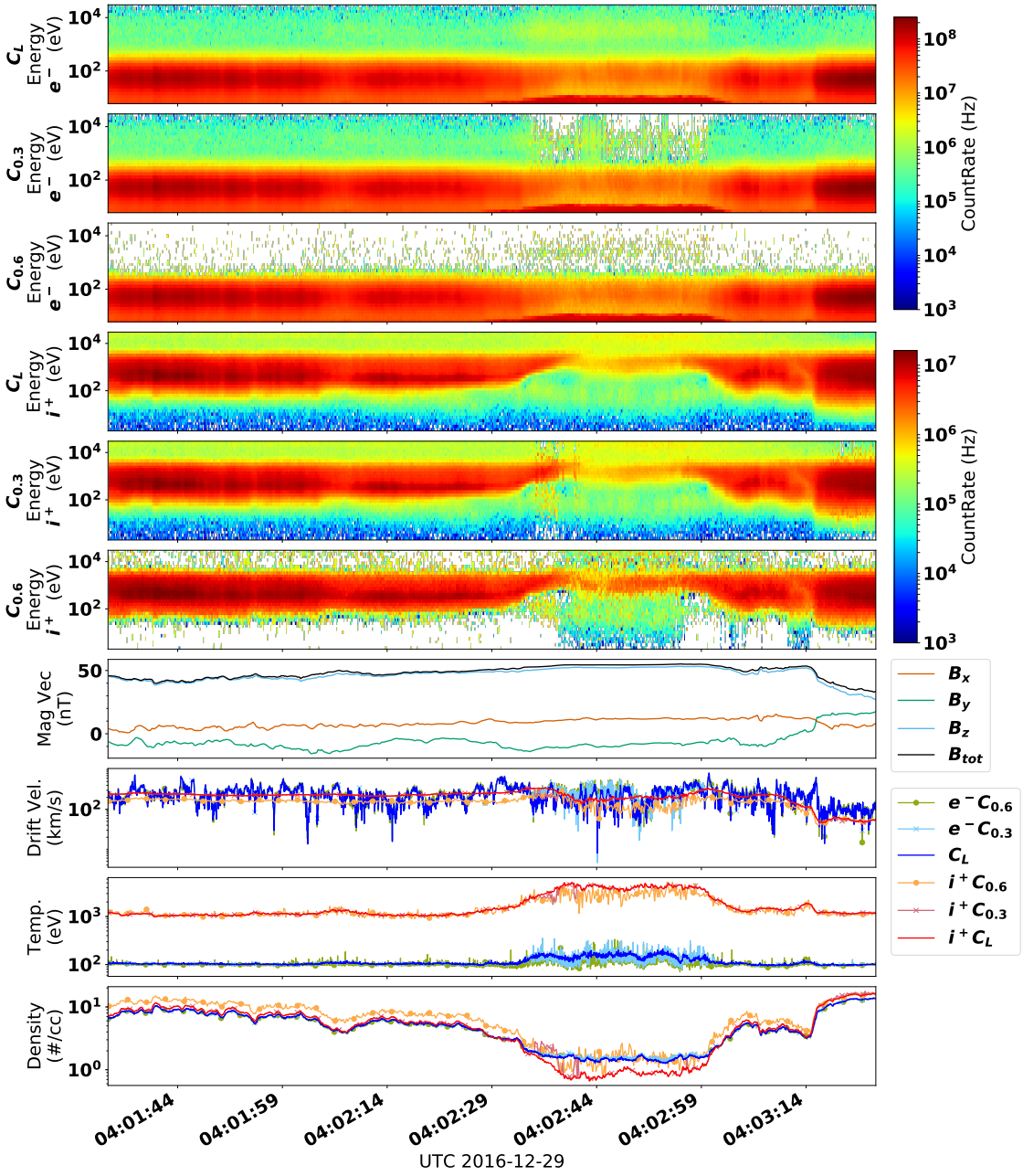

Figure 3.15: Plasma moments calculated for a partial magnetopause crossing from December 29, 2016, ([65.6k, -13.9k, -44.9] km GSE). Analysis run for both electrons (e^-) and ions (i^+) at three levels of compression: Lossless, C_L, constant error of $\varepsilon = 0.3$, $C_{0.3}$, and constant error of $\varepsilon = 0.6$, $C_{0.6}$. $C_{0.3}$ represents the point where the integrated mean of counts may no longer be preserved. $C_{0.6}$ represents the point where major features of the distribution may be lost. Error, ε, is defined by Equation 3.2.

quality when the magnetopause crossing occurs and the image size is drastically reduced (04:02:30

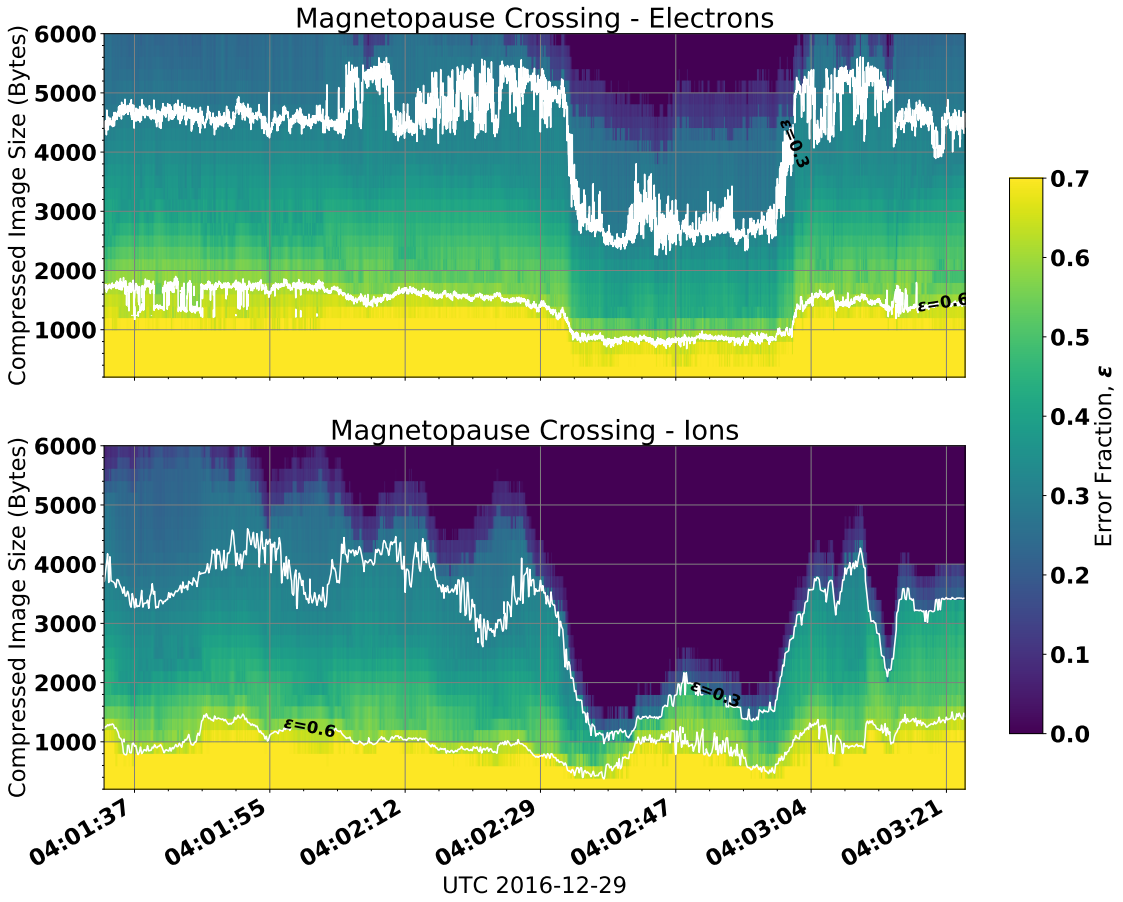

Figure 3.16: Compression performance on typical magnetopause crossing from December 29, 2016 for electrons (top) and ions (bottom). White traces indicate lines of constant error at $\varepsilon = 0.3$ and $\varepsilon = 0.6$. Error is calculated as in Equation 3.2.

- 04:03:00) as evidenced by increased jitter and occasional separation of the lossless and $C_{0.3}$ lines.

In addition to the magnetopause crossing, lossless FPI skymaps were taken from several other regions of the magnetosphere and then compressed to increasingly smaller sizes using the floating point mode of operation. Each region chosen represents data flagged by the MMS *Scientist In the Loop*[9] (SITL). These selections are therefore representative of the regions specified, however are also of particular scientific interest making for a good baseline comparison for future missions. The below plots show the $C_{0.3}$ and $C_{0.6}$ constant error traces for reference, however the integrated moment plots show only the reference lossless data for brevity.

Generally speaking, the ion data compresses much better than the electron data. This is for

two reasons:

- Different distribution functions and speeds for a given energy result in lower ion fluxes to the instrument.
- Electrons have a higher ratio of thermal velocity to drift velocity. This results in a broader angular distribution in the image, which is harder to compress as more pixels in the image contain count information.[6]

While the ion data in many of the preceeding cases has little or no error for much of the parameter space, it is important to note that the error increases rapidly once it does appear. The electron error starts at modest sizes, but the increase in error is slow. The ion data, by comparison, shoots from no error into the smearing region almost immediately. This is because the ion wavelet series are shorter (easier to compress), thus no error down to small sizes. When truncation does occur, however, a small truncation of the series is a larger fraction of the information, therefore the error rises rapidly.

Solar Wind Figure 3.17 shows a solar wind interval from December 7, 2016. This interval was marked as interesting due to a magnetic field reversal about midway through the interval, accompanied by an elevated temperature and density in the electrons; signatures often associated with magnetic reconnection regions. The compression performance of this interval is shown in Figure 3.18. This example illustrates the difference in compression performance between a largely thermal plasma in the electrons, versus a cold beam in the ions. This makes sense, as compression performance scales well with overall entropy in the image (Fig. 3.2, 3.3.) The ion counts are highly localized spatially, resulting in a large fraction of the ion image containing little or no data, which is easy for the system to compress. This leads to a short series of wavelets required to encode the entire image, allowing the compression to have no error down to a small fraction of the initial size. Both the electron and ion data do show a small uptick in error around the location of the magnetic field reversal indicating some change in the ambient plasma as well, resulting in a higher entropy.

Magnetosheath Figure 3.19 shows a selected interval of magnetosheath plasma from

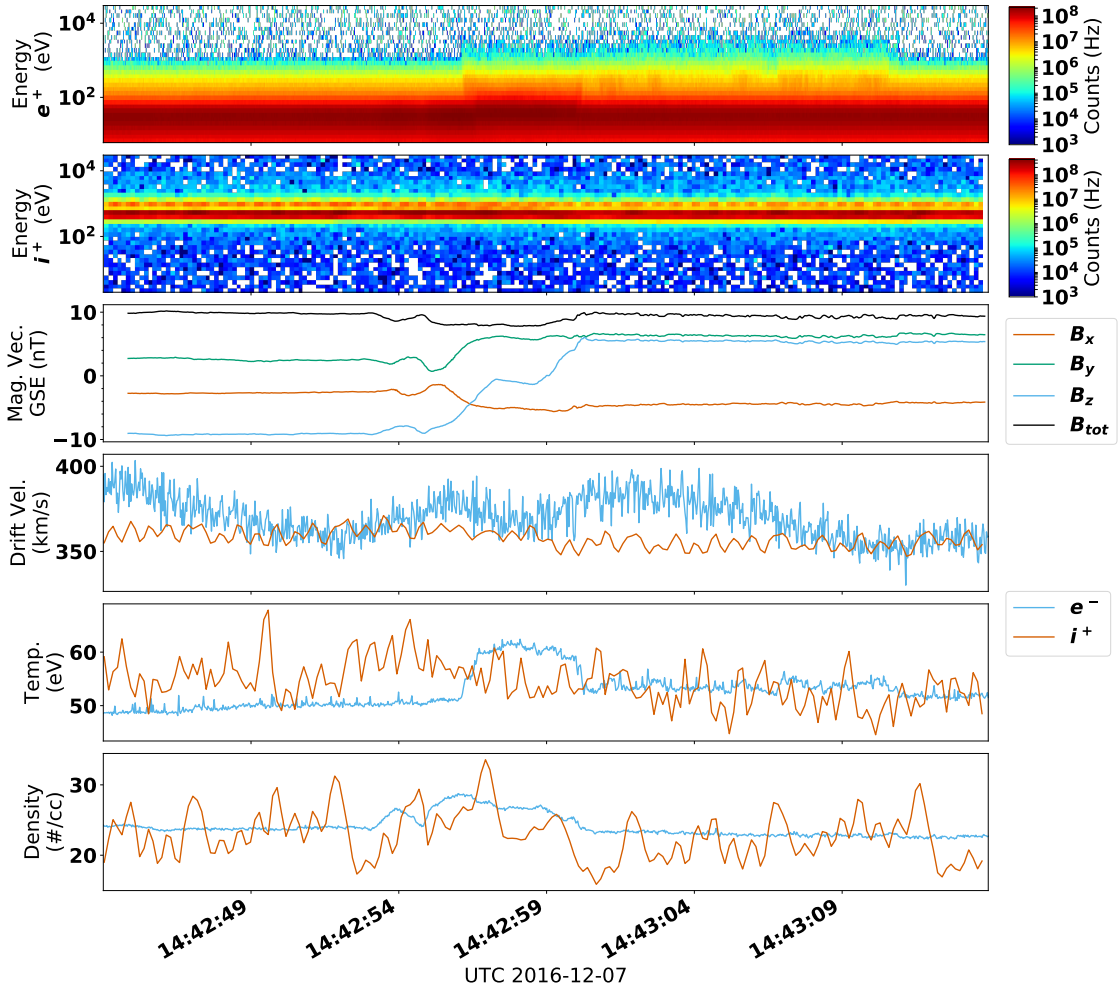

Figure 3.17: Plasma moments calculated for a typical solar wind interval from December 7, 2016, ([62.7k, 36.5k, 7.4k] km GSE). A field reversal in B_Z is present at 14:42:57. Marked by SITL as possible reconnection site.

November 8, 2017. The B_Z reversal and fluctuations in B_{tot} were flagged by the SITL as signatures consistent with a flux rope. The compression performance of this interval is shown in Figure 3.20. In this case the electron compression improves slightly during the magnetic field reduction. The electron compression performance is also helped by the temporary decrease in density immediately following the shift in magnetic field. The ion compression performance, however, is largely driven by the density and not strongly affected by the magnetic field. These both make sense as the electrons tend to be more tightly magnetized than the ions. The ions in this interval have a higher temperature than the electrons; Figure 3.1 illustrates that the effect of density is greater at higher

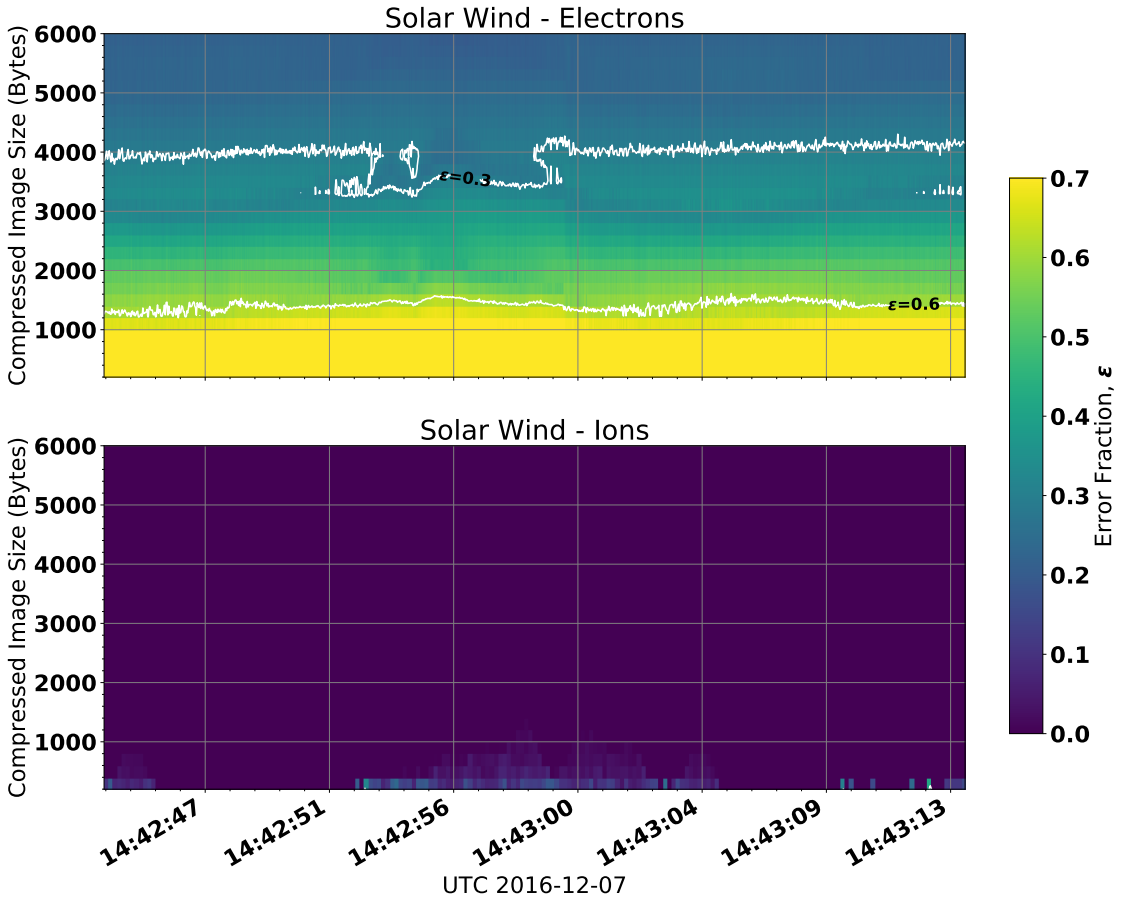

Figure 3.18: Compression performance on typical solar wind data from December 7, 2016 for electrons (top) and ions (bottom). White traces indicate lines of constant error at $\varepsilon = 0.3$ and $\varepsilon = 0.6$. Error is calculated as in Equation 3.2. Note that for ions (bottom) the error does not reach 0.3, therefore white traces are not visible.

temperatures.

Tail - Central Current Sheet Figure 3.21 shows a crossing of the central current sheet in the tail from July 6, 2017. The compression performance of this interval is shown in Figure 3.22. Both the electrons and ions show an elevated error in the vicinity of the higher density current sheet crossing with relatively lower area in the surrounding sheath data. This illustrates that regions are not monolithic - a significant amount of variability is seen in the electron data on either side of the current sheet crossing.

Inner Magnetosphere Figure 3.23 shows a region of the inner magnetosphere from De-

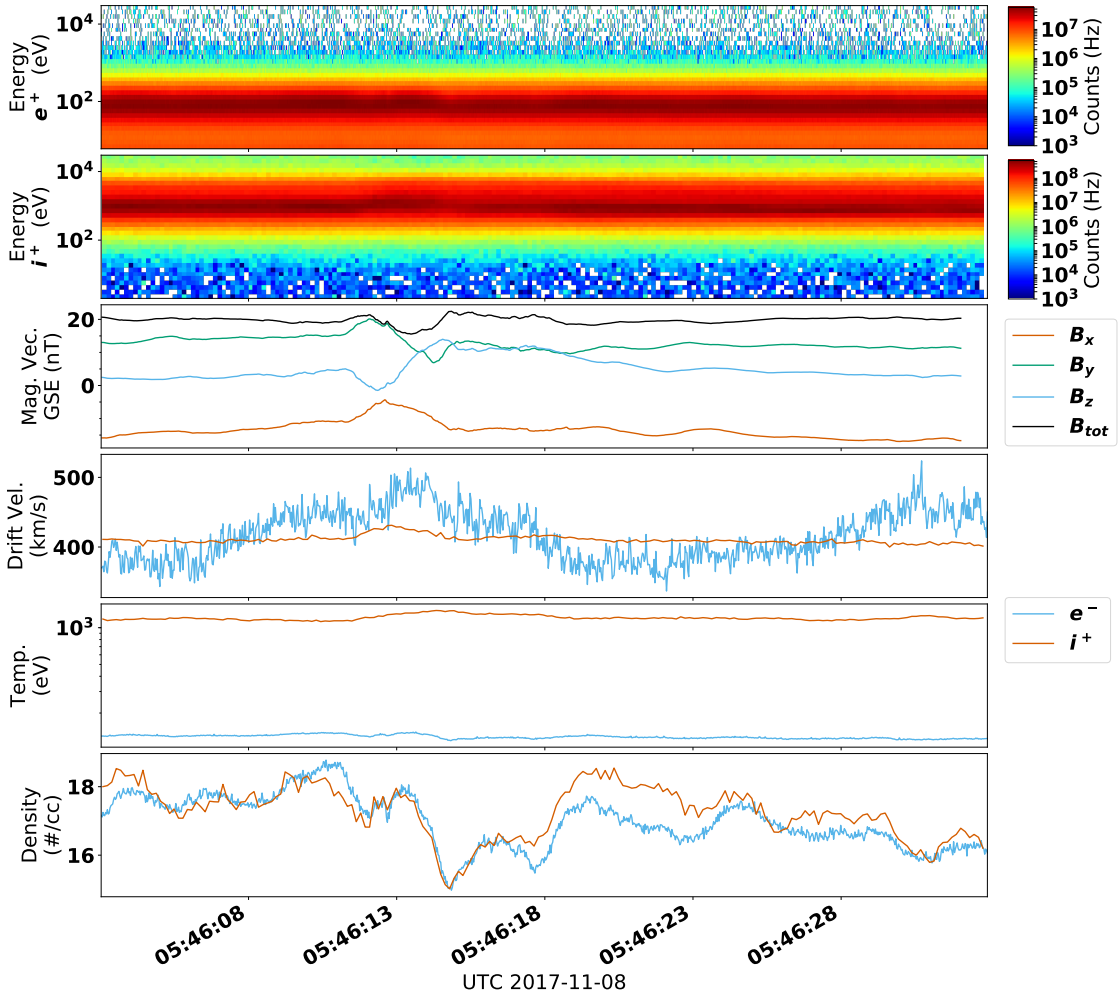

Figure 3.19: Plasma moments calculated for a magnetosheath interval from November 8, 2017, ([13.2k, 106.6k, 13.2k] km GSE). Marked by SITL as possibly containing a magnetic flux rope.

cember 30, 2016, which was annotated as containing a possible flux transfer event (FTE.) The compression performance in the electrons (Fig. 3.24) improves quickly as the density drops at the start of the interval, with a noticeable, but smaller effect in the ions. Noteworthy in this case is that while the FTE appears significant in the energy time spectrograms, it appears to have a comparatively smaller effect on the compression performance. The image size where the error first appears is $\sim$ in line with the lossless transition size shown in Figure 3.1 for similar density and temperature. While the ions compress well and show no significant error until the image size is reduced below 1000 bytes, it is noteworthy that once the image becomes lossy the error escalates

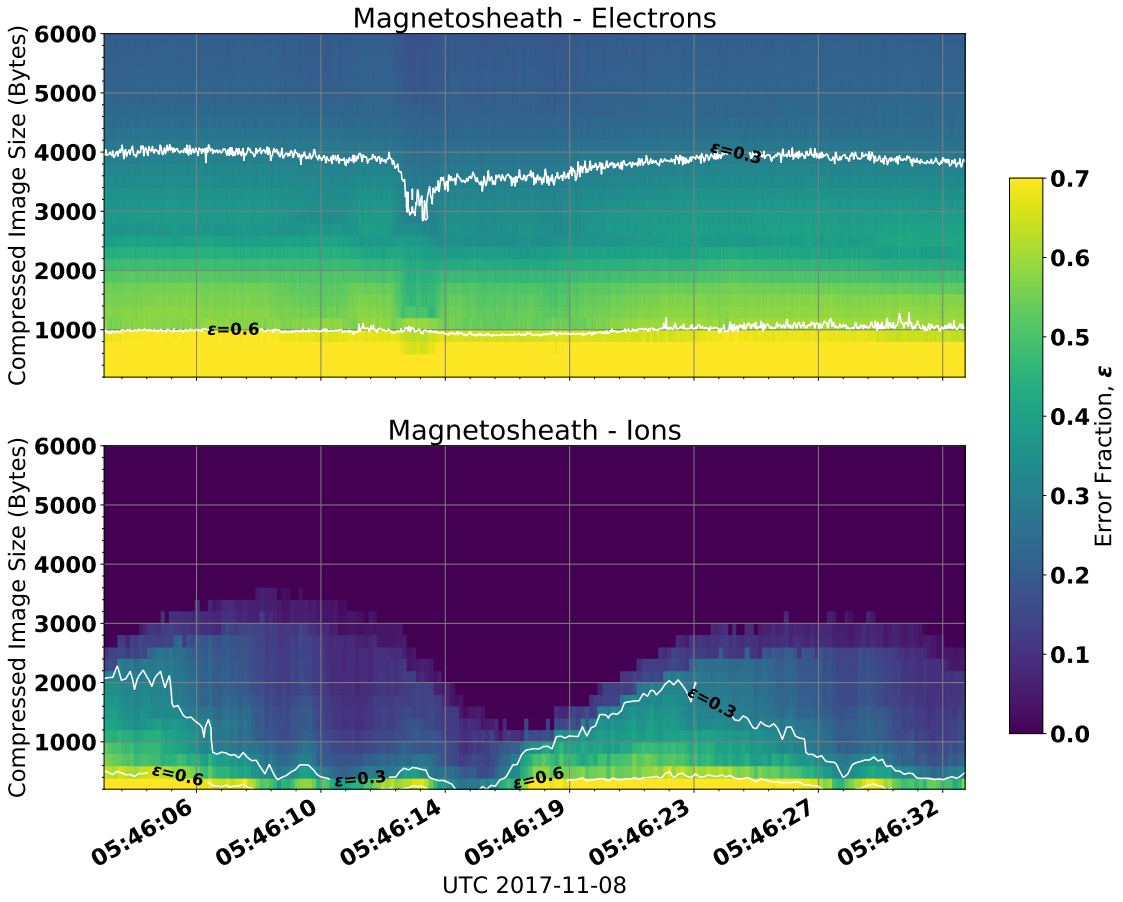

Figure 3.20: Compression performance on magnetosheath data from November 8, 2017 for electrons (top) and ions (bottom). White traces indicate lines of constant error at $\varepsilon = 0.3$ and $\varepsilon = 0.6$. Error is calculated as in Equation 3.2.

quickly. This illustrates that when the wavelet series is short, each wavelet carries a larger fraction of the information.

Lobe / Plasmasheet Boundary Layer Figure 3.25 shows the plasmasheet boundary layer and lobe as recorded on August 7, 2017. Figure 3.26 illustrates that, as with many of the previous cases, the ions compress much better than the ions. Several vertical blue stripes in the electron data shows that even small changes in plasma can significantly alter the compression performance. While the moments are fairly consistent during the first half of the interval, some variation is seen in the spectrogram. Around the mid point, the density rises slightly and the ion temperature jumps leading to some compression error being present in the ion data for the lowest

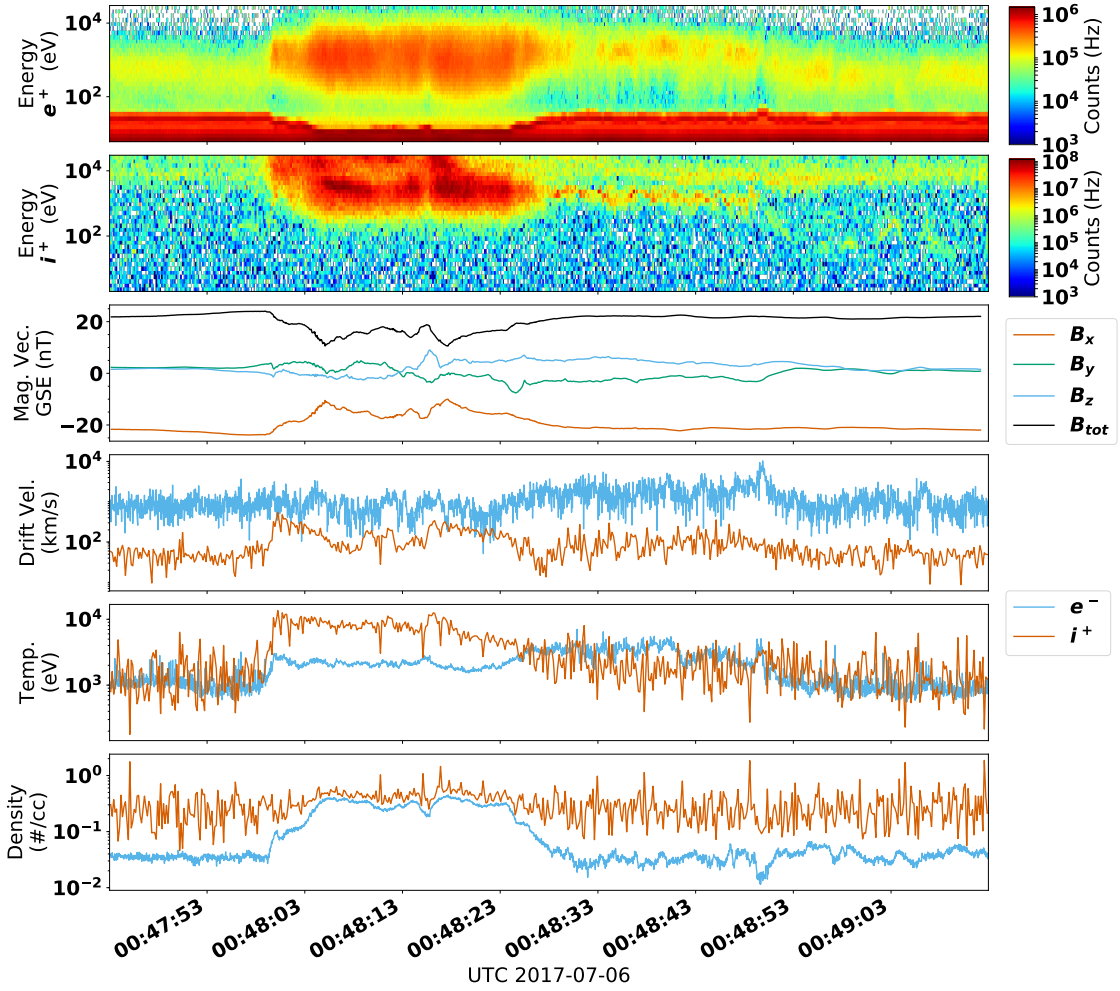

Figure 3.21: Plasma moments calculated for an interval from July 6, 2017, ([-112.1k, 24.5k, 13.8k] km GSE). Marked by SITL as current sheet crossing in the magnetotail.

image sizes.

3.4 Conclusion

The FPI suite onboard the MMS spacecraft have measured plasma distributions a factor of 100 times faster than previous missions. This time cadence required a method of data compression that could be tuned to higher compression ratios than previous missions. Enough data has now been acquired to characterize the performance of the DWT/BPE based compression for plasma count skymap images. The results show that in many regions of the magnetosphere, the images

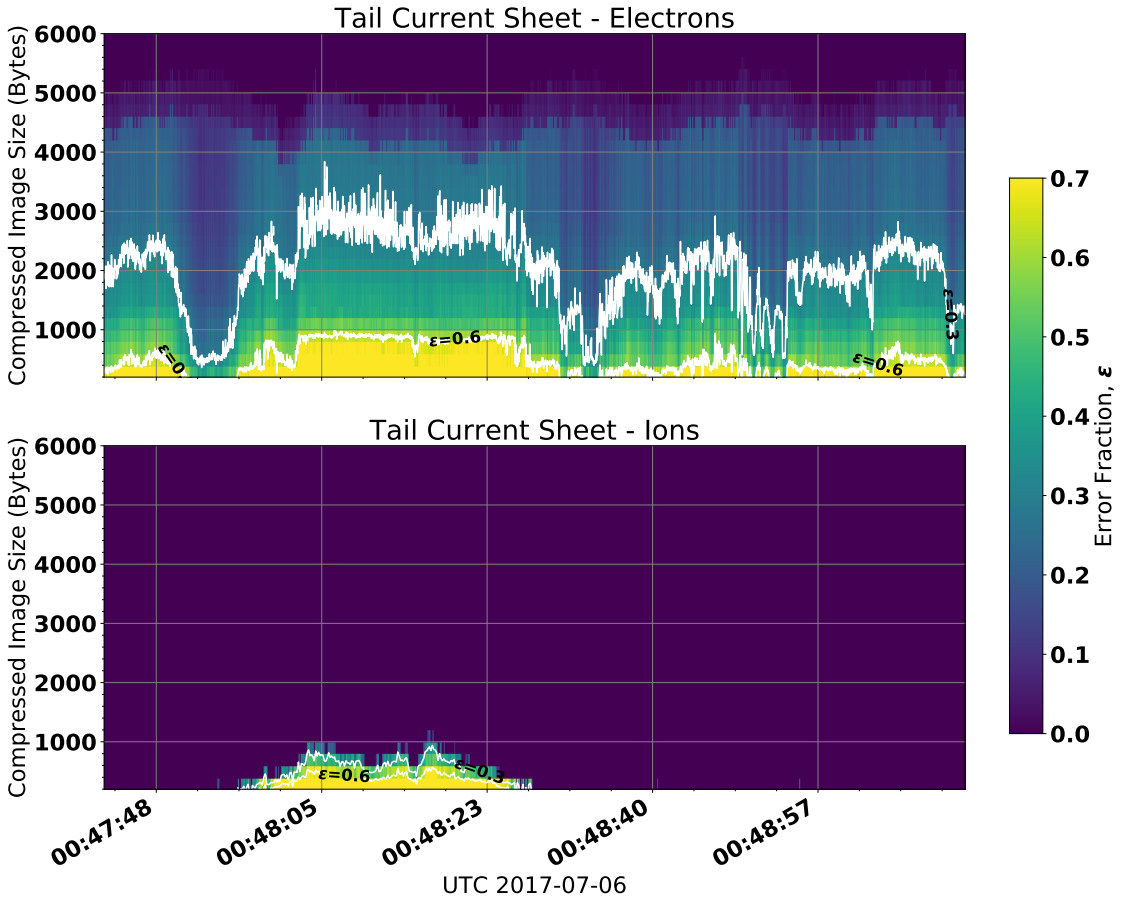

Figure 3.22: Compression performance on tail data from July 6, 2017 for electrons (top) and ions (bottom). White traces indicate lines of constant error at $\varepsilon = 0.3$ and $\varepsilon = 0.6$. Error is calculated as in Equation 3.2.

can be compressed significantly in a lossless manner. The error in the compressed image tends to rise with increased density (count rate) and temperature and tends to lower with more narrowly focused angular distributions. These points tend to allow some plasma regimes to compress better than others, and more starkly, for ions to compress significantly better than electrons in almost all cases.

As increased compression introduces larger losses in the wavelet series, the error tends to manifest in distinct, predictable ways. Some of these are subtle and largely benign, while others fundamentally alter the description of the plasma. These error modes were explored in detail, with typical regions of the magnetosphere annotated for how much the data can be compressed before

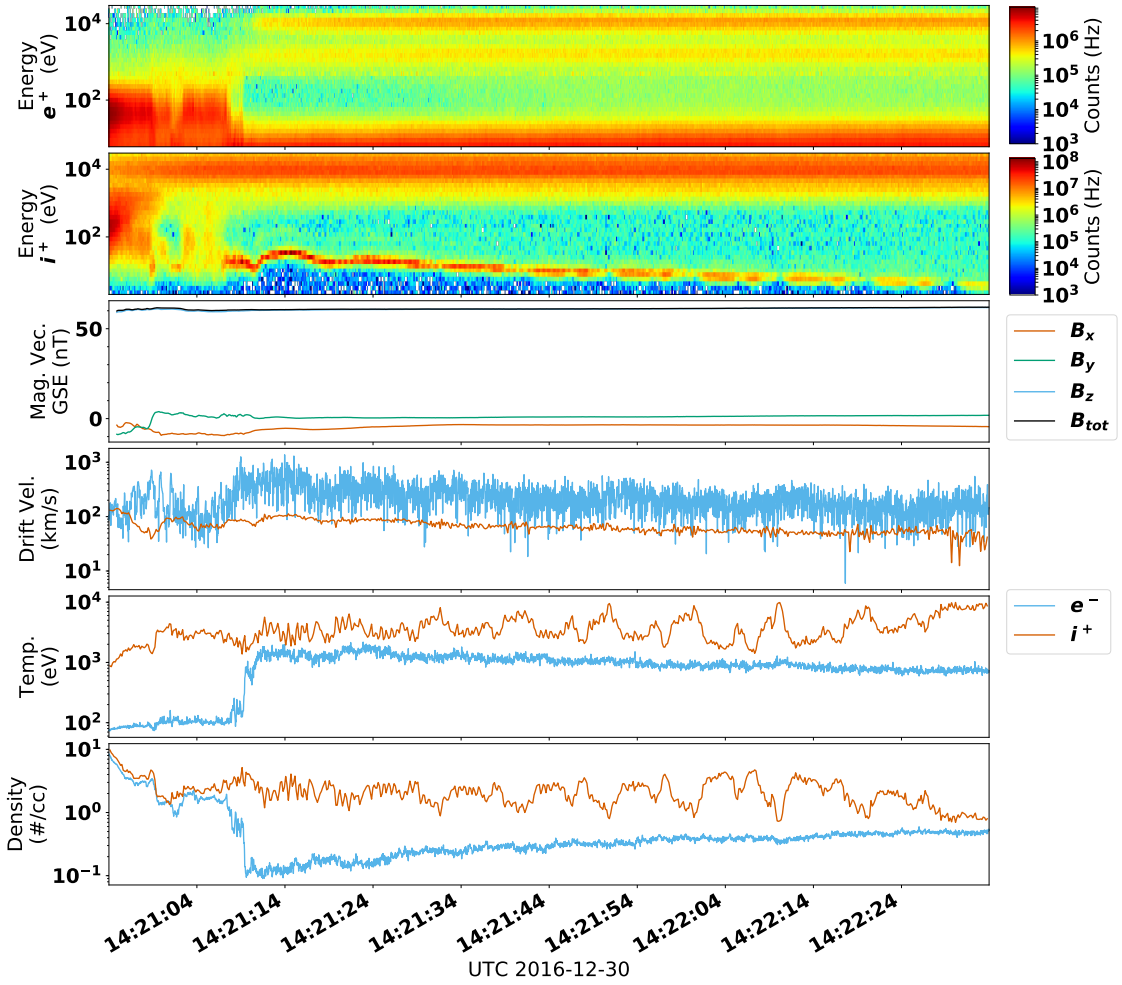

Figure 3.23: Plasma moments calculated for an interval from December 30, 2016, ([62.3k, 17.2k, 10.8k] km GSE). Marked by SITL as possible flux transfer event in the inner magnetosphere.

given error thresholds are crossed.

FPI used integer mode compression and a size limit that yielded lossless compression in the vast majority of images. This work shows that it is possible, however, to drive the compression further if a small amount of error is tolerable using the floating point mode, which will fill all available data volume but with lower error[65]. Electron data can be compressed significantly smaller than the FPI limits while maintaining the large structures in the image. If small errors are allowed to be introduced ($\varepsilon < 0.3$ as defined in Equation 3.2), electron data can, in many cases, be compressed about three times smaller than the FPI limit. Ion data is even more stark, with a large

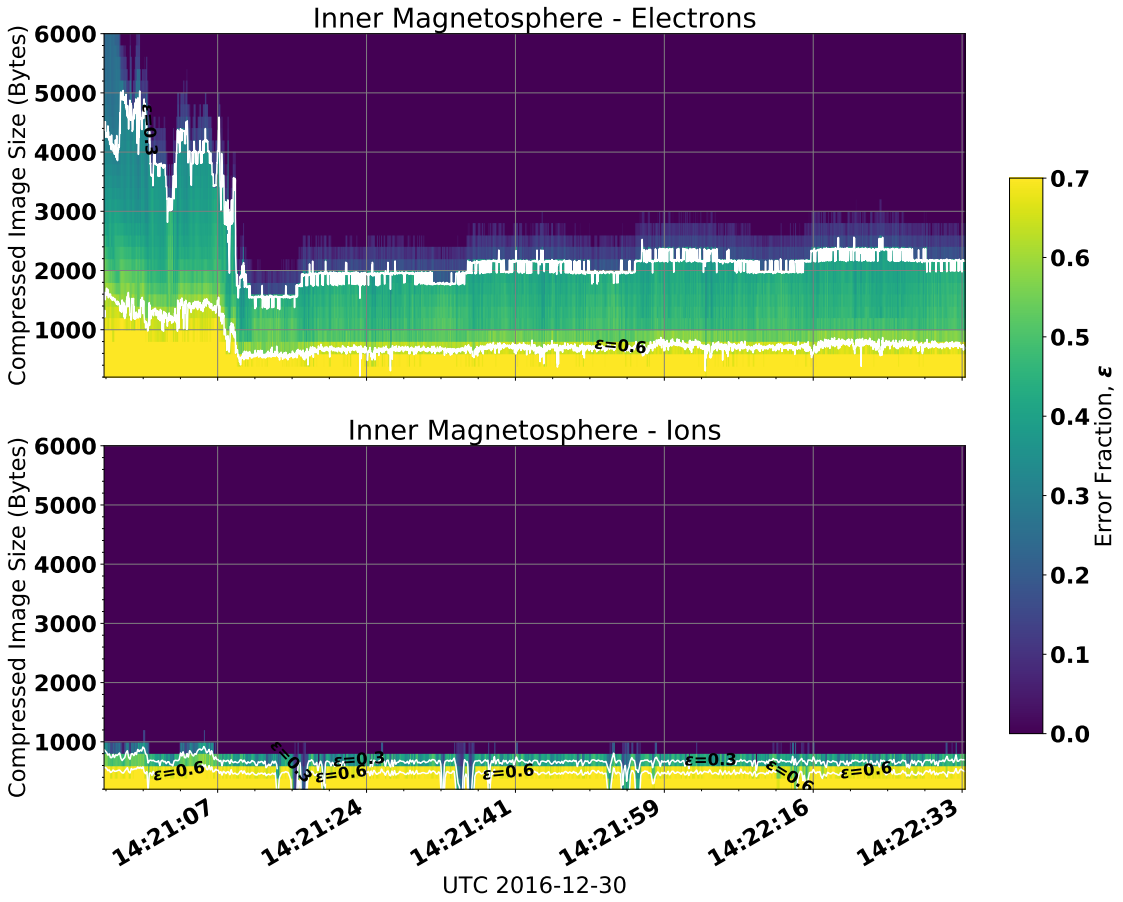

Figure 3.24: Compression performance on inner magnetosphere data from December 30, 2016 for electrons (top) and ions (bottom). White traces indicate lines of constant error at $\varepsilon = 0.3$ and $\varepsilon = 0.6$. Error is calculated as in Equation 3.2.

percentage of data maintaining the low level of error upwards of ten times below the FPI limit. As the FPI data is already compressed, note that this 10x increase from FPI would represent an overall compression ratio of $\sim$ 50:1 of the raw image data. This would represent a huge increase in available data downlink volume for future missions.

FPI assumed a similar performance of the two species, however this should not be the default assumption for future missions. This difference is of particular note in the solar wind, which is highly collimated for ions but not for electrons. The solar wind represented one of the worst regions for electron performance and best regions for ion performance. Many of the ion maps still had no error even at the lowest tested compression size of 200 bytes. This represented a compression ratio of

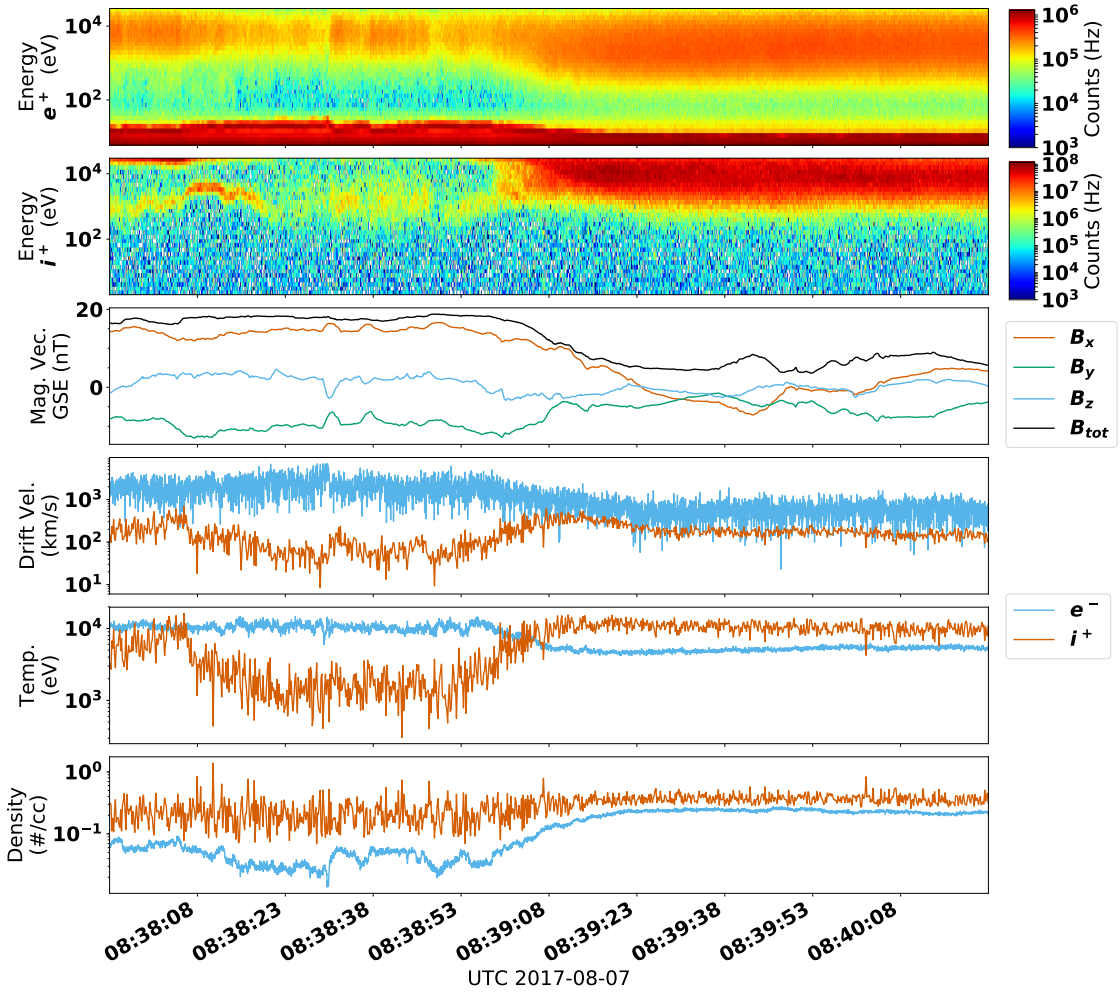

Figure 3.25: Plasma moments calculated for an interval from August 7, 2017, ([-128.2k, 37.7k, 37.0k] km GSE). Marked by SITL as lobe and PSBL.

164:1. By contrast, the electrons approach the artifact level[6] of error ($\varepsilon = 0.3$) even at the highest tested size of 6000 bytes. This illustrates the notion that compression is not one size fits all and that special care must be paid to the operational regimes of the instrumentation when designing a compression system.

A set of recommendations/guidelines for future missions regarding wavelet compression:

- Compression ratios upwards of 10:1 should be possible in most regions of the magnetosphere maintaining an error threshold below that of Poisson statistical noise.
- Higher compression ratios are possible as density and temperature are reduced.

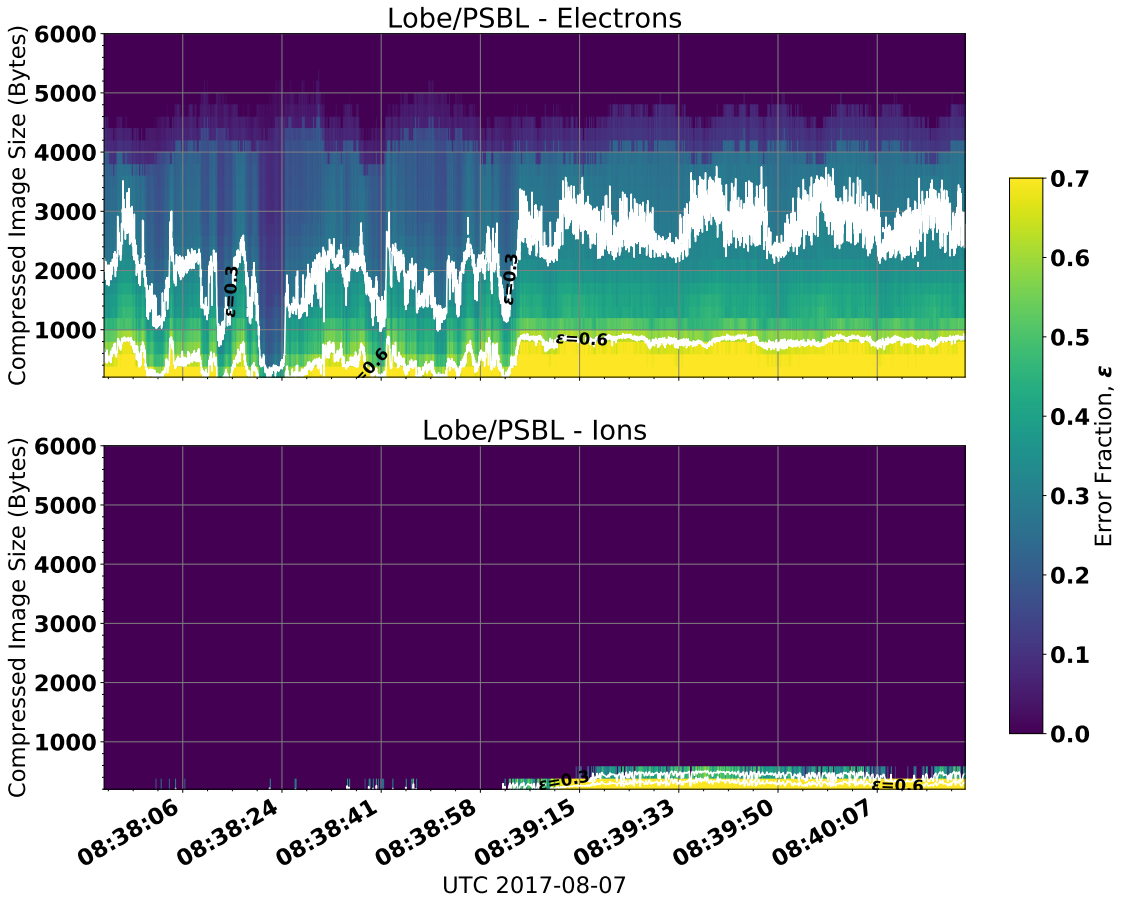

Figure 3.26: Compression performance on lobe / PSBL data from August 7, 2017 for electrons (top) and ions (bottom). White traces indicate lines of constant error at $\varepsilon = 0.3$ and $\varepsilon = 0.6$. Error is calculated as in Equation 3.2.

- Ion data typically compresses to a smaller size than electrons, or alternatively, lower error for a fixed size.

- A minimum size for compressed ion images, or others of sparse data, is recommended due to the quickly increasing error shown in Figures 3.24 and 3.26. A size of 1000 bytes would be recommended based on the data set used here, however this value should be evaluated individually based on the design of future instrumentation.

- Evaluate species separately as ions and electrons will have different compression characteristics.

Chapter 4

Development and Validation of Science Quality Pseudo Moments

Portions of this chapter are taken from:

AC Barrie, D da Silva, S Elkington, Z Sternovsky, AC Rager, DJ Gershman, WR Paterson, JC Dorelli, and B Giles. Physically accurate large dynamic range pseudo-moments for the mms fast plasma investigation. **Earth and Space Science**, 2018

4.1 Introduction

A full-sky image for FPI is performed in 30 ms for electrons and 150 ms for ions for the highest, *burst* resolution data. Only a small fraction ($\approx 5\%$) of this burst resolution data can be down-linked due to telemetry limitations. A longer time resolution (4.5 s) *fast survey* data product is available for the entire science region of interest (roughly 1/2 of the orbit). Not only is the fast survey data at a significantly slower sampling rate, it is also subjected to an increased compression ratio and associated error[6].

Embedded in the 4.5 s fast survey data packet is a set of *trigger terms*, taken at the full burst time resolution. These trigger terms were initially designed as a mechanism to identify large gradients and variances in the data in an effort to mark areas of high scientific interest for priority download. When properly tuned and corrected, however, these trigger terms represent *pseudo plasma moments*, accurate to within a few percent of the fully corrected, burst resolution plasma moments, allowing for a wealth of additional high time resolution science investigations. The processes by which the trigger system calculates the on board terms, and how they are corrected

on the ground, are presented in this chapter.

Previous instrument suites such as AMPTE/IRM[45], THEMIS/ESA[40], WIND[35], and CLUSTER/PEACE[21] have computed on board plasma moments, however the accuracy has generally not been to the level of the ground processed moments. This is largely due to two effects:

(1) The dynamic range of the plasma moments can vary over $\sim$ seven decades[21, 46]. It is difficult for an onboard computational process to accurately resolve this large of a dynamic range, particularly for instruments, such as FPI, that do not have a processor[52].

(2) Environmental and spacecraft effects such as spacecraft potential, a truncated energy range, photoelectrons, etc. are corrected for on the ground but often cannot be corrected for onboard moments[24, 21, 25, 29].

Two new techniques have been incorporated into the FPI scheme and are presented here: tuning the dynamic range of the system to the local environment, and using a neural network to correct for systematic external effects. The tuning of the system allows the dynamic range to be focused on a specific region, which can be adjusted as the spacecraft enters new regimes. This leads to higher resolution, lower error calculations centered on the area of interest. The neural network is designed to correlate several inputs simultaneously, allowing for corrections based on all available inputs. This helps to alleviate external effects such as those mentioned above.

One important distinction between FPI and previous missions is that FPI is not spin integrated. Simultaneous measurements are taken from eight spectrometers through four electrostatic deflection states to form a complete sky image for a given energy shell. Each individual spectrometer has slightly different performance characteristics and ground correction factors for science data. A correction table on the ground can be used to flat-field data from all spectrometers together, however, for the trigger quantities, values are integrated over all spectrometers on board making individual, per spectrometer tuning impossible. A statistical approach was therefore taken for correcting the trigger quantities to produce pseudo plasma moments.

4.2 Ground Based Moment Calculations

Burst resolution data come to the ground in the form of a 32 energy × 16 elevation × 32 azimuth array of counts, C. The raw counts are then converted to a set of plasma moments through a multistep process described below. Moments calculations are performed over velocity space. The FPI spectrometers filter based on energy, which is then used in conjunction with an assumed mass (proton mass for ions) and look angle to acquire velocity, $\vec{v}$. The final released moments are referred to as Level 2 (L2) data[52].

4.2.1 Data Manipulation

The raw count data undergoes a series of transformations and corrections before final moment integrations are performed. The general outline of steps progresses as:

(1) Decompress the raw data

The DES or DIS raw counts array, $\mathrm{C}_{des/dis}$, is made up of 32 energies, 16 zenith look directions, and 32 azimuth deflection pair look directions. These *skymaps* are compressed on board using a discrete wavelet transform and bit plane encoder[6]. Decompression is performed during ground processing into a three dimensional counts array,

$$\mathrm{C}_{des/dis} = \mathrm{array}\{32 \times 16 \times 32\}. \tag{4.1}$$

(2) Apply the deadtime correction

A correction is applied to the counts array to account for the fact that the detection system cannot count infinitely fast, and requires some time to recover between counting events. For FPI, this is primarily driven by the Amptek A121 preamplifier[2]. The DES/DIS deadtime corrected counts array, $\mathrm{D}_{des/dis}$, is constructed using:

$$\mathrm{D}_{des/dis} = \frac{\mathrm{C}_{des/dis}}{1.0 - \tau_{des/dis} \times \mathrm{C}_{des/dis}}, \tag{4.2}$$

where $\tau_{des/dis}$ is defined by:

$$\tau_{des} = \frac{\tau_{eff}}{195 \times 10^{-6}}, \quad \tau_{dis} = \frac{\tau_{eff}}{1.0 \times 10^{-3}}, \tag{4.3}$$

where 195×10^{-6} and 1.0×10^{-3} represent the integration times for DES and DIS for an individual angle/energy bin, in seconds. τ_{eff} represents the detection system deadtime (minimum time between count pulses) in seconds, and is defined as follows:

$$\tau_{eff} = 100 \times 10^{-9}. \tag{4.4}$$

(3) Construct the phase space density

Using the $D_{des/dis}$ counts array (32 azimuth, 16 polar, 32 energy), the energy and angle targets, and the f_1 *counts correction table*[25], construct the 3 dimensional phase space density f,

$$f = f(\vec{v}) = f_1 D_{des/dis} = \text{array}\{32 \times 16 \times 32\}. \tag{4.5}$$

(4) Despin the phase space density

Data are converted to a non-spinning reference frame, accounting for the effects of a rectilinear mapping of a spherical measurement space.[54]

(5) Apply a photoelectron correction

Photoelectrons are removed from the electron data as described by Gershman et. al.[24]. This correction is composed of two components: internal photoelectrons generated by direct sunlight in the instrument aperture (several energy bins, localized in azimuth), and low energy electrons generated on the spacecraft surface and detected by FPI (fewer energy bins, across all azimuth angles.) Both components are well characterized with both lab and flight data and can be subtracted.

(6) Correct the energies by the spacecraft potential, provided by the Electric Double Probes (EDP)[61]

The reported FPI energies are energy set points and do not include the effects of spacecraft potential which are obtained separately from EDP. Energies of measured particles are adjusted by the measured spacecraft potential (simple addition/subtraction) to account for acceleration through the spacecraft sheath. Note that while energies are corrected for sheath effects, directions cannot be recovered, and thus some sheath induced error will remain in calculations, particularly at low energies.

(7) Rescale energy

Energies are rescaled from the measurement energy range, E, to a new range, U following $U = E/(E + E_0)$ where E_0 is a constant (set to 100eV for FPI). This maps $U(E \to 0) = 0$ and $U(E \to \infty) = 1$. Velocity integrands are modified accordingly.

(8) Extrapolate to full angle and energy range for integration

(a) $f(\phi = 0)$ is repeated as $f(\phi = 360°)$ to ensure that the periodic boundary condition is incorporated to the azimuthal integration.

(b) $f(\theta = 0) = 0$ and $f(\theta = 180°) = 0$ data points are added to ensure the polar integration goes from 0 to 180 degrees. The $\sin(\theta)$ dependence of the polar integration forces the integrand at $\theta = 0$ and $\theta = 180$ to zero regardless of the value of the phase space density

(c) $f(U = 0) = 0$ and $f(U = 1) = 0$ data points are added to ensure the integration goes from $E \to 0$ to $E \to \infty$. $U = 0$ forces the integrand equal to zero regardless of the phase space density.

4.2.2 Calculate the Plasma Moments

The plasma moments that are correlated to trigger based pseudo-moments are described here (see [25] for a complete set of moments.) In general, plasma moments define the bulk behavior of a plasma: density, temperature, etc[32]. These are calculated using the phase space density, $f(\vec{v})$.

FPI uses a trapezoidal integration scheme for its calculation of plasma moments. First, phase space density skymaps are integrated with respect to spacecraft azimuth angle, (i.e., 32, 11.25° bins with centers 0-348.75°). Next, skymaps are integrated with respect to spacecraft polar angle, (i.e., 16, 11.25° bins from 5.625 to 174.375°). Finally skymaps are integrated with respect to energy, E, (i.e., 32 bins from ≈ 10 eV to 30 keV).

$$\text{Number density, } \#/cm^3,\ n = \int f(\vec{v}) d^3v \tag{4.6}$$

$$\text{Flux, } \#/s/cm^2,\ \vec{F} = \int n\vec{v} \tag{4.7}$$

$$\text{Magnetic parallel flux, } \#/s/cm^2,\ F_B = \int n\vec{v} \cdot \hat{B} \tag{4.8}$$

$$\text{Pressure tensor, nPa, } \overline{P} = m \int (\vec{v} - \vec{v}_d)(\vec{v} - \vec{v}_d) f(\vec{v}) d^3v \tag{4.9}$$

$$\text{Kinetic temperature, eV, } T = \frac{\text{Tr}[\overline{P}]}{3n} \tag{4.10}$$

where $\vec{v}_d$ is the drift velocity, m is the particle mass, and $\hat{B}$ is the unit magnetic field unit vector.

4.3 Pseudo Moment Calculations

A full complement of standard plasma moments are available for FPI burst data[52]. These are processed and corrected on the ground for all downlinked data. In addition, the FPI suite calculates a set of on board *trigger terms* for each burst skymap - every 30 ms for electrons and 150 ms for ions. While the trigger terms are proportional to physical quantities there are several key differences between these and the full moments derived from burst data:

(1) There is no term for ion pressure term, which also precludes an ion temperature calculation

(2) Trigger integrals are performed on raw counts and are missing several corrections, discussed in [25, 54], that occur during ground moment calculations:

   (a) Correcting for deadtime

(b) Removal of secondaries and photoelectrons

(c) Adjusting energies for spacecraft potential

(d) Correcting for relative efficiency between spectrometers

(e) Extrapolating to a full angle and energy range

(3) All trigger terms are unsigned, which impacts the onboard flux integrals and products derived from them

(4) A magnetic field is acquired onboard from the FIELDS suite at a rate of 8 Hz; this is also uncorrected, and at a significantly reduced time resolution than is available on the ground

These trigger terms are corrected on the ground into a set of *pseudo moments*, which are physically meaningful and approach the accuracy of the fully corrected plasma moments.

4.3.1 On Board Trigger Term Calculations

The formulation of each of the four electron and three ion trigger term quantities are shown here. In these formulations, ε represents the bin for a given energy, E, and $\hat{b}$ is the magnetic field vector. θ and ϕ are look angles, used to inform the look direction, $\hat{r}$, consisting of x, y, z components in the spacecraft reference frame. S represents a pruning table that is used to remove a subset of values near the poles to prevent oversampling[52]. C_e and C_i represent the raw count matrix for electrons or ions.

$$\text{Electron Pseudo Density, } D_e = \sum_{\varepsilon=E_0}^{E_{31}} \frac{1}{\sqrt{\varepsilon}} \sum_{\theta=0}^{15} \sum_{\phi=0}^{31} S\left(\theta,\phi\right) C_e\left(\varepsilon,\theta,\phi\right) \tag{4.11}$$

$$\text{Electron Pseudo Pressure, } P_e = \sum_{\varepsilon=E_0}^{E_{31}} \sqrt{\varepsilon} \sum_{\theta=0}^{15} \sum_{\phi=0}^{31} S\left(\theta,\phi\right) C_e\left(\varepsilon,\theta,\phi\right) \tag{4.12}$$

$$\text{Electron Pseudo Mag Parallel Flux, } F_{eB} = \left| \sum_{\varepsilon=E_0}^{E_{31}} \sum_{\theta=0}^{15} \sum_{\phi=0}^{31} S\left(\theta,\phi\right) \hat{b} \cdot \hat{r}\left(\theta,\phi\right) C_e\left(\varepsilon,\theta,\phi\right) \right| \tag{4.13}$$

$$\text{Ion Pseudo Density, } D_i = \sum_{\varepsilon=E_0}^{E_{31}} \frac{1}{\sqrt{\varepsilon}} \sum_{\theta=0}^{15} \sum_{\phi=0}^{31} S(\theta,\phi)\, C_i(\varepsilon,\theta,\phi) \tag{4.14}$$

$$\text{Ion Pseudo X Flux, } F_{ix} = \left| \sum_{\varepsilon=E_0}^{E_{31}} \sum_{\theta=0}^{15} \sum_{\phi=0}^{31} S(\theta,\phi)\, r_x(\theta,\phi)\, C_i(\varepsilon,\theta,\phi) \right| \tag{4.15}$$

$$\text{Ion Pseudo Y Flux, } F_{iy} = \left| \sum_{\varepsilon=E_0}^{E_{31}} \sum_{\theta=0}^{15} \sum_{\phi=0}^{31} S(\theta,\phi)\, r_y(\theta,\phi)\, C_i(\varepsilon,\theta,\phi) \right| \tag{4.16}$$

$$\text{Ion Pseudo Z Flux, } F_{iz} = \left| \sum_{\varepsilon=E_0}^{E_{31}} \sum_{\theta=0}^{15} \sum_{\phi=0}^{31} S(\theta,\phi)\, r_z(\theta,\phi)\, C_i(\varepsilon,\theta,\phi) \right| \tag{4.17}$$

The conversion of counts to phase space density includes a v^{-4} factor, where v is the speed of the particle at a given energy. Integration of phase space density over a spherical grid to find number density requires an additional factor of $v^2 dv$. Therefore, scaling counts by $1/\sqrt{\varepsilon}$ and summing provides a quantity that is proportional to a number density integral. For the pressure term, counts are scaled by $\sqrt{\varepsilon}$ to correlate with nT.

Electron temperature pseudo moments are calculated as a derived parameter: $T_e = P_e/n_e$. Similarly, velocity moments are obtained by dividing fluxes by density. Ion pressure is not available as a trigger quantity, so ion temperature is not included in the final distribution.

4.3.2 FPGA Implementation

The summations in Equations 4.11 - 4.17 are executed by a Field Programmable Gate Array (FPGA) inside the IDPU. Onboard summations, such as these, are not new and are similar to those as far back as AMPTE/IRM (See Table 6.1 in[45]). Because the trigger terms must be small in data volume, yet still cover a large dynamic range, however, a new system has been developed for FPI that allows for the dynamic range to be tuned to a specific plasma regime or environment. This is accomplished by scaling the data to a specific range at two intermediate points during the summations. The scaling process allows for the full system range to be utilized, regardless of the physical dynamic range. This allows a small register to cover an arbitrarily wide dynamic range.

This process can therefore mimic the behavior and accuracy of a double precision floating point calculation while still using a fixed point (FPGA) architecture. The two angular summations are performed and intermediately stored in a 32 bit register during summing. The completed sum over angle is shifted by an arbitrary number of bits, known as a *scale factor* and is then truncated to a 16 bit register. This angular summing is referred to as the *inner loop*. A second sum, over energy, is also internally stored in a 32 bit register before again being shifted by a second *scale factor* and stored in a 16 bit register. This is the *outer loop*. After completion of the summation a logarithmically spaced lookup table (LUT) is used to compress the absolute value of the term into an unsigned 8 bit final quantity in the range of 0-255. This process yields a quantity that is not physical, but scales with the desired plasma moment. Each trigger term is therefore stored in a single byte of data, whereas a complete raw count skymap takes up 20480 or 32768 bytes for electrons and ions respectively.

The 8 bit term values are downlinked to the ground in the Fast Survey science packets. In addition to the 8 bit term products, internal calculations of variances and means of the term quantities over a 10 second interval are also performed and downlinked to the ground in the form of *Trigger Data Numbers* (TDNs)[52]. The 10 second TDN products are computed using 16 bit signed term values (before the LUT compression to 8 bits and loss of sign). Some additional information can therefore be learned from the TDNs, however, they will not be discussed in detail here.

4.3.3 Scale Factor Tuning

As described in Section 4.3.2, each trigger term has two associated scale factors, one for the inner loop (over angles) and one for the outer loop (over energy.) The inner loop scale factor is between 0 and 3. The outer loop scale factor can range between 0 and 15, however, is typically in the range of 8-13. These scale factors are used to tune the trigger calculation to the current region of interest's dynamic range for each term.

There are three major causes of error introduced in the fixed point trigger calculation (relative to the equivalent floating point calculation): saturation of the inner (angle sum) loop, saturation

of the outer (energy sum) loop, and quantization of low values. All three of these error sources are characterizable by the values of the two scaling factors and the term value. Each combination of scale factors will lead to a low error introduced, $\approx 3\%$, for a significant subset of the overall dynamic range. Associated reference curves can then be used to fine tune the scale factors in such a way as to ensure that the entire region of interest lies in this low error regime, keeping the error for all calculations below $\approx 3\%$. The error between the fixed point calculated term, a, and the floating point calculated term b, for a given term on a given skymap is calculated as:

$$error = \frac{|a - b|}{b} \tag{4.18}$$

A data set was created where the value for each moment (density, bulk velocity, temperature), was randomly selected on a log-uniform scale. 2000 random samples were drawn, ranging from Log10(M0) to Log10(M1), where M0 and M1 are the min and max of the moment being sampled. Density ranges from 0.1/cc to 100/cc, bulk velocity components from -1000 km/sec to 1000 km/sec (with a minimum magnitude of 10 km/sec), and temperature from 1 eV to 10 keV. Magnetic field is set to a constant 25 nT with each component having equal magnitude. Each sampling was used to create a burst map, which was added to the data set.

Figure 4.1 shows the results of a trigger term calculation for electron density for this data set. The data set encompasses a dynamic range larger than the system can accurately resolve, and therefore illustrates the available error modes. Quantization, seen on the left side, appears when a large shift on either loop prevents small values, or small deltas, from being accurately resolved. This can be relieved by lowering either scale factor. Inner loop saturation depresses the counting of the inner, angular summing, loop. This can be relieved by raising the inner scale factor. Saturation of the outer loop results in the term value to be pegged at the maximum 255. This can be relieved by raising the outer scale factor. Note that saturation of the inner loop is more harmful than saturation of the outer loop since it is not immediately clear from an individual point that the saturation has occurred; the error is thus unknown. Saturation of the outer loop is easily identified

since it will always be at the maximum value. For this reason, the inner scale factor is generally kept large when high count rates can be expected in a single energy shell.

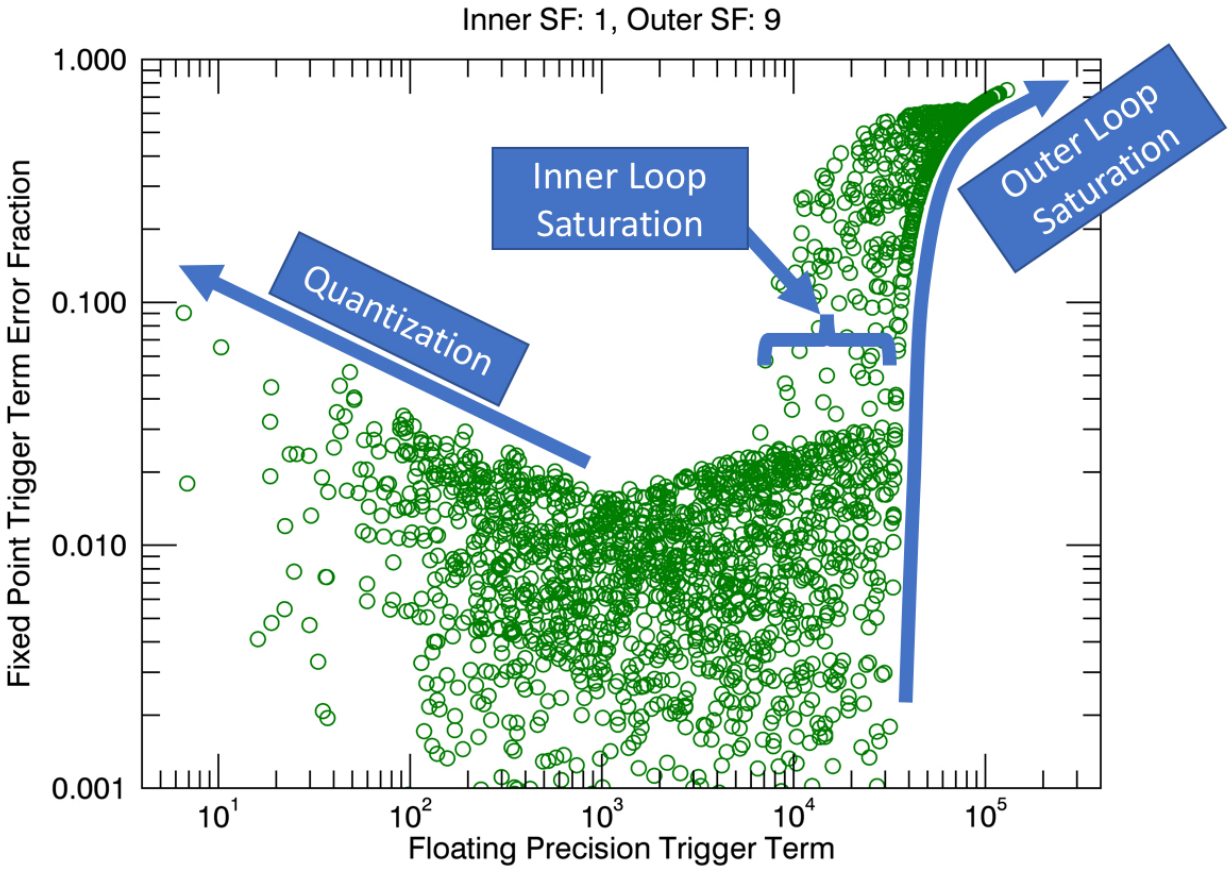

Figure 4.1: Identifying the error modes associated with the FPGA term accumulations: quantization, and saturation of the two summation loops. Data points are of the electron density term, sampled from a simulated data set.

For a given set of scale factors, there exists a range of values that do not experience significant quantization, or saturation of either loop. Scale factors may be chosen such that the majority of data points for a given plasma regime will lie in this region of the curve. For example, Figure 4.2 shows two data sets run through the trigger engine with different sets of scale factors. The same data set from Figure 4.1 has been divided into a subset of sparse magnetosphere ($< 1/cm^3$) in red, and dense magnetosheath ($> 10/cc$) in blue. Three different sets of scale factors are chosen, yielding three different encoding behaviors. The center panel shows that both sets cannot be fully resolved at the same time, however, the left and right panels show that the system can be tuned to

focus on one set or the other, keeping the max error below 3%. The scale factors are parameters to the fast survey science mode command, allowing the scale tuning to be performed regularly. FPI uses three sets of scale factors tuned to three specific regions:

(1) Magnetopause

(2) Solar wind

(3) Tail current sheet

For a given day side orbit, the *magnetopause* set is used from the inner magnetosphere out until beyond the bow shock. The *solar wind* scale factors are then loaded while MMS is in the solar wind, and the *magnetopause* factors are resumed on the inbound leg prior to crossing the bow shock. The *tail current sheet* table is used seasonally when the orbit precesses into the magnetotail. Note that the *solar wind* scale factors were not used during Phase 1[19] of the mission due to a lower apogee.

To arrive at operational scale factors, the simulated data used in Figure 4.2 were used as an initial guess. These scale factors were then refined using flight data from commissioning to arrive at a final set of scale factors shown in Table 4.1. While the scale factors rotate through these sets multiple times per orbit, the three sets of scale factors themselves are not routinely updated. Upon completion of a mission phase, when a new neural network is trained, the scale factors are reevaluated. They are therefore not static, and may be adjusted in the future as the system ages.

4.3.4 Reconstitution of Data on Ground

4.3.4.1 Unpacking Terms

The trigger terms downlinked to the ground are all in the range of 0-255. These are reconstituted into physical pseudo moments on the ground. The terms are first re-scaled to their original magnitudes following the form:

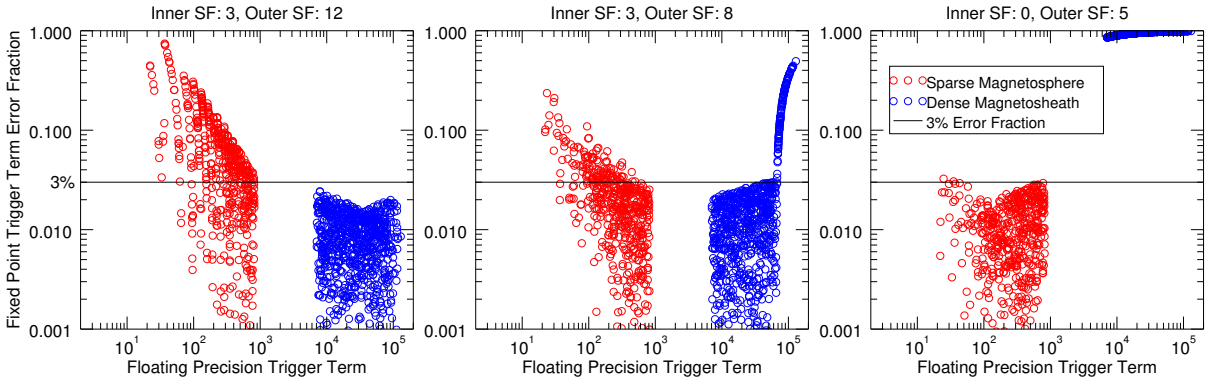

Figure 4.2: Scale factors can be chosen to optimize a certain plasma regime and tuned to either the red or blue regions. The red data points were sampled from a distribution of typical sparse magnetosphere, and the blue from typical dense magnetosheath.

	Magnetopause		Tail Current Sheet		Solar Wind	
Term	Inner SF	Outer SF	Inner SF	Outer SF	Inner SF	Outer SF
Electron Pseudo Density	2	11	0	9	3	11
Electron Pseudo Mag Parallel Flux	0	14	1	7	2	10
Electron Pseudo Pressure	2	12	0	9	2	10
Ion Pseudo Density	1	9	0	5	1	7
Ion Pseudo Flux	2	9	0	5	2	10

Table 4.1: List of currently used scale factors for MMS mission. Note that all three ion fluxes share a common set of scale factors.

$$term = LUT(i) \times 2^{s_i + s_o} \tag{4.19}$$

where i is the downlinked 0-255 term value, $LUT(i)$ is a logarithmically spaced look up table and s_i and s_o are the assigned inner and outer loop scale factors. This process yields a number that is proportional to a physical moment value (density, pressure, flux, etc). Corrections must still be applied, however, to obtain a physically meaningful quantity.

Figure 4.3 shows the raw correlation between the trigger terms and the L2 moments for the Phase 1B day side pass (See Section 2 for a discussion of the MMS phases). These initial correlations show that a linear relationship appears to exist, with an error associated with spacecraft potential. Spacecraft potential was identified as a primary driver of error in the calculation through initial

data analysis and is therefore used as a parameter for data correction. This makes logical sense as a potential sheath around the spacecraft will directly alter particle velocities.

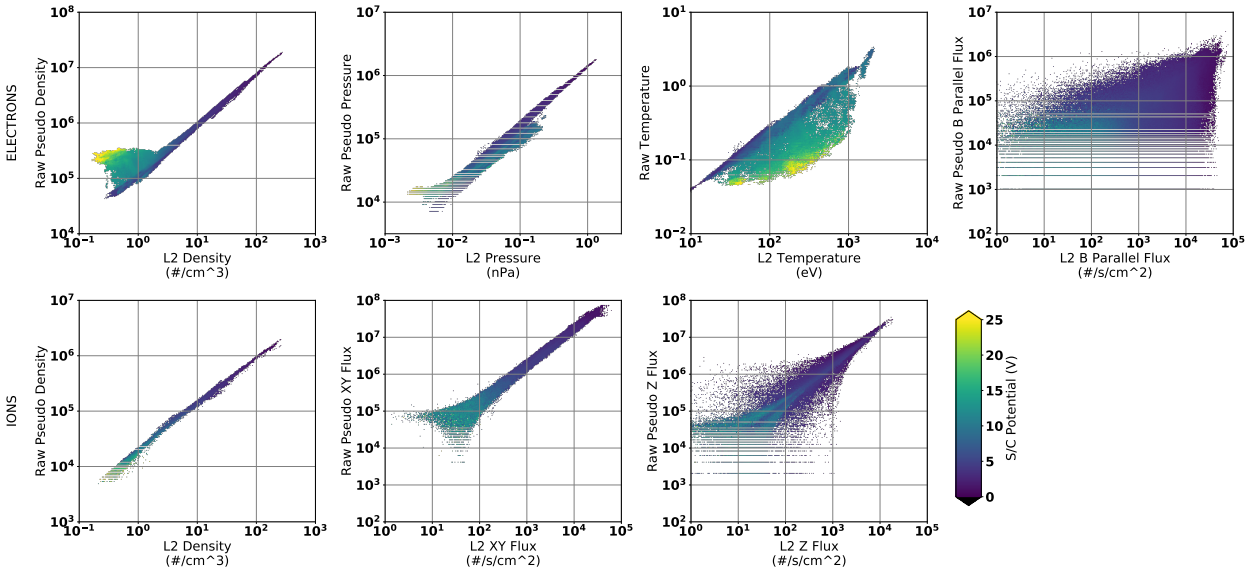

Figure 4.3: Relationship of raw, uncorrected trigger terms to Level 2 (L2) plasma moments; electron data (top row) and ion data (bottom row). Data is taken from MMS Phase 1B day side pass.

The ion flux pseudo moments are expressed as a spacecraft centered Z Flux (spin axes aligned) and an XY Flux (spin plane). Although the raw term values separate X and Y flux, these quantities are unsigned, making a transformation to a non-spinning frame unreliable. These algorithms cannot be modified as the FPGA is non-reprogrammable. A combined value, XY flux in the spin plane, mitigates these concerns.

Ion XY Flux shows evidence of outer loop saturation and cannot resolve the highest flux levels as evidenced by the flat capped value of the raw values. Similarly, many of the terms show signs of quantization at the lowest levels evidenced by quantized horizontal stripes. These effects can be attributed to the scale factors not being ideally selected. It should be noted, however, that all three ion fluxes share a common set of scale factors so it is not possible to tune XY Flux independently of Z Flux.

4.3.4.2 Correction Using Neural Network

The ground correction process was automated using a neural network regression model[55, 48]. The corrections were designed as an independent network for each of the pseudo moments. Each neural network (one per pseudo moment) takes in all terms for a given species (4 electron / 3 ion) plus the spacecraft potential as the input layer (feature vector space.) The central hidden layer optimizes the weighting of 100 linear combinations of the inputs. The optimization is based around the gradient of the error; moving down the gradient to a lower error state, where error is measured relative to the set of provided training data - the burst L2 moments in this case. Linear combinations that do not decrease the overall error are then removed from the optimization via the activation model. The weighting and activation models can then be applied to any set of inputs to convert an unpacked term into a pseudo moment.

The accuracy of the model increases with a greater amount of training data up to the capacity of the architecture. The networks used for correcting FPI pseudo moments are trained on one season (day side / tail pass) of burst moments. The results presented here are using the network trained using Phase 1A data. In each case 90% of the data was randomly sampled as *training* data, and the remaining 10% was segregated as validation, or *test* data. This design was chosen for its ability to efficiently treat the nonlinearities with a relatively low cost for design and implementation. There can be a concern with this approach that the correction model will only be accurate for data that is similar to the training data. Such a model is justified here due to close similarity between the selected burst data and the remaining data that was not downlinked as burst. To ensure that seasonal changes, or aging of the instrumentation, are accounted for, training will be performed independently for each mission phase ($\sim$ 3-6 months) upon completion of the phase.

The networks were structured after the multi-layer perceptron pattern[31, 27] with the following specifications:

- **Loss: squared-error + L2 regularization**. This is a standard squared residual for measuring the error of the linear combination.

- **Layers: 3** . Standard input, hidden (optimization), and output layers are used.
- **Hidden layer size: 100**. 100 different linear combinations are randomly chosen.
- **Activation: max(0, x)**. If a combination increases the error it will be not be included.
- **Optimization: Adam**. Adam stochastic gradient method for optimizing the coefficients[31]. This is a standard method often used in neural networks.

4.3.4.3 Scaling to Survey Data

Fast survey data is available for all science regions, and can therefore be included in the correction. Fast survey data can also be fully corrected up to L2. The final step in the correction process, therefore, is to scale the data segment ($\approx$ 1 min) so that the average of the corrected pseudo moment data matches the average of the fast survey data from the same time period.

4.3.4.4 Correction Quality

The fit quality as a function of likelihood is shown in Figure 4.4. As expected, the relationship between the predicted pseudo moments and L2 moments is highly linear. The density and pressure moments show excellent agreement in almost all cases. Note that there are two small populations in the electron density moment that stray significantly from the x=y unity line. These errors were introduced by the inclusion of fast survey data in the correction algorithm. The fast survey data is not part of the training algorithm, but is used during the correction process to inform the average moment value over the 4.5s integration period. In the majority of cases, this improves the accuracy of the pseudo moment calculation, but in some cases the fast survey product suffers from significant compression error[6]. In these cases, the fast survey average is not representative of the burst data and can actually reduce the accuracy of the pseudo moment. While they are included here for illustrative purposes, in practice, time intervals with increased compression error in the fast survey product will be flagged as likely invalid and the Fast Survey data would not be used to scale those data. Temperature moments also show good agreement, with slightly elevated error owing to error

contributions from both the density and pressure terms. The flux values show good agreement at high flux levels, however, they show a large uncertainty at lower fluxes. The errors in flux tend to be larger because of the inherent uncertainty in direction measurements as well as generally larger error for low count rates:

- FPI has an 11.25 degree angular bandpass[52]
- Angular measurements are affected by the sheath around the spacecraft in a non-systematic way[64]
- Rectilinear mapping of a spherical space causes errors in look angle at high latitudes[54]
- Lower flux levels typically correspond with lower count values and increased statistical noise
- The electron term integrals also include a significant photoelectron population[24], which becomes more significant at low densities

The magnetic parallel electron flux has a larger error than the ion fluxes because of the higher thermal velocity in electrons relative to drift velocity. There is also an additional uncertainty introduced from the magnetic field vector. The on board trigger system is passed an updated magnetic field eight times per second, not correlated in time to the native resolution of the FPI calculations. The ground based L2 moments use a much higher resolution magnetic field vector that has been corrected on the ground.

The spread around the linear fit is symmetric, consistent with randomly distributed error. While all terms do show a statistical distribution around the unity line, the frequency of points far ($> 10\%$) from the unity line tends to be small. The majority of data, therefore, can be said to lie close to the unity line having low associated error.

This is backed up by a histogram distribution of errors shown in Figure 4.5. Sharp peaks are present, centered around 1.0 (perfect correction) for all moments except for the magnetic parallel flux. Figure 4.4 shows that the magnetic parallel flux still has a concentrated focus of correction around the unity line, however, the statistical distribution is not as symmetric as other terms. The

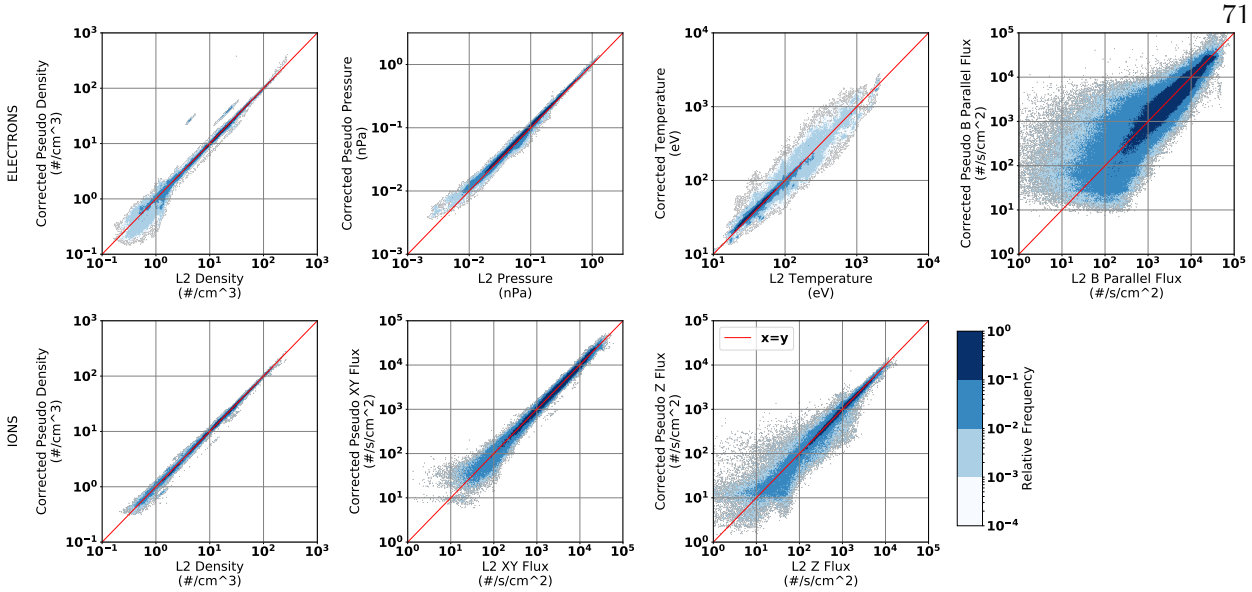

Figure 4.4: Final correction fits of the pseudo moments as a function of likelihood; electron data (top row) and ion data (bottom row). Pseudo moments are compared to Level 2 (L2) burst resolution data, that uses the best available corrections and time resolution.

correction algorithm prioritizes having an equal number of points on either side of 1.0, but does not correct skewness - thus the inherent skew in the data for magnetic parallel flux leads to a skewed final error distribution. The skew is due to the quantization present, which elevates the pseudo moment at values near 0.

Figure 4.6 shows the correction quality as a function of spacecraft potential, analogous to the raw correlation of Figure 4.3. When Figures 4.6 and 4.3 are compared, it is seen that the majority of spacecraft potential effects have been mitigated. One exception is unusually high spacecraft potentials, such as in the electron pressure and temperature, where a large patch of high S/C potential (> 25V) can be clearly identified. This error is due to the fact potentials of this magnitude are so infrequent that they are not heavily weighted statistically in the correction algorithm. More data at higher potentials would improve these corrections.

Note that each input quantity is correlated to the given output term in a series of weighted linear combinations and that some inputs may end up being more or less influential on the correction. For example, as seen in the raw data (Fig. 4.3), the spacecraft potential appears to be more

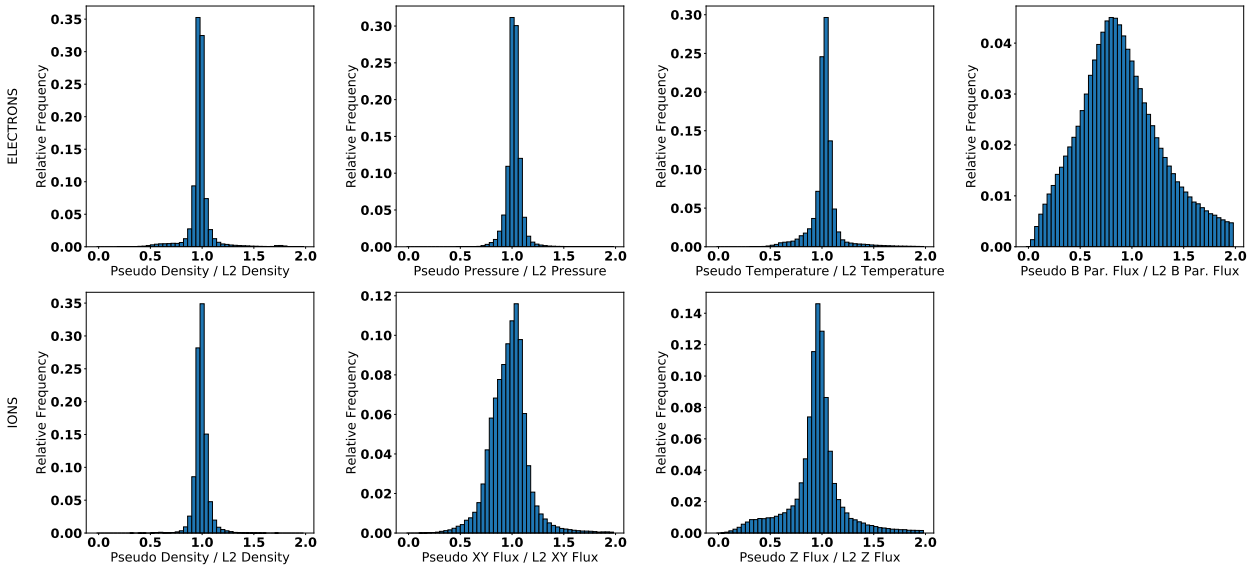

Figure 4.5: Histograms illustrating accuracy of trigger term to pseudo moment corrections. The value shown is a ratio of the corrected pseudo moment to the level 2 moment.

important for the electron terms than the ion terms. This helps to avoid the problem of overfitting, or correcting using a correlation that is not strongly supported.

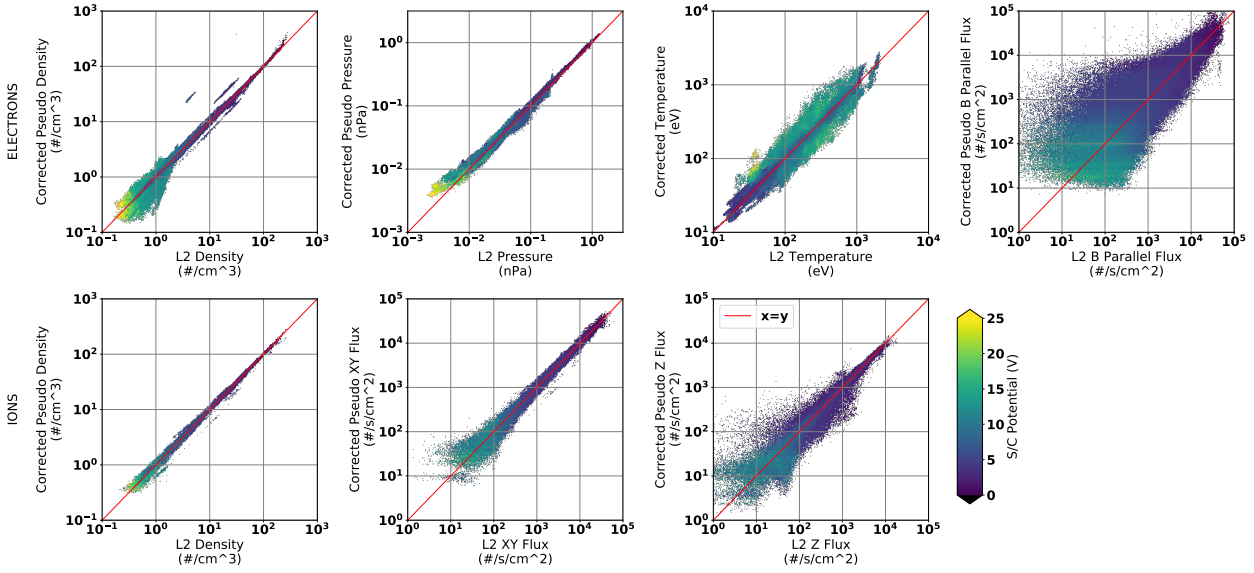

Figure 4.6: Trigger term corrections as a function of spacecraft potential. Note that while the highest bin is 30V, potentials have been observed in excess of 50V.

Because the corrections are statistical in nature, it is difficult to provide a reliable error bar for

all cases when releasing these data publicly. For each raw 0-255 term value, a standard deviation, σ will be calculated over all burst data maps associated with the given trigger value. For example, for an electron density term of 100, all burst L2 electron density data would be included that came from a timestamp where the electron density term was 100.

4.4 Flight Validation

4.4.1 Dynamic Range Scaling

As discussed in Section 4.3.2, the summations in Equations 4.11 - 4.17 form the set of raw trigger terms and range from 0-255. An ideal distribution would have data ranging from 0-255, with only a small amount of data in the 0 (quantized) or 255 (saturated) bins. This would mean that the system is using all available dynamic range without sacrificing any data. As shown in Section 4.3.3, the selection of scale factors determines the dynamic range of the trigger terms. Operationally, FPI uses three primary sets of scale factors, each targeting a different type of science. Table 4.1 shows the scale factor settings for each science region.

(1) **EM Sheath:** The electromagnetic (EM) sheath set of scale factors are targeting the the magnetopause. In particular, these are the regions where MMS is looking for magnetic reconnection on the day side. This set of scale factors are used below $\sim$ 16 RE, on the day side.

(2) **Solar Wind:** The solar wind set of scale factors targets the incoming solar flux beyond the bow shock. This set is loaded for the science regions greater than $\sim$ 16 RE, on the day side.

(3) **Tail Current Sheet:** This set of scale factors is targeting lower density regions in the magnetotail on the night side. This set is used at all radii on the night side.

Distributions of the trigger terms from 2017/2018 are shown in Figures 4.7, 4.8, and 4.9 for the EM Sheath, Solar Wind, and Tail Current Sheet sets of scale factors. These histograms

represent the distribution of the term values over the course of an MMS sweep through a given region. An ideal distribution would have a tail reaching zero likelihood at the quantization limit (0) and at the saturation limit (255). Data that are heavily quantized, with a large fraction of data in the 0 bin have the scale factors set too high. Terms that have a large amount of saturation, in the 255 bin, have the scale factors set too low. Per Equation 4.19, the look up table (LUT) used to bin the data from 0-255 is logarithmically spaced between 0 and 2^{16}. This means that a change in the scale factor of 1 would result in a shift in the histogram distribution of term values of $\sim$ 23-24 in either direction. Note that, while these terms could be shifted artificially to simulate the updated scale factors, this would not yield a correct result because the quantization and saturation cannot be recovered.

Figure 4.7 shows the distribution of all seven terms during December 2017 and January 2018, the center of a day side pass, when the EM sheath scale factors were loaded. This distribution appears multimodal because it covers from high voltage turn on, around 7 RE out past the bow shock at around 15 RE. This allows the spacecraft to pass through the inner magnetosphere, cross the magnetopause into the magnetosheath, and cross the bow shock into the solar wind. These different plasma regimes have different distributions in the term histograms.

In these distributions, the magnetic parallel flux shows a large amount of quantization, as evidenced by the high frequency of points in the 0 bin. This indicates that the scale factors for the magnetic parallel flux were likely set too high and they should be reduced. Similarly, the pressure term has some quantization and no values near 255, so this term could be shifted to the right by decreasing the scale factors. The ion fluxes also show a small amount of quantization, however the high end tail of the ion fluxes is nearing 255 so it would likely not be advantageous to shift these distributions to the right via a scale factor update. The density terms for both electrons and ions appear to be set appropriately.

Figure 4.8 shows histogram distributions of the December 2017 - January 2018 solar noon pass for times when the solar wind scale factors were loaded. Compared to the EM sheath distributions in Figure 4.7, these solar wind distributions are much narrower. This is because the solar wind

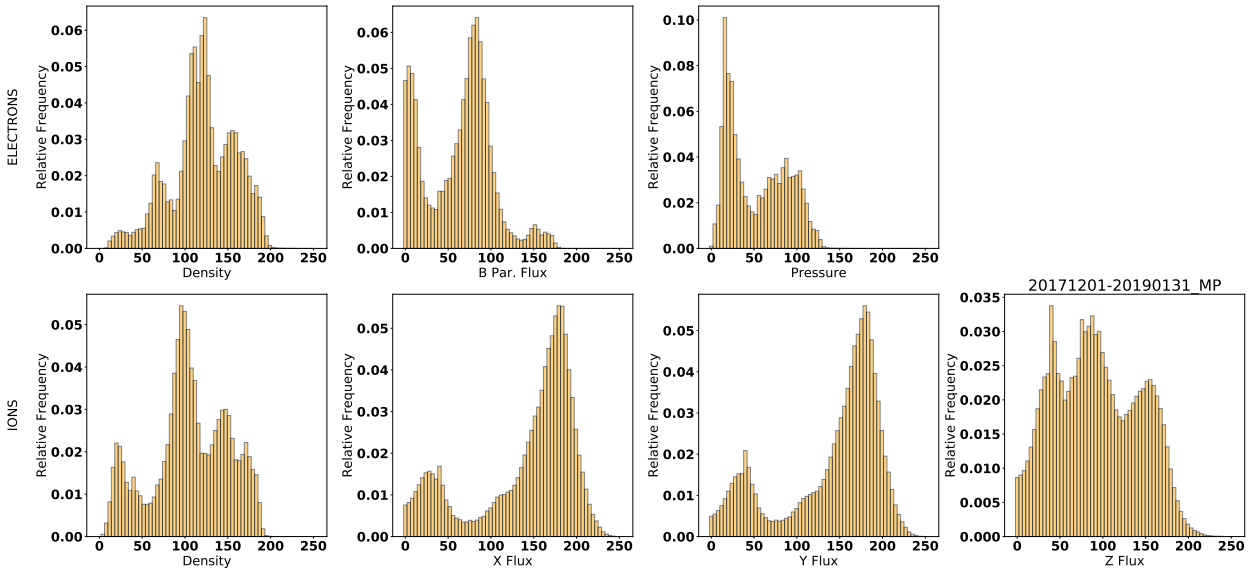

Figure 4.7: Histograms of 2017/2018 day side pass with scale factors tuned for magnetopause crossings. No saturation (255) of terms is present, however some quantization (0) is present in the ion fluxes and the magnetic parallel flux. Terms range from 0-255, where the term number scales logarithmically with the corresponding physical quantity.

scale factors were only loaded in the solar wind, and thus only one type of plasma is represented in the frequency data. There is a small amount of quantization in the ion Z flux term, however it is likely not enough to warrant an adjustment to the scale factors. Note that, while the scale factors can be adjusted to shift a distribution of terms, they cannot broaden or narrow a distribution of terms. For this reason, it would be difficult to broaden the solar wind term distributions to a full dynamic range of 0-255. The only way to broaden the distribution would be to alter the LUT binning table. Dynamically adjusting the LUT is possible, as it can also be updated dynamically with region, however this avenue has not yet been pursued due to operational complexity imposed on the ground system.

Figure 4.9 shows a histogram distribution of trigger terms during the 2017 tail pass, from June 20 through July 20. This represents two months centered around solar midnight. In this case, the distributions are divided into two colors. Orange (density term < 120) represents the prime science data, lower density plasma, near the central current sheet. Blue (density term $>= 120$) is largely inner magnetosphere and, while interesting, is not the prime science target during this

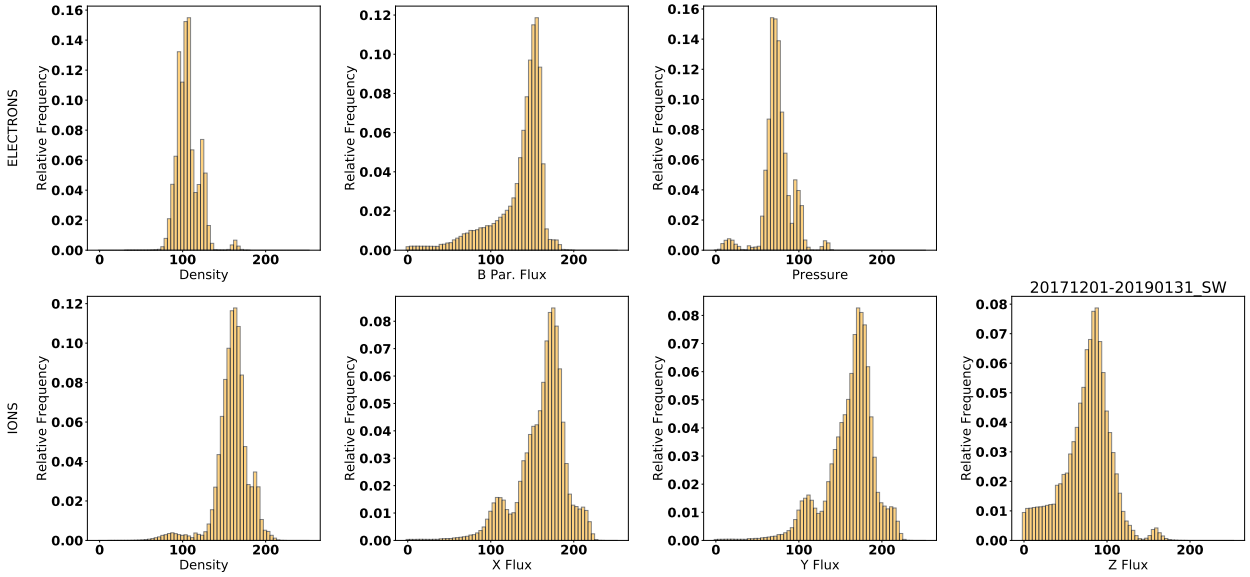

Figure 4.8: Histograms of 2017/2018 day side pass with scale factors tuned for solar wind. Terms range from 0-255, where the term number scales logarithmically with the corresponding physical quantity.

phase of the mission. The blue histograms are heavily saturated in the magnetic parallel flux and the ion fluxes, however this is acceptable in this case because the blue regions are not the prime science targets. During the tail season, the scale factors are set intentionally to acquire the best resolution (least quantization) possible for the lower density, tail data, while allowing the higher density data of the inner magnetosphere to saturate. It could still be argued, however, that some of these terms are still shifted too far to the right; in particular the magnetic parallel electron flux could be shifted to the left.

To exemplify this distinction in region, Figure 4.10 shows an energy/time (ET) spectrogram (ions top panel, electrons 2nd from top) for May 11, 2017. The bottom two panels show histograms of when the electron magnetic parallel flux (bottom) and ion x aligned flux (2nd from bottom) are saturated (red, term=255). There is a clear relationship between the count rate shown in the ET spectrograms and the amount of saturation. While there is some intermittent saturation earlier in the region, significant saturation begins to occur in the transition region around 15:00 and fully saturates after $\sim$ 17:00. The higher count rates at lower energies indicate that the spacecraft is

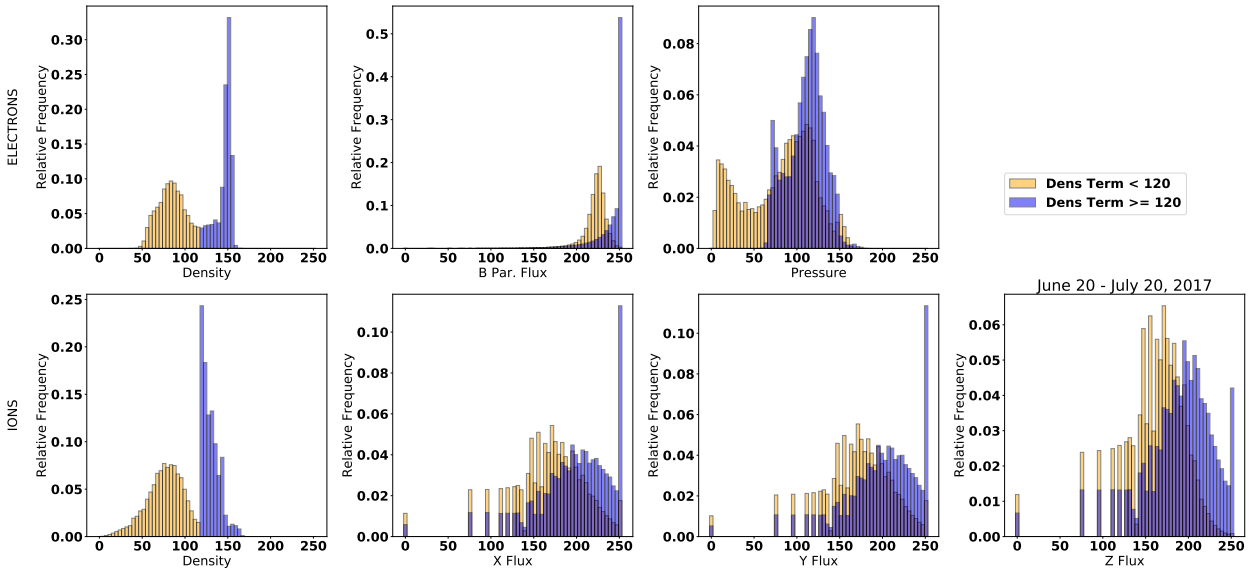

Figure 4.9: Histograms of the June 20 through July 20, 2017 pass through the central tail current sheet. Low density orange data represents terms likely to be from near the central current sheet. Higher density blue data is likely to be from the inner magnetosphere and not of prime scientific interest. Terms range from 0-255, where the term number scales logarithmically with the corresponding physical quantity.

no longer near the central current sheet, so it is OK if these data saturate. This is an example of tuning the scale factors for the prime region of scientific interest.

Figure 4.11 illustrates a problem with this set of scaling factors that was not anticipated prior to the first tail pass. The top two panels show ET spectrograms of ions and electrons, while the spacecraft is in the vicinity of the tail current sheet. The bottom two panels show frequency of saturation of the ion x aligned, and electron magnetic field aligned fluxes. Contrary to the May 11 case (Fig. 4.10) where the electron and ion flux saturation were largely in sync, this case shows that the ion flux never saturated, while the electron flux saturated for a large fraction of the data. The reason for this is shown in the ET spectrograms. The electron data shows a large red area of high count rate at the lowest energies prior to $\sim 12:00$. This high count band is not present in the ion data and has a sharp cutoff when it disappears. This high count population is photoelectrons and secondaries generated by the spacecraft and measured by FPI.

While it is expected that FPI will capture this population in the lowest energy bins, it was

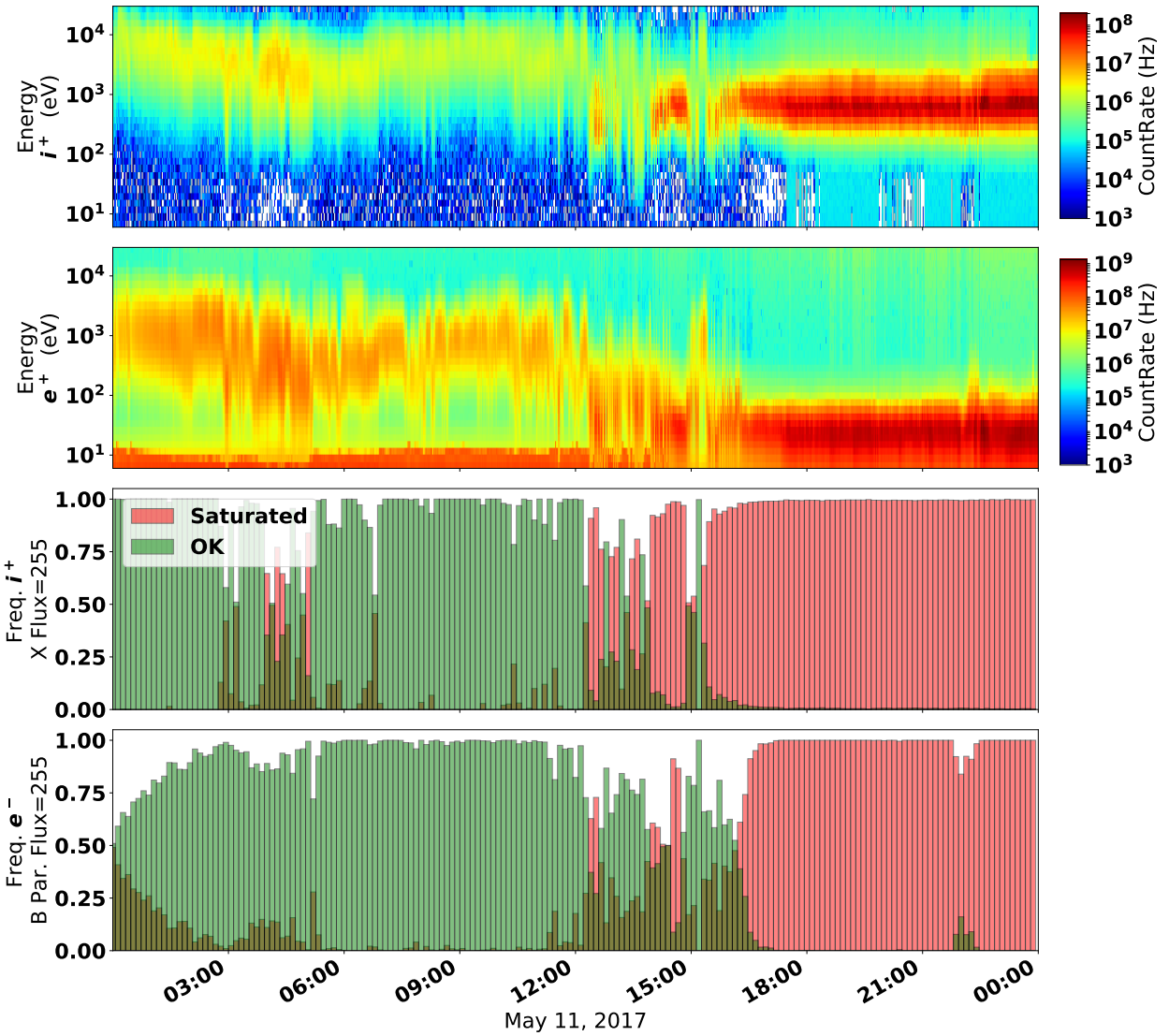

Figure 4.10: ET spectrogram for ions (top) and electrons (2nd from top) show a transition region into higher density plasma. The higher density regions correlate with frequency of saturation of the electron (bottom) and ion (2nd from bottom) flux terms.

not anticipated for this population to be of such a high intensity, or to reach such high energy levels[24]. The reason for this change in the photoemission / secondary emission population is that, in the first part of the interval, ASPOC is not emitting and there is no control on the spacecraft potential. The spacecraft potential then elevated to the 15-20 V range, which in turn accelerated the emitted electrons to higher energy bins, contaminating the DES measurement at low energies. This large influx of low energy particles caused the trigger term to saturate.

This type of saturation can potentially degrade science quality for the term and, as such, the scale factor will be adjusted for future tail passes to ensure that saturation is not present in similar regions even if there is an elevation of the spacecraft potential resulting in a surge of low energy electrons collected.

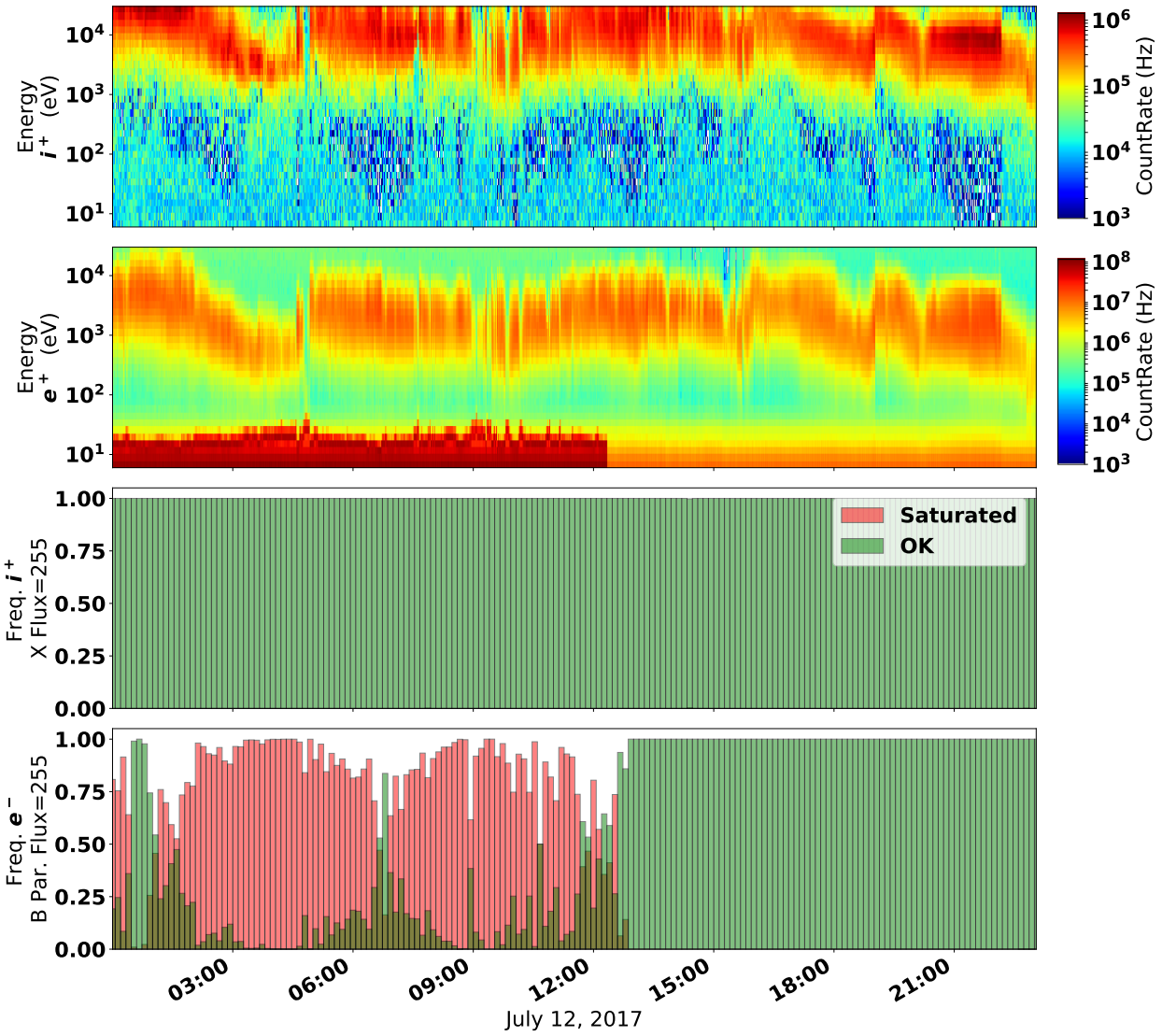

Figure 4.11: ET spectrogram for ions (top) and electrons (2nd from top) show a data segment near the central current sheet in the magnetotail. Prior to 12:00, the spacecraft potential was not controlled and floated into the 15-20 V range, resulting in a significant contamination of the lower energy electron data. This correlates with saturation of the electron magnetic parallel flux term (bottom).

Overall, the trigger term distributions are acceptable, particularly given that they were chosen

prior to launch, with no data to use as a baseline. For future phases, however, the scale factor sets will be updated periodically based on this and future analyses.

The correction seed data was taken from January through March of 2016. As a validation, the corrections were applied to an event from December of 2015, outside the range of the seed data. This is an interval of kinetic Alfvén waves observed near the magnetopause as studied by Gershman et al. [23]. Figures 4.12 (electrons) and 4.13 (ions) show this interval, comparing the corrected pseudo moments with the studied burst resolution level 2 moments as well as the 4.5s fast survey data. Good agreement is shown on all moments, with a notable increase in error in the low flux regions as shown previously. In this same region, the density and temperature errors increase as well, however, this appears to be statistical noise from the low count rates experienced at densities below 1/cc. Some variability in the magnetic parallel flux is also not present, likely due to quantization in low values and uncertainty in the magnetic parallel flux, as discussed earlier. The pseudo moments are able to resolve the entire dynamic range of the event, resolving an order of magnitude in flux, density, temperature, and pressure. More specifically, the wave nature of the interval is clearly visible in the pseudo moments, allowing for further analysis of the wave properties. This is of particular note, because the wave nature is entirely absent in the fast survey data, which is the only other available data for large percentages of the orbit. This emphasizes the importance of a high time resolution product for times when burst resolution data is not available.

Figures 4.14 (electrons) and 4.15 (ions) show a zoom of time index 22:26 on the December 30th 2015 interval. This region shows, in detail, the observed wave structure of the plasma moments. The pseudo moments accurately resolve the observed wave structure in all cases. Note that while the density and pressure pseudo moments match almost exactly with the burst data, the temperature pseudo moment has a systematic error over the entire interval. The temperature, in this case, is low ($\sim$ 40 eV), which therefore introduces some amount of quantization error. The systematic offset is on the order of the quantization limit ($\sim$ 1 LSB (least significant bit.)) The variation in temperature is also quite small; the amplitude of the wave in the temperature profile is 3-4 LSBs for the pseudo temperature, meaning that the amplitude of the wave is nearing the quantization

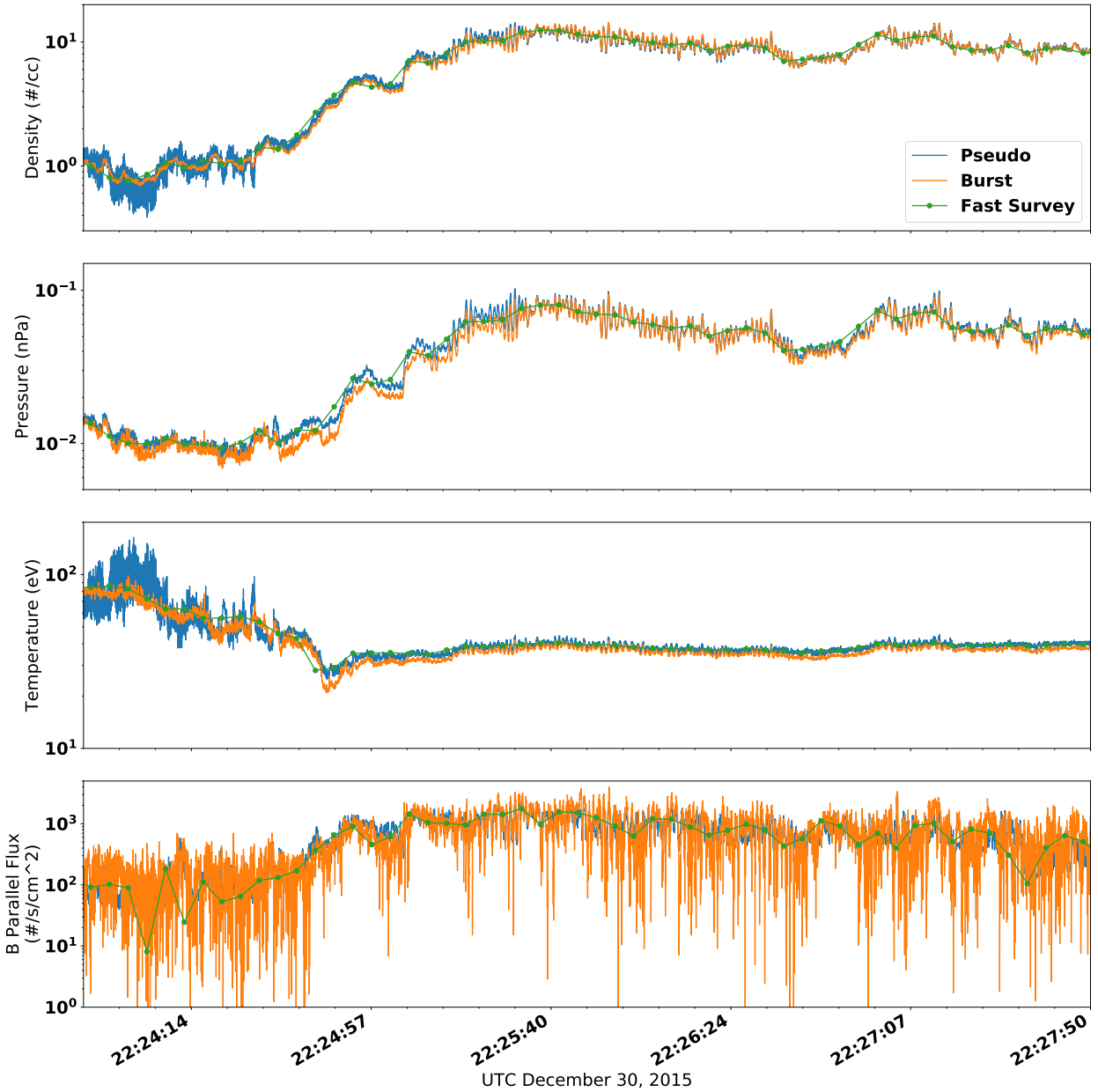

Figure 4.12: December 30, 2015 (MMS1); Electron pseudo moments (blue) compared to level 2 burst resolution data (orange) and fast survey (green). From top: magnetic parallel flux, temperature, pressure, number density.

limit. This quantization could be lowered via adjusting the scale factors, but there is no scale factor associated strictly with temperature, rather it is a combination of the density and pressure scaling, and adjusting those would affect their corresponding corrections.

Figure 4.13: December 30, 2015 (MMS1); Ion pseudo moments (blue) compared to level 2 burst resolution data (orange) and fast survey (green). From top: spin plane (XY) flux, spin aligned (Z) flux, number density.

4.5 Conclusion

FPI has incorporated a system for calculating on board trigger terms, which can be corrected into physically meaningful pseudo moment quantities. They are proportional to plasma moments integrated by the ground system. During design, these trigger quantities were intended not for use as a science product, but merely as an indicator to be used for ranking data by scientific interest. Two innovations have been introduced in this system, however: tuning the dynamic range of the system to specific plasma regimes minimizing error, and correcting the data using a trained

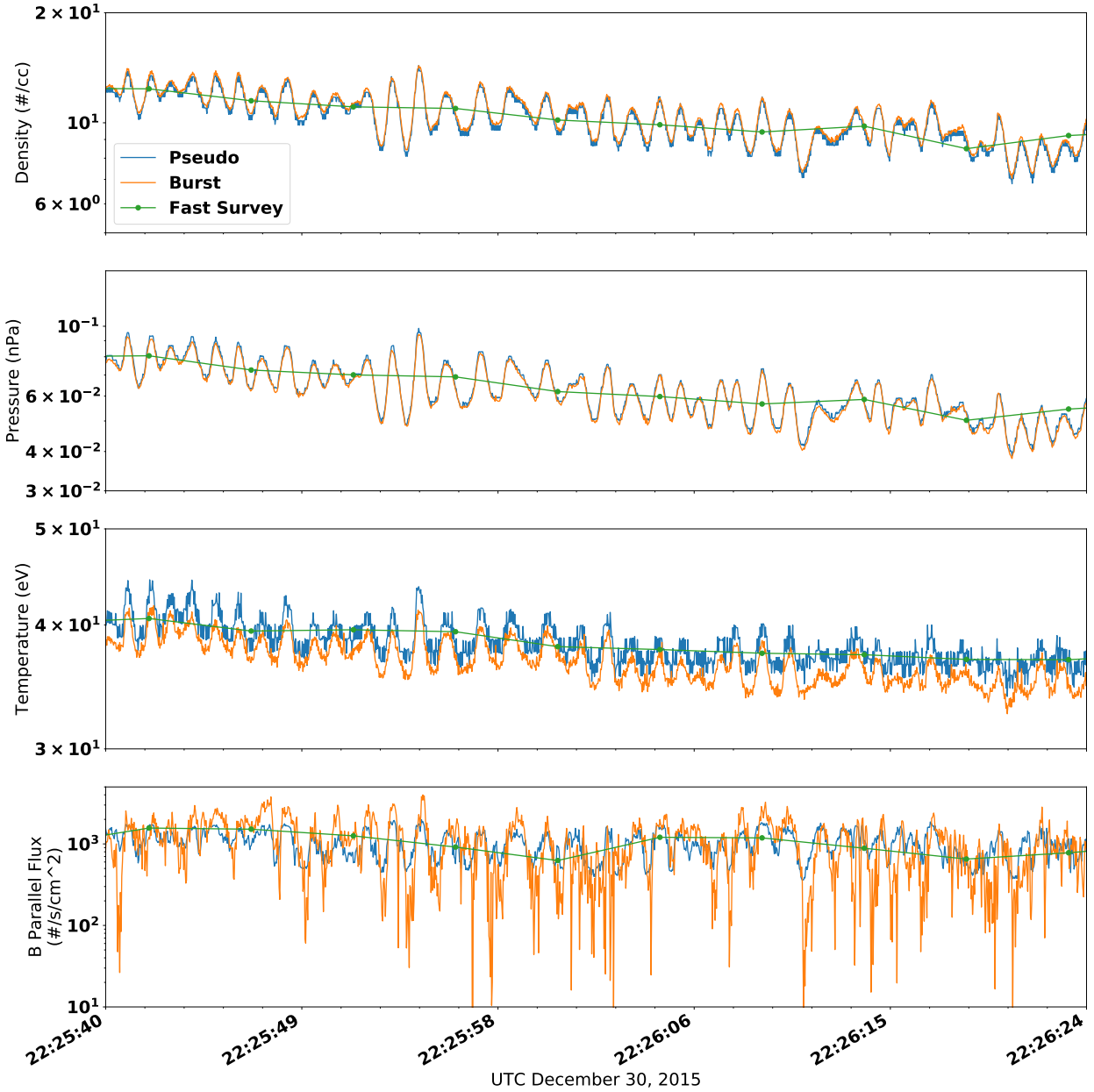

Figure 4.14: December 30, 2015 (MMS1); capture of Alfvén wave structure in electron pseudo moments zoomed around the 22:26 time index.

neural network. The corrected product is a physically meaningful pseudo plasma moment. The resolution and level of detail evidenced by these pseudo moments has illustrated that they may be used as a science product in and of themselves. This is highly desirable because the trigger terms are downlinked for all times when FPI is operating in the nominal fast survey science mode. By

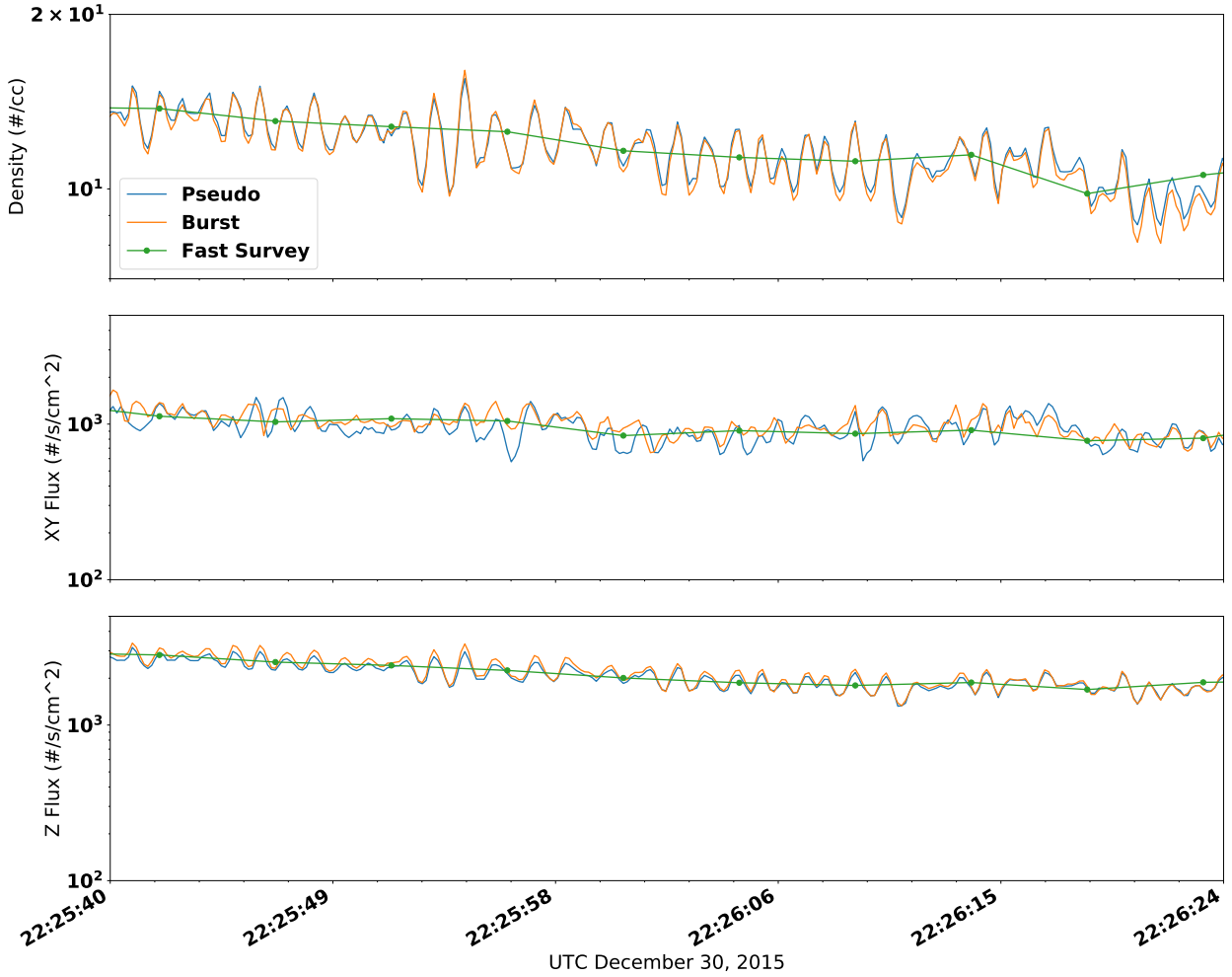

Figure 4.15: December 30, 2015 (MMS1); capture of Alfvén wave structure in ion pseudo moments zoomed around the 22:26 time index.

contrast, only $\approx 5\%$ of the high resolution burst data is downlinked. The trigger term based pseudo moments have been shown to be accurate when compared to a previously published detection of kinetic Alfvén waves and statistically accurate over the course of three months.

The time resolution of the trigger terms is 30 ms for electrons and 150 ms for ions. These terms are downlinked as part of the fast survey data product and are available throughout this operating mode. Corrections were performed using magnetic field and spacecraft potential data also present in the fast survey data. This allows for scientific comparison of the plasma moments with field data using only data contained in the fast survey packet. While not strictly a component

of the level 2 data processing, it is expected that corrected FPI pseudo moments, such as shown here, will be made available for the entirety of the MMS mission. Having a high time resolution science product for the entire science region poses a huge asset to the scientific community of MMS. More broadly, the techniques introduced here may open up future missions to on board moment calculations.

Chapter 5

Sheath Effects on Particle Trajectories

Portions of this chapter are taken from:

AC Barrie, Z Sternovsky, and S Elkington. Correcting particle measurements for potential sheath effects. In Preparation

5.1 Introduction

On each spacecraft, FPI measures particles using four DES and four DIS. The units are placed 90 degrees apart on the spacecraft and each has a 90 field of view in azimuth, allowing for a full 360 degree view among the four together. As the particles approach the MMS spacecraft, they are affected by a plasma sheathing effect, resulting from the spacecraft potential[57, 44, 20]. This potential sheath alters the trajectories of the particles affecting both direction and energy. FPI corrects for the energy by simply adjusting the measured energy by the spacecraft potential[54, 25]. The directional error, however, is not currently accounted for.

There are several factors that make this effect hard to correct for:

(1) The sensors are not in the same physical location on the spacecraft, but are spaced on the perimeter, 90 degrees apart, and are thus exposed to different plasma sheath environments.

(2) The spacecraft potential, which drives the sheath geometry, is variable over time and is mitigated by an Active SPacecraft POtential Control (ASPOC) system that emits a plume of positively charged indium ions into a highly localized area of the sheath[63]. The Elec-

tron Drift Instrument (EDI) also emits charged particles (electrons), affecting the sheath environment[62, 61].

(3) MMS has eight long booms that measure magnetic and electric fields. These booms will also have a charge on them which affects the sheath in a local area near the booms[9, 61, 36].

(4) FPI measures electrons down to 6 eV and ions down to 2 eV, where a spacecraft charge of several volts can have a profound effect[52].

(5) The spacecraft is spinning, and moving through space, making the sheath environment a constantly evolving process.

These factors lead to a local electric field around the spacecraft that is nonintuitive and not easily modeled analytically. Some work has been done on analytical models for simplified spacecraft in stationary environments[57, 44, 20], and limited work has been done on modeling sheath effects computationally[22, 59, 16, 30].

This work introduces a method whereby a detection efficiency map is created which can be used to identify errors in the measured counts, and in some cases, correct the count rates measured by FPI, or a similar instrument. A map of the spacecraft potential sheath is modeled in a commercial spacecraft charging code, Spacecraft Plasma Interaction Software (SPIS)[56], including emission from the ASPOC plumes (other codes, such as NASCAP-2K[38] would work as well.) Simulated particles are flown through the resulting electric field and collected using a numerical integration routine and initial trajectories are compared to final trajectories. A statistical map of detection bias is created, corresponding to the energy/angle bins used by FPI, which could be used to identify sources of error and correct for some sheath effects.

5.2 Algorithms

5.2.1 Potential Map

The interaction of the MMS platform with its plasma environment was modeled to study the effects of the emitted ASPOC plume, with results used here, with permission. SPIS v5.2.4[56] was used for this simulation. SPIS uses a Newton type solver to approximate the spacecraft geometry as an electric circuit, while using a combination of Particle in Cell (PIC) and several preset distribution functions to solve for space charge. The multi-physics approach allows the ambient environment to inform the charge state of the spacecraft, and vice versa. The spacecraft geometry was simplified to include all spacecraft surface elements including the Spin-plane Double Probes (SDP)[36] and the Axial Double Probes (ADP)[18], as well as the ASPOC system, but not the fine details of the model, such as fasteners, etc. In this model the ambient space potential and spacecraft potential are self-consistently solved accounting for the ambient plasma population densities and temperatures, as well as spacecraft generated photoelectrons and secondary electrons, and ASPOC beam ions, for given illumination conditions and ASPOC operating currents. The specific conditions chosen for this simulation, shown in Table 5.1, were based on the ambient MMS environment from 2016-08-14 at $\sim$ 08:00 UTC.

Parameter	**Value**
Number Density	0.5/cc
Electron Temperature	900 eV
Ion Temperature	5200 eV
Electron Drift Velocity	0 km/s
Ion Drift Velocity	25 km/s
Spacecraft Potential	4.6 V

Table 5.1: Plasma parameters used for SPIS charging simulation. Values are approximations of MMS values from 2016-08-14, 08:00 UTC.

The resulting potential map from the SPIS simulation is shown in Figure 5.1. Two plumes from the ASPOC emitters are clearly visible, as are the long wire booms (SDP) and axial, ADP, booms. A diagram of the MMS spacecraft is overlaid on the figure to provide context and annotate

the locations of the FPI sensors. The provided azimuth reference is maintained throughout this work. While the spacecraft potential is maintained at 4.6V, the ambient potential reaches 7.6V in some locations. Note that the two ASPOC plumes are not identical, as the more sunward of the two has a greater degree of neutralization from spacecraft emitted photoelectrons.

5.2.2 Particle Traces

Particles are launched from the instrument aperture and propagated through the electric field until they exit the domain, at a distance of 17 m. Particles had to be flown in the reverse direction (away from aperture) because many particles launched from the edge of the domain would not be detected at the aperture location.

The python scipy ODE function was used to integrate particle position and velocity, using the *lsoda* integrator[49, 43]. This integrator was chosen because it can adaptively switch between integration techniques based on the local stiffness of the current integration step. Integration steps were performed manually for two primary reasons:

(1) The equations of motion are based in time, however the integration is based on distance. This means that it is difficult to pass an exact time range to the integrator. Rather, it is easier to manually continue integration steps until the particle crosses the 17 m threshold and then break the integration routine.

(2) For each individual step of the integration from point to point, python controls the internal timestep of the integration. When choosing how far to place the next integration point, however, an adaptive timestep was calculated based on the local electric field and particle velocity. This is opposed to passing a predetermined set of time points into the routine for a complete end to end integration. A typical particle trace was composed of $\sim$ 10,000 points.

The integration was not performed with a predetermined set of timesteps to solve fed to the integrator, but rather each integration point was evaluated to determine the next integration

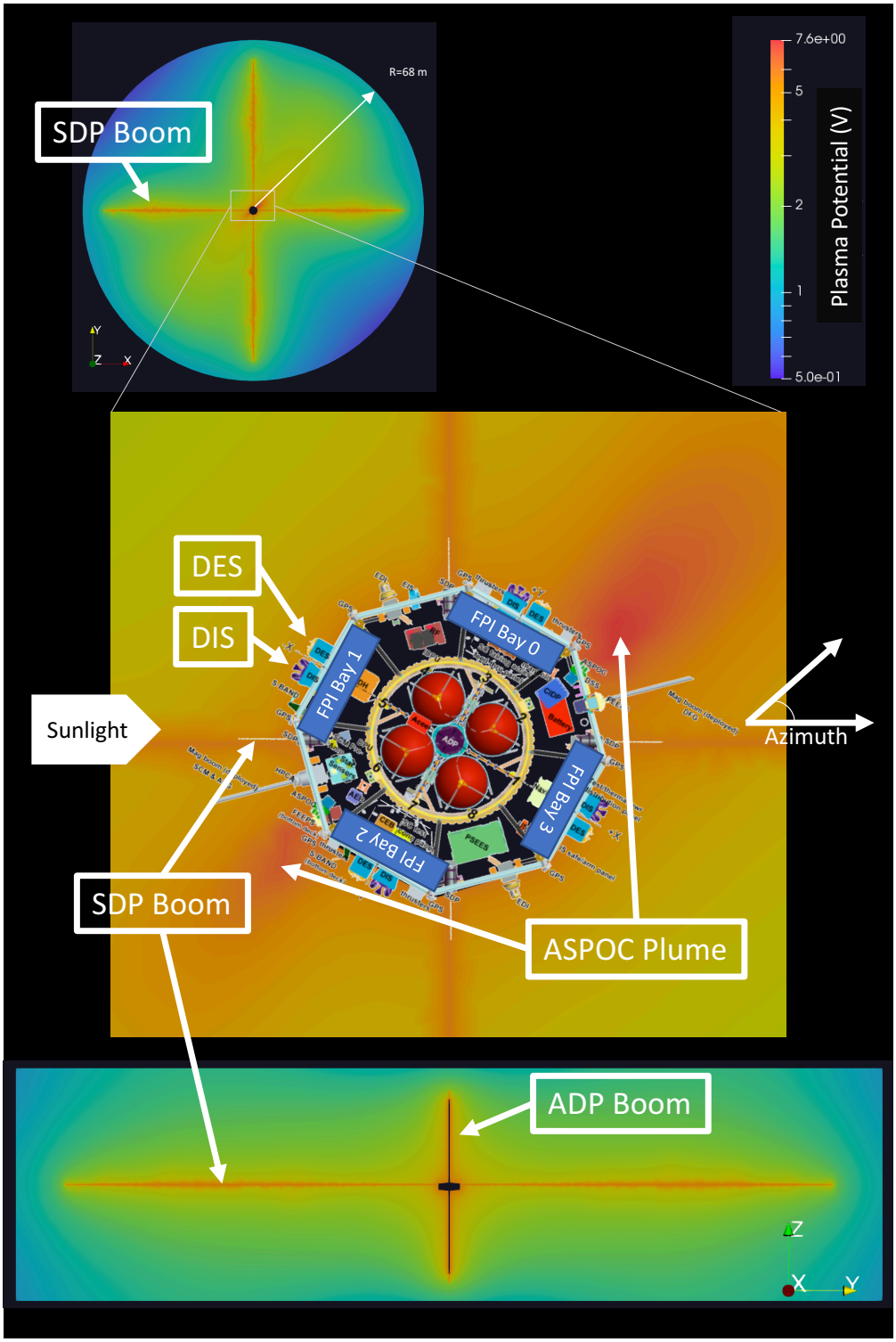

Figure 5.1: Ambient potential as calculated by SPIS model. The center panel shows a zoom in of the area near the spacecraft. MMS spacecraft is overlayed showing instrument locations. Annotations show areas of concentrated potential as well as the FPI sensor locations. Note that similar DES/DIS pairs are in all four of the annotated FPI bays. Azimuth angle for all future figures is as annotated here as is the direction of the Sun.

timestep. This evaluation of the timestep, dt, was based on the instantaneous particle velocity, $\vec{v}$, and acceleration, $\vec{a}$, as:

$$dt = \frac{C}{|\vec{a}||\vec{v}|} \tag{5.1}$$

where C is a constant chosen such that the particles typically exited the domain in about 10,000 steps. Electric field, $\vec{E}$, is the primary force mechanism. Because the magnetic field can vary quickly and time, and it would be impractical to parameterize over all possibilities, the magnetic field was ignored for this case study. This approach is justified due to the gyroradius being much larger than the simulation domain ($\sim$ 1 km for a 10 eV electron in a 10 nT field.) This decision is validated further in Section 5.4. The equation of motion to be integrated is therefore:

$$md\vec{v} = -q\vec{E}dt \tag{5.2}$$

Note the negative sign on the right hand side; this is applied to computationally integrate the particle paths backwards from the aperture to the domain boundary. For the final simulation run, four million particles were flown per species (electrons/ions), one million from each instrument. The trajectories were evenly distributed over a unit sphere (90 degrees per instrument) with logarithmic energy sampling from 10 eV to 30 keV. The energy range corresponds to the energy range of FPI upon launch. Histograms of the particle distributions are shown in Figure 5.2.

The overall process for the simulation is as follows:

(1) Load background potential data (as calculated in SPIS model)

(2) Solve gradient to obtain electric field

(3) Sample n particles from a predefined logarithmic energy / spherical angle distribution

(4) For each particle:

  (a) Place at instrument aperture

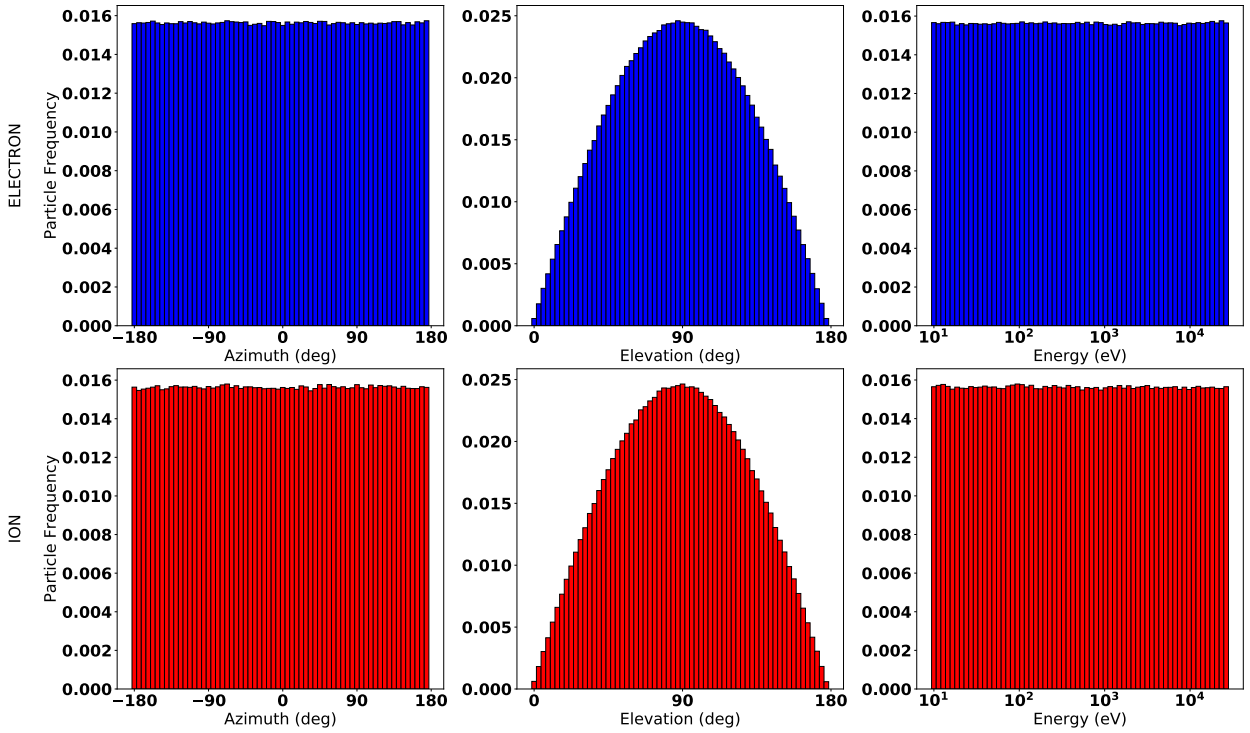

Figure 5.2: Histograms of particle distributions for electrons (top) and ions (bottom). Distributions are uniform over a unit sphere and logarithmically sampled from 10 - 30,000 eV in energy. A total of 4,000,000 particles were sampled.

(b) While in the domain (within 17 m of aperture):

(i) Calculate acceptable time, t' to next integration point based on local field strength and particle velocity

(ii) Use *lsoda* to integrate particle position and velocity up to t'

(c) Remove particle from the domain

(5) Record all data to file

Errors are recorded as differences between the detected particle (at launch) and the true particle (at domain exit). Error in energy, elevation, azimuth, and combined angle are recorded for each particle trace.

5.3 Results

Particles were binned into 32 uniformly spaced azimuthal bins, 16 uniformly spaced elevation bins, and 32 logarithmically space energy bins. These bins were chosen to match the FPI measurement space. For each bin, a detection bias, η_d, was measured by comparing true particles counted, c_t, and detected particles counted, c_d, per bin:

$$\eta_d = \frac{c_d}{c_t} \tag{5.3}$$

An angle-angle plot of detection bias, η_d, for the lowest energy bin (10 - 13 eV) is shown in Figure 5.3. The azimuthal angle is referenced as in Figure 5.1. Both electrons and ions show a non-uniform detection bias, with some areas reaching a +/- 50% bias. As expected, the electron map is largely an inverse of the ion map due to the opposite polarity. Several areas of localized bias are annotated by green numbered circles:

(1) The top and bottom horizontal bands are caused by charging of the ADP boom, along the spacecraft spin axis (roughly GSE Z). This is shown in the bottom panel of Figure 5.1.

(2) The large blobs are effects of the ASPOC emitter plume.

(3) The small squares and vertical bars are caused by the SDP wire booms, in the spin plane.

Figure 5.4 shows a full bias map for the entire energy range. The vertical dimension represents 32 stacked sequences of 0 to 180 degrees in elevation, with energy increasing towards the top of the plot. This is, essentially, 32 stacked angle-angle plots as shown in Figure 5.3, one per energy bin. This format is consistent with an FPI energy/angle skymap[52]. As such, the horizontal striping that is seen is representative of changes over elevation, whereas the gradual fading of the color is representative of changes over energy. While the bias does fall off with energy, there are still areas of high bias ($> 20\%$) even upwards of 1,000 eV. These areas tend to be the areas associated with the SDP booms. This makes sense as the SDP booms are 60m long, thus effecting the local environment over a large distance. This is noteworthy, as this effect could help to explain spin

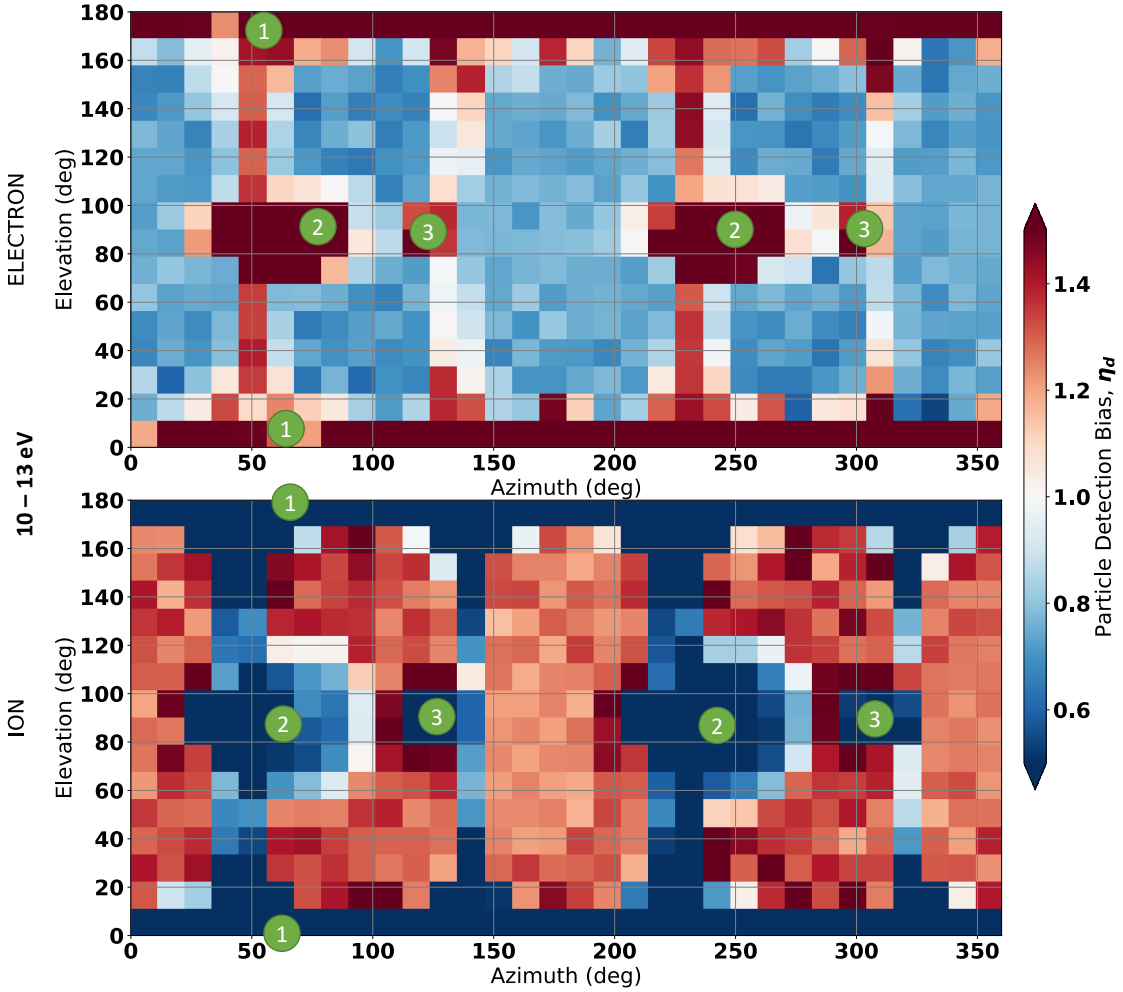

Figure 5.3: Detection bias map for electrons (top) and ions (bottom) for the lowest FPI energy range (10 - 13 eV). Red areas represent a region of overcounting, blue areas represent areas of undercounting. Green circles are areas of particular interest.

tones in the high energy data, or data collapsed over energy, associated with signatures fixed to the spacecraft reference frame, such as illustrated in Figure 3.9. This result is consistent with that found on CLUSTER[16], that the wire booms are one of the primary drivers of electrostatic steering effects.

Figure 5.5 shows a statistical distribution of trajectory error versus energy. In this distribution, at 1,000 eV, there are no particles with greater than a one degree error in angle. What this implies is that, while the particles near the SDP boom may have been pushed to a different detection bin, they were not pushed very far in an absolute sense. The distribution of angular

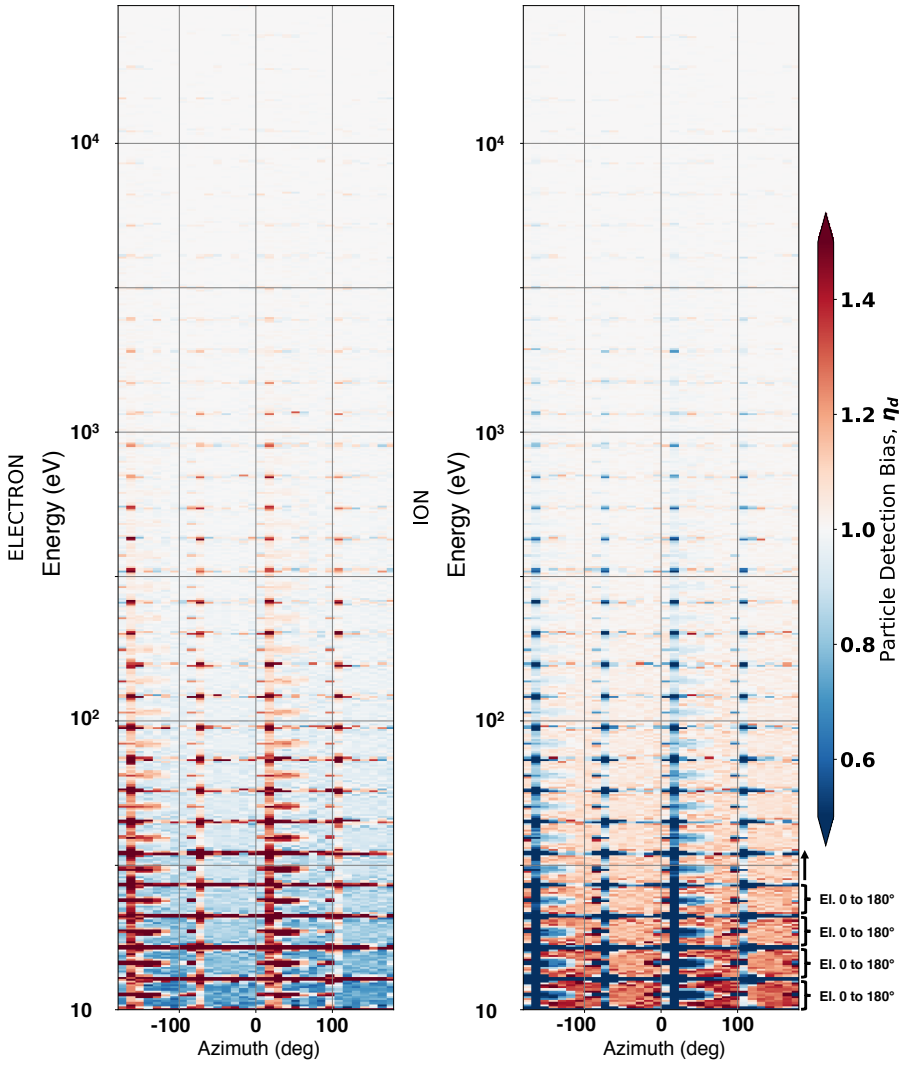

Figure 5.4: Detection efficiency map corresponding to an FPI energy/angle sky map for electrons (left) and ions (right).

error with respect to energy shows a consistent, predictable behavior with maximum error of ~ 30 degrees at 10 eV.

Figure 5.6 shows a calculated error and uncertainty based on the distributions from Figure 5.5. A Gaussian was fit to vertical (energy) slices and the peak of the distribution and standard deviation were calculated. These serve as a convenient metric for error and uncertainty that can be communicated to end users of the data.

The error distribution is quite wide for a given energy, meaning that the error in angle is

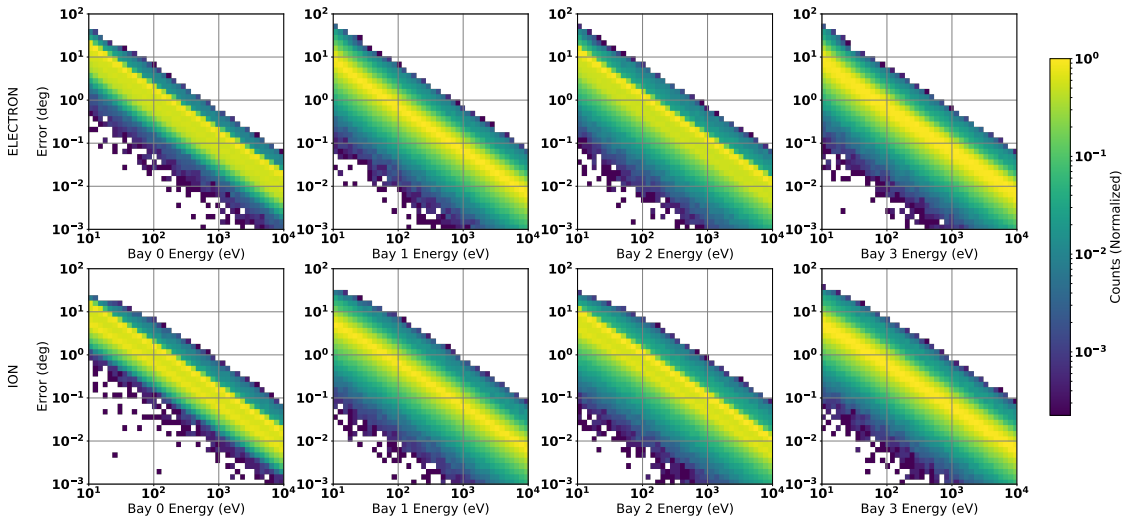

Figure 5.5: Absolute error in trajectory angle as a function of energy, separated per bay.

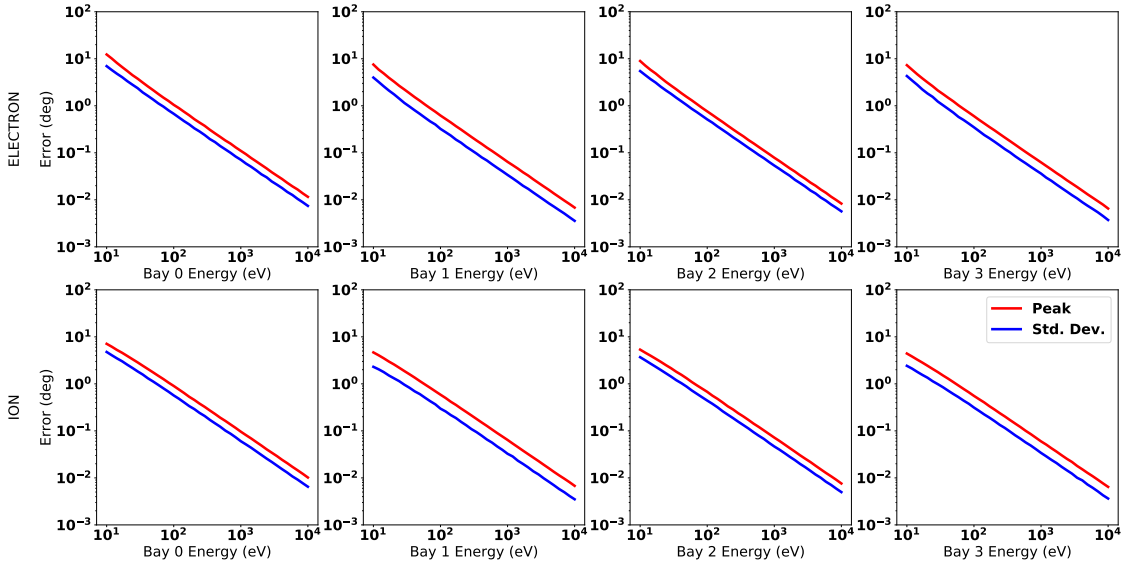

Figure 5.6: Estimation of error and uncertainty for a trajectory measurement versus energy, taken from a gaussian fit to the error distribution data in Figure 5.5. Data is plotted per bin and species.

highly dependent on the exact trajectory. More precise descriptions of error can be made on the basis of energy and look direction. Figure 5.7 shows a distribution of detected particle error per elevation and azimuthal bin. A particle at (0,0) would therefore have no associated error and be detected with the correct trajectory. Bays 0 and 2 show a clear asymmetry to one side in azimuth. This is consistent with the location of the ASPOC plumes, as seen in Figure 5.3. All bins show a

bimodal distribution with a depression in counting around an elevation of 0. This is consistent with the effect of the SDP booms shown in Figure 5.3. Note that this figure is collapsed over energy, not limited to the lowest energy bin. This means that most of the particles (higher energies) have lower associated error, thus the peak of the distribution around (0,0).

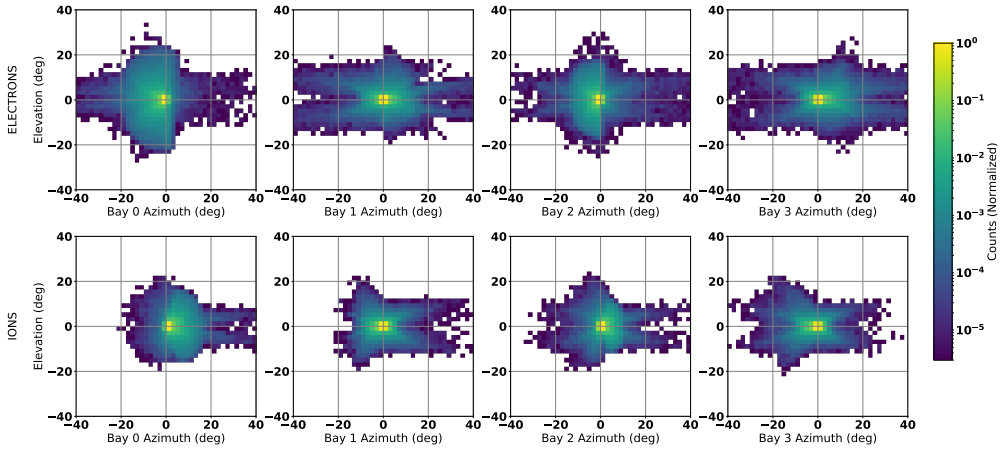

Figure 5.7: Distributions of detected particles per bay, collapsed over all energies. Note that the ASPOC plumes are located in bays 0 and 2 and the SDP booms lie at 0 elevation.

Overall, the simulation paints an interesting picture: while MMS had a pre-launch requirement for no more than a single volt of potential between any two points on its surface throughout flight, the absolute spacecraft potential combined with the long booms and emitted plumes make for an asymmetric and non-uniform distribution of collected particles.

5.4 Flight Validation

To validate the bias map, the 10 - 13 eV bias (Fig. 5.3) was compared to FPI flight data from the 2016 tail phase. Over 1000 regions were analyzed - all data from August 2016 where the spacecraft potential was between 4 - 5 V. While there were subtle differences, all examined maps were qualitatively similar. Figure 5.8 shows an example for electrons from the morning of August 13, while Figure 5.9 shows several intervals from varying times in August, 2016, with the axes removed. Each case is an average for entire burst interval, encompassing several minutes of data. The flight data is normalized to average counts per analyzer; data from each of the eight analyzers

is independently normalized to account for variations in analyzer efficiency. The resulting bias map, therefore, is assuming that at this lowest energy bin, the true plasma is isotropic for electrons over the course of several minutes. This uniformity over several days helps to validate the assertion that, while the magnetic field may change over time, it does not have a profound effect on the resulting trajectory bias distribution.

Figure 5.8 shows some qualitative agreement between the flight (bottom) and simulated (top) data, however several differences exist between the simulated and flight maps:

(1) The ADP signature is smooth and consistent in the simulated data, while is appears ragged and nonuniform in the flight data.

(2) The signatures in the simulation associated with the ASPOC plume ($\sim$ 70 and 250 degrees) are not in agreement with the flight data. The flight data shows a similar structure around 200 degrees and no secondary signature. This discrepancy becomes more glaring when compared across all four spacecraft, as is done in Figure 5.10. While the boom signatures appear similar in the four spacecraft, the plume signature looks markedly different, with possible locations annotated with green arrows.

(3) The square artifacts associate with the wire booms are present and similar in both simulated and flight data, however the magnitude of the vertical stripe is not consistent between the two (although it is present in both).

It is likely that some of these issues have to do with model fidelity. Specifically, the ADP is a complex lattice structure that is difficult to model with a surface mesh. The simulation mesh is likely not able to resolve the fine features of the electric field and particle trace around the latticework at the given resolution. It is also possible that there is some natural variation in the ASPOC plume due to manufacturing and assembly differences in the emitters. A larger impact, however, may be from the fact that the spacecraft simulation was stationary with respect to the sun. The photoelectron signature was therefore asymmetric. In practice, the ASPOC signature

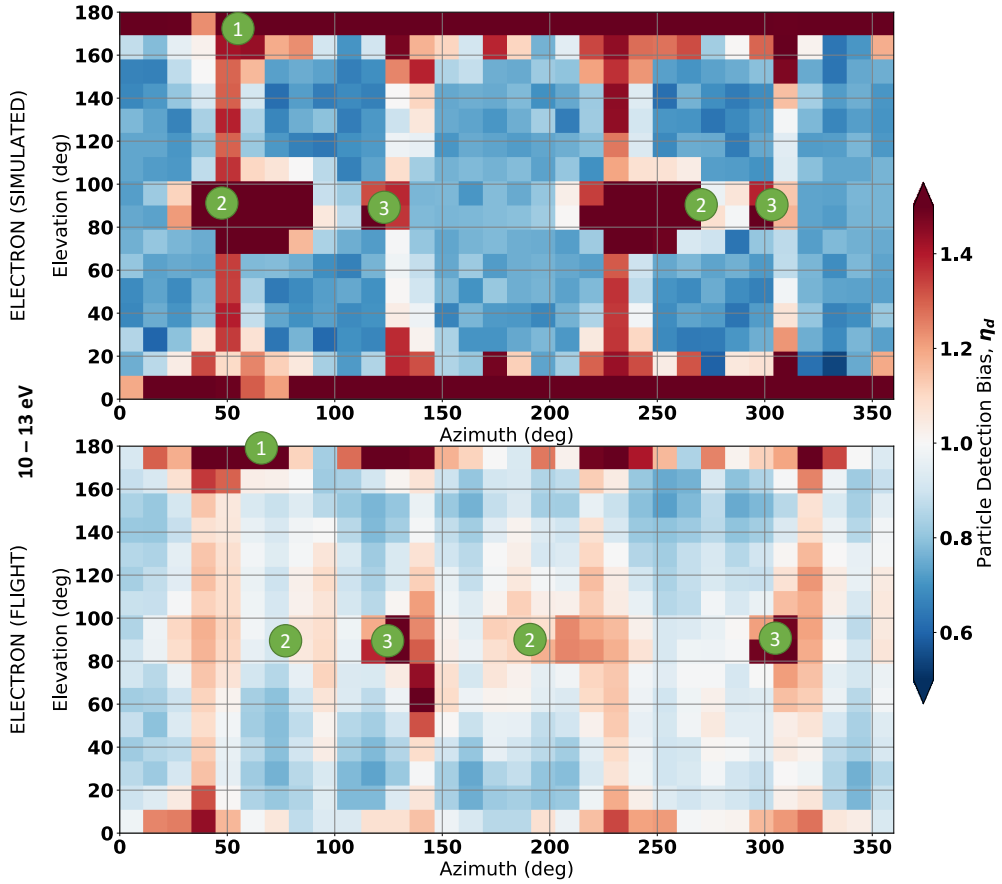

Figure 5.8: Comparison of simulated data (top) to flight data (bottom) for particle detection bias. Data is from MMS1, August 13, 2016, at approximately 08:12 UTC. Data is for the lowest energy bin, 10-13 eV. Flight data is normalized by mean counts per analyzer. It is assumed that the lowest energy electrons are isotropic over the course of the measurement.

would be affected in a different way from photoelectrons than in the static model. Because the flight images shown here are all integrated for up to several minutes (due to low counting statistics), the photoelectron signature would have migrated over a large range in azimuth. Similarly, solar flux was held constant in the model. Variations in solar conditions, particularly times of increased solar activity, flares, coronal mass ejections, etc, can alter the photoelectron emission and corresponding neutralization of the ASPOC plume.

The uniformity of the different regions selected in Figure 5.9 is encouraging as they do not strictly match the stated conditions in Table 5.1. The min and max of relevant parameters from the flight data for electrons is presented in Table 5.2. While all of the density numbers are low

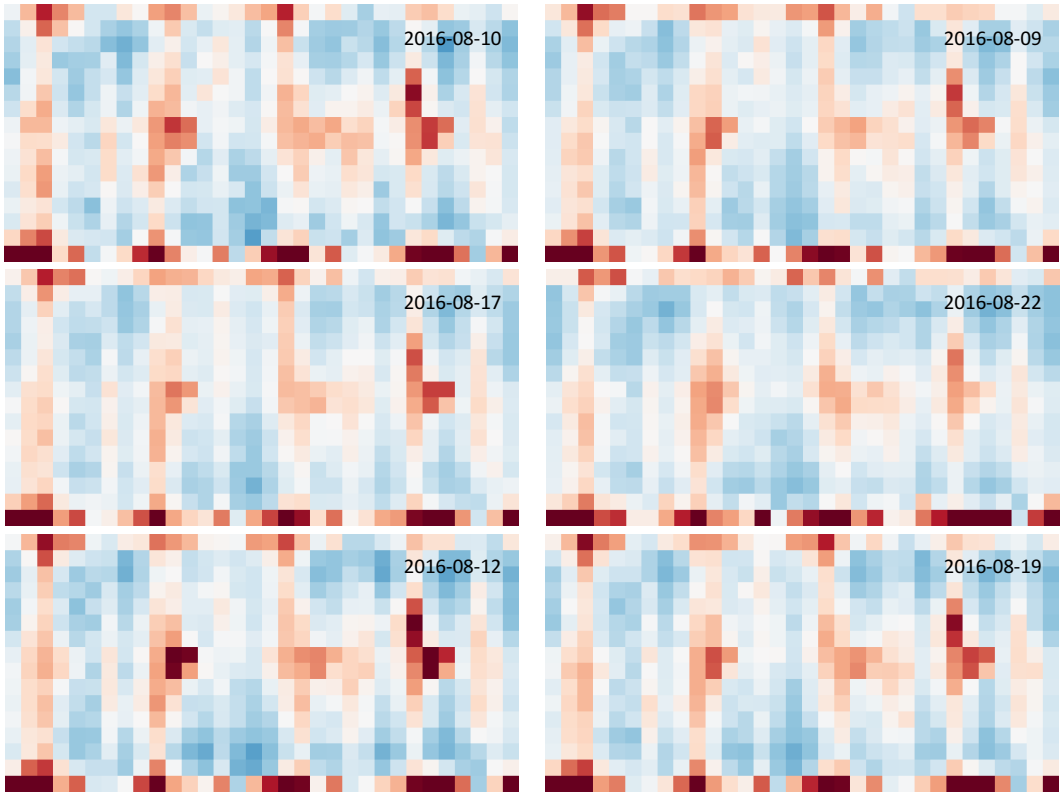

Figure 5.9: Flight electron (DES) bias maps from six selected regions from August, 2016. Axes and color scale are the same as in Figure 5.8. All maps show a similar qualitative shape with minor differences.

(all data was taken from the tail region), there is a factor of eight difference in the density, and a factor of two in the spacecraft potential. There was also a wide range of electron temperature, over two orders of magnitude. This consistency shows that, at least within a similar regime, a single correction map may be able to be used.

Parameter	**Min Value**	**Max Value**
Number Density	< 0.1/cc	0.8/cc
Electron Temperature	200 eV	240,000 eV
Spacecraft Potential	4.0 V	8.0 V

Table 5.2: Plasma parameter ranges for electron data from the flight data selected in Figure 5.9. All data was taken from the tail region during the 2016 tail season.

While it is likely not practical to refine the mesh of the ADP boom sufficiently to resolve the

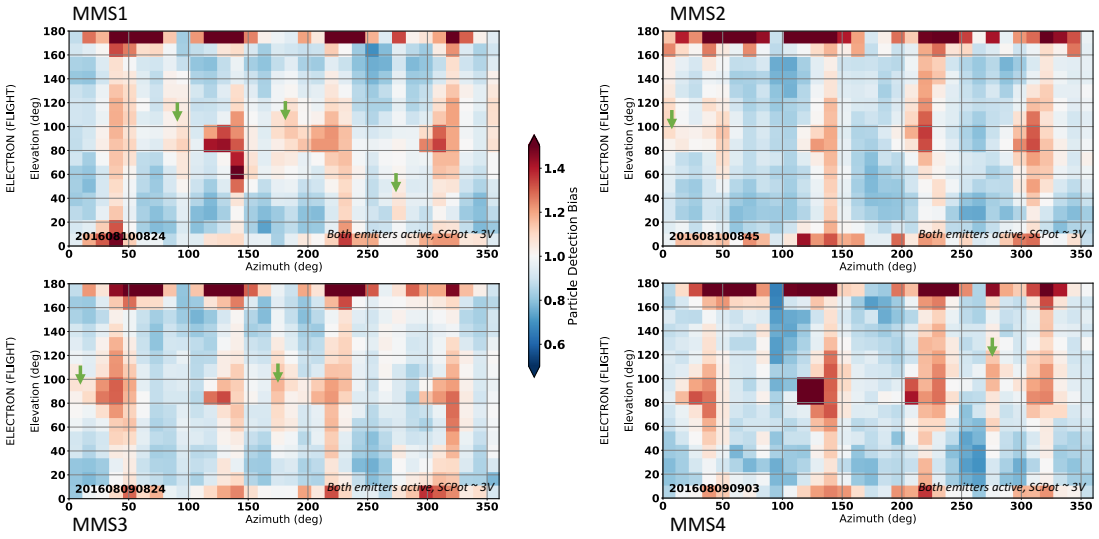

Figure 5.10: Flight electron (DES) bias maps for all four observatories in similar environments. Possible signatures from the ASPOC plume are annotated by green arrows and do not appear in the same locations on all four observatories, despite identical designs and operation.

sheath around each lattice component, it is plausible to include spacecraft spin in the simulation, and to include a contribution from the EDI emitter. The inclusion of spacecraft spin would alleviate the concerns with the stationary photoelectron signature and ASPOC neutralization. Inclusion of EDI may also improve the neutralization of ASPOC and could potentially explain some of the variation between observatories (EDI has a more varied operating scheme[62].)

5.5 Application

This method describes a bias map for particle trajectories as a function of angle and energy due to spacecraft potential effects. In an ideal case, this bias map could be premultiplied by a counts matrix to fully correct the measured counts for electrostatic steering error due to the spacecraft potential and local electric field. While this is possible, two caveats exist:

(1) The bias map is geometric in nature, meaning that it works best for an isotropic plasma, or at least for a plasma without sharp gradients. Narrow beams would be reduced or amplified

in strength as appropriate, however those particles would not necessarily be transferred to the correct location if the correct location had a much lower count rate. For example, 1000 counts could be reduced to 900 by a 0.9 correction factor, but the neighboring pixel may only increase from 10 to 11 with a 1.1 correction factor. In this sense, the integrated density may not be strictly preserved.

(2) The underlying model needs to be better understood and informed. Specifically, the AS-POC plume variation between the model and the flight data and the variation in flight data among the four observatories is cause for conservatism. A compromise, in this case, could be to only correct for the features that are similar and consistent, such as the effects of the booms.

A more reliable use of the bias map is to inform error and uncertainty in a given counts matrix. While a reporting of error in a given pixel (energy/angle combination) would still suffer from the above caveats, the fundamental data is no longer being altered and the map serves, instead, to inform the user of possible error sources or explanations for spacecraft aligned signatures in the data. Similarly, this analysis can serve to inform other corrections or ground processing steps. For example, one might only report velocity moments down to the energy level where the velocity error is less than one angular measurement bin.

5.6 Conclusion

Spacecraft potential changes are accommodated by the ambient plasma forming a sheath around the spacecraft with a varying electric field that eventually decays. This sheath alters the trajectory of incoming particles as they move through the electric field. Modeling this effect has been difficult due to the evolving nature of the sheath around a spacecraft moving through a changing plasma. Presented here is a method whereby the spacecraft potential sheath is modeled with commercial software. A numerical integration scheme was then used to trace particles from a broad distribution through the sheath, resulting in a bias map describing areas of enhances or

depressed counting statistics.

Analysis of the energy and angular distribution of the error was examined and found to be self consistent and plausible. Additionally, results were compared to data from the MMS FPI instrument suite. A qualitative match was evident, although some details of the initial potential map will need to modified for a quantitative correction to be performed. Specifically, the ASPOC plume signature was not consistent between the four observatories or with the simulation. A better neutralization scheme, including spacecraft spin and the EDI emitter may help to improve the simulation accuracy. The flight data appeared similar over the entire measured time range, when looking at similar plasma environments. This lends credibility to the ability to correct raw counts and counteract sheath effects.

The bias maps presented here can be used to inform the reported error in the raw count data. Similarly, the energy/error distributions can highlight the uncertainty

Chapter 6

Concluding Remarks

The Magnetospheric Multiscale (MMS) mission has brought forth a wealth of new knowledge to the scientific community. There have been direct observations of magnetic reconnection in the electron diffusion region[10], the first observations of kinetic Alfvén waves[23], the first detection of magnetic reconnection in the magnetosheath[51], and many other discoveries. Despite the success of the mission, there are always ways to squeeze a little bit more out of the data. As such, this work explores options for improving data quality, increasing data volume, and compiling a set of recommendations for future missions that use similar instrumentation.

This work is broken into three primary fields of investigation, focusing on the Fast Plasma Investigation (FPI):

(1) Data compression is becoming more critical as mission data volumes increase. MMS collects particle data over 100 times faster than previous missions[9, 21], creating a proportionately larger data volume. FPI uses a wavelet compression algorithm, which has never been flown on a space mission before. The FPI compression scheme has performed well, bringing down most data in a lossless manner with no error. If FPI desired, however, and certainly for future missions, there is an option to increase the level of compression. Parameterizing the compression size of existing flight data has shown that the data could be compressed further than what FPI required with little error. Specifically, a series of error modes were explored and it was shown that the compression level can be increased significantly before the signature of the plasma is fundamentally altered. Even if there is a desire to keep

the error below that of Poisson statistical noise, a large increase in compression would be possible. These findings are broken out by specie and by region of the magnetosphere, with some areas compressing better than others. It is therefore recommended that future instrument suites using similar compression, can increase the expected compression ratio, thus bringing down far more data, while understanding what type of error is introduced in their data.

(2) In a second effort to increase scientific applicability of available data products, a study of the FPI trigger data has been performed. The trigger data was intended as a means to rank scientific data for priority download and serve as a quick look, onboard plasma moment summation[52]. A set of scaling factors, was incorporated into the algorithm, however, that allow the dynamic range of the system to be tuned to a specific region. This shifting of dynamic range allows the system to avoid many of the problems with quantization and saturation that have affected previous attempts at onboard moments[45, 21]. Secondarily, once the trigger terms come down to the ground, they are corrected using a trained neural network that takes in all the trigger data and spacecraft potential as an input. Analysis of the neural network showed that it is able to significantly improve the accuracy of these data to a point where they can be released to the scientific community as a set of pseudo moments. This data product will allow the highest time resolution data to be observed for the entire mission instead of only the small fraction of data currently downlinked at the highest data rate. This also serves as a baseline for future missions and shows that it is possible to obtain scientifically useful onboard moment data with a small data volume - a single byte per data point in this case, a factor of 256 reduction in data volume over the raw data.

(3) Finally, to increase the quality of the burst data brought down, an analysis of the effects from the spacecraft potential sheath have been performed. A SPIS model of the spacecraft electric field environment and charge state[13] has been used as a domain to fly four million

test particles through in all directions and energies. The resulting statistical analysis shows that there is an inherent bias in FPI look angle due to interference from other aspects of the spacecraft. Of particular note, the SDP wire booms alter particle trajectories even above 1000 eV. These results was found to be consistent with observations of flight data ranging over the course of a month of data, however the signature resulting from the ASPOC indium ion plume was found to vary significantly between the four observatories. The fidelity of the comparison was sufficiently high as to discover some missing elements in the simulation (notably the electron plume from the Electron Drift Instrument (EDI), and spacecraft spin.) This results of this analysis show that this type of bias map could be used to report areas of uncertainty or error in measurements and, in some cases, to provide corrections to the raw counts.

Future efforts on these items primarily will involve increasing the fidelity of the work. For the data compression analysis, new types of data (field data, for example) may be analyzed for use with wavelet compression. For the trigger system, a more advanced metric for estimating error may be undertaken, as well as attempting to recover the lost sign of the velocities. For the sheath modeling, a more robust potential model will be created, allowing the bias map to be incorporated into the FPI ground corrections.

In summary, this body of research has outlined methods to increase both data volume and quality for the FPI suite. These lessons learned will serve to inform future missions that perform plasma measurements as well.

Bibliography

[1] Osama K Al-Shaykh and Russell M Mersereau. Lossy compression of noisy images. IEEE Transactions on Image Processing, 7(12):1641–1652, 1998.

[2] Amptek a121 charge sensitive preamplifier - discriminator data specification sheet. `http://www.amptek.com/pdf/a121.pdf`. Accessed: 2018-07-31.

[3] Clémentine Barreyre, Béatrice Laurent, Jean-Michel Loubes, Bertrand Cabon, and Loïc Boussouf. Statistical methods for outlier detection in space telemetries. In 2018 SpaceOps Conference, page 2533, 2018.

[4] AC Barrie, D da Silva, S Elkington, Z Sternovsky, AC Rager, DJ Gershman, WR Paterson, JC Dorelli, and B Giles. Physically accurate large dynamic range pseudo-moments for the mms fast plasma investigation. Earth and Space Science, 2018.

[5] AC Barrie, S Elkington, Z Sternovsky, D Smith, B Giles, and C Schiff. Wavelet compression performance of mms/fpi plasma count data. Journal of Geophysical Research: Earth and Space Science, 2018. Under Review.

[6] AC Barrie, SE Smith, JC Dorelli, DJ Gershman, P Yeh, C Schiff, and LA Avanov. Performance of a space-based wavelet compressor for plasma count data on the mms fast plasma investigation. Journal of Geophysical Research: Space Physics, 122(1):765–779, 2017.

[7] AC Barrie, Z Sternovsky, and S Elkington. Correcting particle measurements for potential sheath effects. In Preparation.

[8] AL Borg, M Øieroset, TD Phan, FS Mozer, A Pedersen, C Mouikis, JP McFadden, C Twitty, A Balogh, and H Rème. Cluster encounter of a magnetic reconnection diffusion region in the near-earth magnetotail on september 19, 2003. Geophysical research letters, 32(19), 2005.

[9] J Burch, T Moore, R Torbert, and B Giles. Magnetospheric multiscale overview and science objectives. Space Science Reviews, 199, 2016.

[10] JL Burch, RB Torbert, TD Phan, L-J Chen, TE Moore, RE Ergun, JP Eastwood, DJ Gershman, PA Cassak, MR Argall, et al. Electron-scale measurements of magnetic reconnection in space. Science, 352(6290):aaf2939, 2016.

[11] CW Carlson, DW Curtis, G Paschmann, and W Michel. An instrument for rapidly measuring plasma distribution functions with high resolution. Advances in Space Research, 2(7):67–70, 1982.

[12] C Cattell, J Dombeck, J Wygant, JF Drake, M Swisdak, ML Goldstein, W Keith, A Fazakerley, M André, E Lucek, et al. Cluster observations of electron holes in association with magnetotail reconnection and comparison to simulations. Journal of Geophysical Research: Space Physics, 110(A1), 2005.

[13] F. Cipriani, P. Escoubet, K Torkar, R. Nakamura, G. Dprez, D. Rodgers, Y Khotyaintsev, and A Barrie. Simulated effects of aspocs on plasma measurements performed onboard the magnetospheric multiscale mission. Proceedings of the 15th Spacecraft Charging Technology Conference, 2018.

[14] Glyn A Collinson, John C Dorelli, Levon A Avanov, Gethyn R Lewis, Thomas E Moore, Craig Pollock, Dhiren O Kataria, Robert Bedington, Chris S Arridge, Dennis J Chornay, et al. The geometric factor of electrostatic plasma analyzers: A case study from the fast plasma investigation for the magnetospheric multiscale mission. Review of Scientific Instruments, 83(3):033303, 2012.

[15] Lossless Data Compression. Recommendation for space data system standards. Technical report, CCSDS 121.0-B-1. Blue Book, 2005.

[16] CM Cully, RE Ergun, and AI Eriksson. Electrostatic structure around spacecraft in tenuous plasmas. Journal of Geophysical Research: Space Physics, 112(A9), 2007.

[17] Xavier Delaunay, Marie Chabert, Vincent Charvillat, and Géraldine Morin. Satellite image compression by post-transforms in the wavelet domain. Signal Processing, 90(2):599–610, 2010.

[18] RE Ergun, S Tucker, J Westfall, KA Goodrich, DM Malaspina, D Summers, J Wallace, M Karlsson, J Mack, N Brennan, et al. The axial double probe and fields signal processing for the mms mission. Space Science Reviews, 199(1-4):167–188, 2016.

[19] S Fuselier, W Lewis, C Schiff, R Ergun, J Burch, S Petrinec, and K Trattner. Magnetospheric multiscale science mission profile and operations. Space Science Reviews, 199, 2016.

[20] Henry Berry Garrett. The charging of spacecraft surfaces. Reviews of Geophysics, 19(4):577–616, 1981.

[21] J Geach, SJ Schwartz, Vincent Génot, O Moullard, A Lahiff, and AN Fazakerley. A corrector for spacecraft calculated electron moments. In Annales Geophysicae, volume 23, pages 931–943, 2005.

[22] Vincent Génot and S. J. Schwartz. Spacecraft potential effects on electron moments derived from a perfect plasma detector. Annales Geophysicae, 22(6):2073–2080, June 2004.

[23] Daniel J Gershman, F Adolfo, John C Dorelli Viñas, Scott A Boardsen, Levon A Avanov, Paul M Bellan, Steven J Schwartz, Benoit Lavraud, Victoria N Coffey, Michael O Chandler, et al. Wave-particle energy exchange directly observed in a kinetic alfvén-branch wave. Nature Communications, 8, 2017.

[24] Daniel J Gershman, Levon A Avanov, Scott A Boardsen, John C Dorelli, Ulrik Gliese, Alexander C Barrie, Conrad Schiff, William R Paterson, Roy B Torbert, Barbara L Giles, et al. Spacecraft and instrument photoelectrons measured by the dual electron spectrometers on mms. Journal of Geophysical Research: Space Physics, 122(11), 2017.

[25] Daniel J Gershman, John C Dorelli, Adolfo F-Viñas, and Craig J Pollock. The calculation of moment uncertainties from velocity distribution functions with random errors. Journal of Geophysical Research: Space Physics, 120(8):6633–6645, 2015.

[26] Rafael C Gonzalez, Richard E Woods, Steven L Eddins, et al. Digital image processing using MATLAB., volume 624. Pearson-Prentice-Hall Upper Saddle River, New Jersey, 2004.

[27] Lidwine Gross, Sylvie Thiria, and Robert Frouin. Applying artificial neural network methodology to ocean color remote sensing. Ecological Modelling, 120(2):237–246, 1999.

[28] Stanislas Guillemant, Vincent Génot, Jean-Charles Mateo Velez, Pierre Sarrailh, Alain Hilgers, and Philippe Louarn. Simulation study of spacecraft electrostatic sheath changes with the heliocentric distances from 0.044 to 1 au. IEEE Transactions on Plasma Science, 41(12):3338–3348, 2013.

[29] Daniel Hastings and Henry Garrett. Spacecraft-environment interactions. Cambridge university press, 2004.

[30] S Hussain and R Marchand. Sheath-induced distortions in particle distributions near enhanced polar outflow probe particle sensors. Physics of Plasmas, 21(7):072902, 2014.

[31] Diederik Kingma and Jimmy Ba. Adam: A method for stochastic optimization. arXiv preprint arXiv:1412.6980, 2014.

[32] Nicholas A Krall, Alvin W Trivelpiece, and Robert A Gross. Principles of plasma physics. American Journal of Physics, 41(12):1380–1381, 1973.

[33] Kristopher Larsen, Chris Pankratz, Barbara Giles, Kim Kokkonen, Brian Putnam, Corey Schafer, Dan Baker, and Jim Burch. The mms science data center. operations, capabilities, and data availability. In EGU General Assembly Conference Abstracts, volume 18, page 10061, 2016.

[34] Robert P Lin. Particle acceleration in solar flares. In AIP Conference Proceedings, volume 1516, pages 121–122. AIP, 2013.

[35] RP Lin, KA Anderson, S Ashford, C Carlson, D Curtis, R Ergun, D Larson, J McFadden, M McCarthy, GK Parks, et al. A three-dimensional plasma and energetic particle investigation for the wind spacecraft. Space Science Reviews, 71(1):125–153, 1995.

[36] P-A Lindqvist, Göran Olsson, RB Torbert, B King, M Granoff, D Rau, G Needell, S Turco, I Dors, P Beckman, et al. The spin-plane double probe electric field instrument for mms. Space Science Reviews, 199(1-4):137–165, 2016.

[37] D Mackler, L Avanov, A Barrie, D Chornay, D Gershman, B Giles, C Pollock, A Rager, and S Smith. Microchannel plate lifetime experiment for the dis and des instruments on the magnetospheric multiscale mission. Planetary and Space Science, 2018.

[38] Myron J Mandell, Victoria A Davis, David L Cooke, Adrian T Wheelock, and Christopher J Roth. Nascap-2k spacecraft charging code overview. Technical report, SCIENCE APPLICATIONS INC SAN DIEGO CA, 2005.

[39] Jose Martinez. New telemetry monitoring paradigm with novelty detection. In SpaceOps 2012, page 1275123. 2012.

[40] JP McFadden, CW Carlson, D Larson, J Bonnell, F Mozer, V Angelopoulos, K-H Glassmeier, and U Auster. Themis esa first science results and performance issues. In The THEMIS Mission, pages 477–508. Springer, 2009.

[41] Mms mission, nasa profile. `https://mms.gsfc.nasa.gov/science.html`. Accessed: 2018-07-31.

[42] National aeronautics and space administration. `http://www.nasa.gov`. Accessed: 2018-07-31.

[43] Travis E Oliphant. Scipy: Open source scientific tools for python. Computing in Science and Engineering, 9:10–20, 2007.

[44] LW Parker and EC Whipple. Theory of spacecraft sheath structure, potential, and velocity effects on ion measurements by traps and mass spectrometers. Journal of Geophysical Research, 75(25):4720–4733, 1970.

[45] G Paschmann, H Loidl, P Obermayer, M Ertl, R Laborenz, N Sckipke, W Baumjohann, CW Carlson, and DW Curtis. The plasma instrument for ampte irm. IEEE transactions on geoscience and remote sensing, (3):262–266, 1985.

[46] Götz Paschmann and Patrick W Daly. Analysis methods for multi-spacecraft data. ESA publications division, 1998.

[47] WR Paterson, AC Barrie, SA Boardsen, BL Giles, R Ergun, LA Avanov, MO Chandler, VN Coffey, J Dorelli, DJ Gershman, et al. Prioritization for downlink of scientific observations for the magnetospheric multiscale mission using trigger parameters from the fast plasma instrumentation. In AGU Fall Meeting Abstracts, 2016.

[48] F. Pedregosa, G. Varoquaux, A. Gramfort, V. Michel, B. Thirion, O. Grisel, M. Blondel, P. Prettenhofer, R. Weiss, V. Dubourg, J. Vanderplas, A. Passos, D. Cournapeau, M. Brucher, M. Perrot, and E. Duchesnay. Scikit-learn: Machine learning in Python. Journal of Machine Learning Research, 12:2825–2830, 2011.

[49] LR Petzold and AC Hindmarsh. Lsoda; computing and mathematics research division. Lawrence Livermore National Laboratory, Livermore, CA, 1997.

[50] T Phan, HU Frey, S Frey, L Peticolas, S Fuselier, C Carlson, H Reme, J-M Bosqued, A Balogh, M Dunlop, et al. Simultaneous cluster and image observations of cusp reconnection and auroral proton spot for northward imf. Geophysical research letters, 30(10), 2003.

[51] TD Phan, JP Eastwood, MA Shay, JF Drake, BU Ö Sonnerup, M Fujimoto, PA Cassak, M Øieroset, JL Burch, RB Torbert, et al. Electron magnetic reconnection without ion coupling in earth's turbulent magnetosheath. Nature, 557(7704):202, 2018.

[52] C Pollock, T Moore, A Jacques, J Burch, U Gliese, Y Saito, T Omoto, L Avanov, A Barrie, V Coffey, et al. Fast plasma investigation for magnetospheric multiscale. Space Science Reviews, 199, 2016.

[53] Eric Priest and Terry Forbes. Magnetic reconnection. Magnetic Reconnection, by Eric Priest, Terry Forbes, Cambridge, UK: Cambridge University Press, 2007, 2007.

[54] A. C. Rager, J. C. Dorelli, D. J. Gershman, V. Uritsky, L. A. Avanov, R. B. Torbert, J. L. Burch, R. E. Ergun, J. Egedal, C. Schiff, J. R. Shuster, B. L. Giles, W. R. Paterson, C. J. Pollock, R. J. Strangeway, C. T. Russell, B. Lavraud, V. N Coffey, and Y. Saito. Electron crescent distributions as a manifestation of diamagnetic drift in an electron scale current sheet: Magnetospheric multiscale observations using new 7.5 ms fast plasma investigation moments. Geophysical Research Letters, 2017. 2017GL076260.

[55] Frank Rosenblatt. Principles of neurodynamics. perceptrons and the theory of brain mechanisms. Technical report, CORNELL AERONAUTICAL LAB INC BUFFALO NY, 1961.

[56] Jean-FranÇois Roussel, FranÇois Rogier, Guillaume Dufour, Jean-Charles Mateo-Velez, Julien Forest, Alain Hilgers, David Rodgers, Laurence Girard, and Denis Payan. Spis open-source code: Methods, capabilities, achievements, and prospects. IEEE Transactions on Plasma Science, 36(5):2360–2368, 2008.

[57] Earl E Scime, John L Phillips, and Samuel J Bame. Effects of spacecraft potential on three-dimensional electron measurements in the solar wind. Journal of Geophysical Research: Space Physics, 99(A8):14769–14776, 1994.

[58] JBj Taylor. Relaxation and magnetic reconnection in plasmas. Reviews of Modern Physics, 58(3):741, 1986.

[59] B Thiébault, A Hilgers, E Sasot, H Laakso, P Escoubet, Vincent Génot, and J Forest. Potential barrier in the electrostatic sheath around a magnetospheric spacecraft. Journal of Geophysical Research: Space Physics, 109(A12), 2004.

[60] Carole Thiebaut, Emmanuel Christophe, Dimitri Lebedeff, and Christophe Latry. Cnes studies of on-board compression for multispectral and hyperspectral images. In Satellite Data Compression, Communications, and Archiving III, volume 6683, page 668305. International Society for Optics and Photonics, 2007.

[61] RB Torbert, CT Russell, W Magnes, RE Ergun, P-A Lindqvist, Olivier LeContel, H Vaith, J Macri, S Myers, D Rau, et al. The fields instrument suite on mms: Scientific objectives, measurements, and data products. Space Science Reviews, 199(1-4):105–135, 2016.

[62] RB Torbert, H Vaith, M Granoff, M Widholm, JA Gaidos, BH Briggs, IG Dors, MW Chutter, J Macri, M Argall, et al. The electron drift instrument for mms. Space Science Reviews, 199(1-4):283–305, 2016.

[63] K Torkar, R Nakamura, M Tajmar, C Scharlemann, H Jeszenszky, G Laky, G Fremuth, CP Escoubet, and K Svenes. Active spacecraft potential control investigation. Space Science Reviews, 199(1-4):515–544, 2016.

[64] K Torkar, W Riedler, M Fehringer, CP Escoubet, K Svenes, BT Narheim, A Fazakerley, S Szita, and M André. Effects of active spacecraft potential control on cluster plasma measurements-first results. In Spacecraft Charging Technology, volume 476, page 255, 2001.

[65] Paul Winterrowd, Chad Orbe, Jack Venbrux, Sterling Whitaker, Eric Cameron, Ronald Nelson, Gary Maki, Dave Fisher, and Pen-Shu Yeh. A 320 mbps flexible image data compressor for space applications. In Aerospace Conference, 2010 IEEE, pages 1–6. IEEE, 2010.

[66] Guoxia Yu, Tanya Vladimirova, and Martin N Sweeting. Image compression systems on board satellites. Acta Astronautica, 64(9-10):988–1005, 2009.

Appendix A

FPI Energy Targets

The current energy targets, as of July 1, 2018 are presented here. Each of four EEPROM slots houses a single 32 step table. These tables represent the center of the energy bin; the bandpass of DES is $\sim 18\%$ and DIS is $\sim 13\%$. Each time the spacecraft enters a science region of interest, a new table is loaded. The applied voltage to the electrostatic analyzer (ESA) and deflecting electrodes are calculated based on these energy targets and the look direction.

Note that in EEPROM3 there is a *DIS Safety* table. This table is for use on a short term basis when there is a suspected high voltage discharge in a DIS unit. This is a known failure mode in DIS due to a workmanship issue during manufacturing. The safety table reduces the max voltage in all DIS units and is intended to be used only long enough for a permanent fix to be uploaded, which reduces the voltage on the specific unit in question. In addition to this safety table, a secondary mitigation against discharges is to use a lower maximum voltage in the electromagnetic (EM) sheath table. Because DES does not share this concern, it does not reduce the voltage in the safety or EM sheath tables.

Both DES and DIS use a reduced energy range when observing solar wind. This is not a safety concern, but is rather to increase resolution around the expected solar wind energy range.

DIS	EEPROM1	EEPROM2	EEPROM3	EEPROM4
Energy Bin	Tail Targets (eV)	EM Sheath Targets (eV)	DIS Safety Targets (eV)	Solar Wind Targets (eV)
0	2.16	2.16	2.16	210.00
1	3.91	3.91	3.91	236.80
2	7.07	7.07	7.07	267.03
3	10.93	10.93	10.93	301.11
4	14.47	14.24	13.97	339.55
5	19.16	18.54	17.85	382.89
6	25.37	24.14	22.81	431.76
7	33.59	31.44	29.16	486.87
8	44.48	40.94	37.26	549.02
9	58.89	53.32	47.61	619.10
10	77.98	69.44	60.85	698.12
11	103.24	90.43	77.76	787.23
12	136.7	117.77	99.37	887.71
13	180.99	153.36	126.99	1001.02
14	239.63	199.72	162.29	1128.79
15	317.28	260.1	207.4	1272.87
16	420.09	338.72	265.04	1435.34
17	556.22	441.11	338.71	1618.55
18	736.45	574.45	432.85	1825.14
19	975.08	748.1	553.16	2058.11
20	1291.03	974.23	706.9	2320.80
21	1709.37	1268.72	903.38	2617.04
22	2263.26	1652.24	1154.47	2951.08
23	2996.62	2151.68	1475.35	3327.76
24	3967.62	2802.1	1885.41	3752.52
25	5253.25	3649.12	2409.44	4231.49
26	6955.46	4752.19	3079.12	4771.60
27	9209.24	6188.69	3934.94	5380.66
28	12193.31	8059.43	5028.62	6067.45
29	16144.31	10495.65	6426.29	6841.91
30	21375.56	13668.31	8212.42	7715.22
31	28301.89	17800	10495	8700.00

Table A.1: Energy targets for the DIS spectrometers in each of the four EEPROM slots, as of July 1, 2018. The DIS Safety table is intended to reduce the max voltage on the DIS units in case of high voltage discharge concerns due to a known manufacturing concern in DIS.

DES	EEPROM1	EEPROM2	EEPROM3	EEPROM4
Energy Bin	Tail Targets (eV)	EM Sheath Targets (eV)	DIS Safety Targets (eV)	Solar Wind Targets (eV)
0	6.52	6.52	6.52	4.38
1	8.54	8.54	8.54	5.19
2	11.17	11.17	11.17	6.15
3	14.63	14.63	14.63	7.30
4	19.15	19.15	19.15	8.66
5	25.07	25.07	25.07	10.27
6	32.81	32.81	32.81	12.18
7	42.95	42.95	42.95	14.45
8	56.23	56.23	56.23	17.14
9	73.60	73.60	73.60	20.32
10	96.34	96.34	96.34	24.11
11	126.12	126.12	126.12	28.59
12	165.09	165.09	165.09	33.91
13	216.11	216.11	216.11	40.22
14	282.89	282.89	282.89	47.71
15	370.31	370.31	370.31	56.58
16	484.74	484.74	484.74	67.11
17	634.54	634.54	634.54	79.60
18	830.63	830.63	830.63	94.41
19	1087.31	1087.31	1087.31	111.98
20	1423.32	1423.32	1423.32	132.82
21	1863.16	1863.16	1863.16	157.54
22	2438.92	2438.92	2438.92	186.85
23	3192.61	3192.61	3192.61	221.62
24	4179.20	4179.20	4179.20	262.86
25	5470.68	5470.68	5470.68	311.77
26	7161.25	7161.25	7161.25	369.78
27	9374.25	9374.25	9374.25	438.59
28	12271.12	12271.12	12271.12	520.21
29	16063.20	16063.20	16063.20	617.01
30	21027.11	21027.11	21027.11	731.82
31	27525.00	27525.00	27525.00	868.00

Table A.2: Energy targets for the DES spectrometers in each of the four EEPROM slots, as of July 1, 2018. The DIS Safety table is intended to reduce the max voltage on the DIS units in case of high voltage discharge concerns due to a known manufacturing concern in DES. The DES voltage is not changed in the DIS Safety table.